Mechanisms of Condensed Phase Reactions: The Role of Structure, Dynamics, and Environment in Photoisomerization and Photodissociation

Christopher James Otolski

Submitted to the graduate degree program in Department of Chemistry and the Graduate Faculty of the University of Kansas in partial fulfillment of the requirements for the degree of Doctor of Philosophy.

Committee members

Christopher G. Elles, Chairperson

Carey K. Johnson

Ward H. Thompson

James D. Blakemore

Hui Zhao

Date defended: May 29, 2019

The Thesis Committee for Christopher James Otolski certifies
that this is the approved version of the following thesis :

Mechanisms of Condensed Phase Reactions:
The Role of Structure, Dynamics, and Environment in Photoisomerization and Photodissociation

Christopher G. Elles, Chairperson

Date approved: June 9, 2019

Abstract

Light-activated chemistry begins with the excitation of a ground-state molecule to a higher-lying excited state. Once in the excited state, the nuclei in the molecule respond by trying to minimize the energy of the system. The nuclear motions sometimes propagate along a pathway that facilitates a reaction, such as isomerization or dissociation. However, in the condensed phase, the environment impacts these fundamental dynamics, thereby changing the excitation process and altering the nuclear motions of the molecule. In order to investigate the kinetics and dynamics for a variety of light sensitive systems we use time-resolved pump-probe spectroscopy. Transient optical and x-ray absorption spectroscopy provide valuable insight into the different reactive pathways and fundamental chemistry in light-activated systems.

First, we show how spatial confinement for a series of stilbene and azobenzene deivatives profoundly impacts the isomerization dynamics involving large amplitude structural rearrangements of a molecule. This work uses ultrafast spectroscopy to probe the effects of confinement for molecules encapsulated in a supramolecular host-guest complex. The supramolecular complex distorts the ground- and excited-state potential energy surfaces, including the conical intersection connecting those states, which results in hindered nuclear motions and different reactive pathways. For stilbene derivatives, the transient absorption measurements reveal broader excited-state absorption spectra, longer excited-state lifetimes, and reduced quantum yields for isomerization in the restricted environment. The organic capsule disrupts the equilibrium structure and restricts torsional rotation around the central C=C double bond in the excited-state, which is an important motion for the relaxation of *trans*-stilbene from S_1 to S_0. Unlike stilbene, azobenzene derivatives also have an in-plane inversion pathway for isomerization, in additon to out-of-plane rotation around the N=N bond. The transient absorption spectroscopy of the encapsulated azobenzene derivative reveals formation of the *cis* isomer in the excited state after exciting the *trans* geometry,

indicating a direct excited-state isomerization channel that is not observed in solution. The confined environment provides new mechanistic insight on the relative roles of inversion and rotation in the ultrafast photoisomerization of azobenzene derivatives.

The solvent affects the photodissociation reactions of manganese tricarbonyl complexes. Interest in manganese tricarbonyl complexes stems from the possible use as earth abundant catalysts for CO_2 reduction, but the complexes decompose under visible light. To investigate the photodecomposition of manganese tricarbonyl complexes, we use ultrafast transient absorption spectroscopy and time-resolved x-ray absorption spectroscopy. The optical transient absorption measurement probes the femtosecond relaxation of a metal-to-ligand charge transfer state via back-electron-transfer, which facilitates the loss of a CO ligand to form a 5-coordinate Mn species. The 5-coordinate species has two competing reaction pathways, the first is solvent coordination to form a stable 6-coordinate Mn species and the second pathway involves the 5-coordinate species reducing the starting Mn^I complex to a Mn^0 species. In order to distinguish between the two pathways, we use a non-coordinating solvent which prevents the formation of the 6-coordinate complex and results in the survival of a 5-coordinate species in solution. Time-resolved x-ray absorption measurements provide structural information about the 5-coordinate and solvent-coordinated manganese species on the picosecond to nanosecond timescale. The combination of optical and x-ray techniques provides new insight into the photodecomposition pathway for manganese tricarbonyl complexes.

Finally, we examine the excitation event directly for photochromic molecules in the plasmonic field of an array of gold nanorods. Incident laser light on a gold nanostructure creates an enhanced electric field capable of driving higher-order excitation processes. To investigate the spatial dependence and anisotropy of optical activation in the field surrounding gold nanorods, we use pulsed 800 nm laser light incident on a plasmonic array of gold nanorods to induce an oscillating plasmonic field that interacts with an overlaid film of photochromic molecules through nonlinear two-photon excitation. Following nonlinear excitation, the photochromic molecules isomerize. The enhanced electric field results in a larger fraction of molecules excited in the near-field in compari-

son with the photochromic molecules outside of the enhanced field. The conversion rate is greatest at the tips of the nanorod where the enhanced electric field is the strongest. However, the observed conversion rate depends on the difference in polarization vectors for the 800 nm and probe light near the nanoparticle surface. The excitation and probe fields have different alignment based on the wavelength-dependence of the plasmonic resonance. Using a simple simulation of the enhanced near-field, we model the conversion of molecules around a single gold nanorod.

Acknowledgements

I want to begin by thanking my advisor Dr. Christopher Elles, for his confidence in me as a scientist and for allowing me into his research group. Over the last 5 years Chris has taught me and guided my research with unwavering enthusiasm, patience and perseverance. On my journey through graduate school I could not have asked for a better mentor who always had my best interests in mind and helped to develop me into the best scientist I could be. I owe much of my success to him and will forever be thankful for the opportunities he provided as well as the time and energy he invested in helping me reach my goals both here at KU and in my future career.

Next, I want to thank my parents Kevin and Carolyn for supporting me during my time in graduate school. They were always there for me and I enjoyed being reminded to take a break from my studies to come home. I am very grateful to have such loving parents.

I would also like to thank those formerly and currently in the Elles research group, Dr. Amanda Houk, Dr. Tim Quincy, Matt Barclay, David Stierwalt, Kristen Burns, Dan Johnson and PJ Srivastava for their many scientific discussions, which helped to produce this dissertation. Throughout my graduate career they all made time in their busy schedules to help me with my science and I really appreciate it. I have also enjoyed our time celebrating each others achievements and growing as a group.

Lastly I want to thank all the great friends I have made during my time here at KU, especially Tal, Nate, Bryce, Melissa and Josh. They made this journey more enjoyable, but more importantly they provided encouragement, advice and support when I needed it, and therefore they are rooted in my success. I feel very fortunate to have such great friends in my life.

Contents

List of Figures

List of Tables

Chapter 1

Introduction

A powerful tool for studying chemical systems is absorption spectroscopy, which includes numerous techniques ranging from low-energy rotational spectroscopy up to high-energy x-ray absorption spectroscopy. This fundamental interaction between light and matter provides detailed information about a chemical system, and that information can be different across techniques. For example, x-ray absorption spectroscopy provides structural information about the molecule while optical absorption spectroscopy examines the electronic transitions in a molecule.[1,2] However, many chemical systems are not static, they are dynamical and evolving over time. Therefore, we carry out a spectroscopy measurement with pulsed light sources to produce time-resolved kinetic information pertaining to chemical reactions. One stipulation however is that the duration of the pulse needs to be on the same timescale as the process to be measured. For example, the μs dynamics for protein unfolding could easily be resolved with a nanosecond pulse duration.[3] A pulse duration on the femtosecond (fs) timescale ($1\text{x}10^{-15}$ s) opens up the possibility of measuring the movement of individual atoms within a molecule.[1]

Ultrafast spectroscopy monitors the nuclear motion of a molecule after an optical perturbation. The absorption of a photon brings the molecule from the electronic ground state to the Franck-Condon region of the excited-state, then the molecule evolves along the excited-state surface.[4] In the gas phase, the motions of the excited molecule are governed solely by the electronic structure of the molecule due to the limited environmental interactions, however this is not the case for reactions in the condensed phase. The environment surrounding a photo-activated molecule plays an important role in the excited-state reaction kinetics and dynamics by restricting or enhancing different reaction pathways, which can influence the reaction rates, yields and even the products

formed.

In this dissertation we use ultrafast transient electronic absorption spectroscopy and time-resolved x-ray absorption spectroscopy to examine the kinetics and dynamics of photo-activated molecules in the condensed phase in order to gain insight into the fundamental chemistry that governs the reactive pathways.[5,6] However, environmental interactions such as steric restrictions or solvent coordination can play a role in manipulating the reactive pathways, which can impact the chemistry on the short and long timescales. Elucidating the effects of the environment on the excited-state dynamics will provide more detail into photo-activated mechanisms. Although the collection of chapters in this dissertation measure a broad range of fundamentally important aspects of chemistry ranging from reaction dynamics in confined environments (chapters 3-5), to reactions of metal coordination compounds (chapter 6), to nonlinear excitation of photochromic molecules in a plasmonic field of a nanoparticle (chapter 7), the experiments are motivated by the environment and its influence on the fundamental chemistry.

1.1 Chemistry in Confined Environments

In an attempt to simplify a chemical system, experiments are sometimes conducted in the gas phase to isolate a reactive species. However, outside of the very well controlled gas phase environment exists a much more complex environment where chemical systems cannot be considered to occur in isolation. Instead, many reactive processes of interest such as those found in biology take place in condensed phase. This difference in environment opens up the possibility for interactions between a solute and the surrounding solvent molecules.

Early measurements into solvent influence on reaction dynamics examined the photoisomerization reaction of *trans*-stilbene in the condensed phase.[7] These studies showed a barrier for relaxation in *trans*-stilbene, which also had a solvent dependence based on viscosity. To explain the isomerization reaction in the condensed phase, models such as Kramer's friction model were used, which provided insight into how the solvent viscosity affected the reaction barriers and rates.[8] Studies such as this led the way for others to investigate the reaction rates, yields and even the prod-

ucts formed by the influence of solvation.[9–13] However, many biological light-driven isomerization reactions, such as vision and phototaxy, are not in a pure solvent environment and as a result exhibit different excited-state dynamics. Nature makes use of spatially confined active sites on proteins to provide steric constraints which guide the early stages in light-activated process.[14–21] These confined environments also provide a much more direct influence on the light-activated chemistry by restricting the motions of the molecule. The confined environment opens up the possibility to explore and drive photochemistry in ways that a solvent environment cannot.[22–24]

Cyclodextrins (CDs) are a popular supramolecular framework, which are oligosaccarides of 6, 7, or 8 d-glucopyranose units and are capable of encapsulating a guest molecule.[25,26] In one study the authors investigated the photoisomerization dynamics of encapsulated stilbene using different sized CDs.[27] The fluorescence data showed that when the stilbene is held tightly inside the CD a slow single-exponential decay is measured. The single decay suggests a uniform stilbene/CD complex throughout the solution. Alternatively, a bi-exponential fluorescence decay is observed for the larger cavities, which indicates two different complexes are present and yield vastly different reaction dynamics. It is suggested that the stilbene molecule in the larger cavity is more loose, which allows it to slip in and out of the cavity to produce the bi-exponential decay observed in the measurement. The results from this study provide information and a model to begin understanding reactions in restricted environments.

The appeal of using confined environments to manipulate the dynamics of photochemical reactions has led to other synthetic cavities such as nanoporous materials, and self-assembled structures ranging from reverse micelles to the cavities of extended molecular frameworks.[28–34] In a similar way as proteins drive isomerization in a chromophore, the synthetic cavities present an opportunity to selectively manipulate the dynamics of photochemical reactions by influencing the structural rearrangement of a molecule.[23,35–37] Reactions in confined environments not only open the possibility of new applications, but also provide a window on the underlying details that control the reaction dynamics.[38]

To better understand the photoisomerization dynamics in a confined environment we encapsu-

late a stilbene molecule in a host-guest complex and then use ultrafast pump-probe spectroscopy to monitor the excited-state dynamics. The host-guest complex consists of a water-soluble supramolecular 'octa acid' cavitand, which spontaneously forms a dimer capsule by incarcerating a hydrophobic guest molecule.[39,40] Given the size and shape of the interior of the octa acid capsule, only a single stilbene molecule fits inside while maintaining the ability to photoisomerize.[40–43] The stilbene molecule is selected for encapsulation due its straightforward isomerization reaction, which has been studied extensively.[7,8,44–55] The well-known *trans*→*cis* isomerization mechanism requires rotation of the phenyl rings around the central C=C bond axis after excitation to the $S_1(\pi\pi^*)$ state.[45,46] Trapping stilbene in synthetic host-guest complexes promises to offer new insight on the role of external forces, such as steric interactions, in selectively controlling reaction dynamics, fluorescence yields, and other properties of a chromophore.[56–58] For example, a tight-fitting cavitand was recently shown to suppress the fluorescence of encapsulated stilbene by rotating the molecule sufficiently far along the C=C rotation axis in the ground state that optical excitation avoids the torsional barrier in the excited state.[56] Crowding is also investigated using alkyl-substituents on the incarcerated stilbene molecule, which change the relative size and shape of the molecule and affects the relative stabilities of the *trans* and *cis* isomers, as well as the ability to photoisomerize around the central ethylene bridge.

Azobenzene is another prototypical photochromic compound with a similar structure and size to stilbene, and undergoes isomerization after photoexcitation. However, the photoisomerization dynamics of azobenzene remain controversial due to the nitrogen atoms being able to rehybridize, which opens up additional relaxation pathways for the molecule. After $\pi\pi^*$ excitation of azobenzene, the relaxation mechanism was initially thought to isomerize solely by out-of-plane rotation around the N=N double bond, whereas after $n\pi^*$ excitation isomerization occurred entirely through in-plane inversion of the phenyl ring along the Ph-N=N coordinate by rehybridization of the nonbonding electrons.[59–65] This simple view proved to be inadequate for describing the photoisomerization dynamics of azobenzene after $\pi\pi^*$ and $n\pi^*$ excitation. By restricting the isomerization dynamics for azobenzene using the octa acid capsule new insight into the photoiosomerization dy-

namics and how interactions with the confined environment can drive different reaction pathways is provided. For example, the confined azobenzene molecule has unique reaction pathways involving relaxation to the *cis* isomer in the excited state after exciting the *trans* isomer, which is a reaction pathway not evident for azobenzene solution measurements. The information gathered from investigating the photoisomerization reaction provides insight into how the confined environment influences the excited-state dynamics.

1.2 Photodecomposition of Mn Tricarbonyl Complex

The conversion of CO_2 into useful products such as fuels is one approach for suppling society's ever increasing energy demand and is accomplished through the use of catalysis.[66] Catalysts for CO_2 reduction need to be robust while also being selective to the chemical systems in order avoid unwanted chemistry. The rhenium tricarbonyl and manganese tricarbonyl complexes are two molecular catalyst frameworks that have acquired attention due to their simplicity of preparation, selectivity for CO production, and high turnonver rate.[67–69] Additionally, the ease of modifying the metal tricarbonyl frameworks led to a plethora of supporting ligands to tune the catalytic properties.[70] The manganese tricarbonyl framework offers a cheap and more environmentally friendly complex for building catalysts compared with the more expensive and toxic rhenium metal. However, the manganese tricarbonyl catalysts are less stable under exposure to visible light. Photoreactivity studies found that irradiation with a visible light source results in the decomposition of the Mn tricarbonyl framework.[71–74] Elucidating the decomposition mechanism of the Mn tricarbonyl complex will provide insight into the mechanism for decomposition as well as the bimolecular chemistry occurring on longer timescales, which has yet to be entirely understood.

Early work examining the photodecomposition reaction involved measuring the UV-vis and infrared absorption spectrum under continuous irradiation.[75,76] More recently ultrafast transient absorption spectroscopy has been used to measure the excited-state spectrum for a series of $Mn(CO)_3(^{L}bpy)Br$ complexes (L = tBu, H, CF_3) in acetonitrile after MLCT excitation. The excited-state quickly decays on the sub-ps timescale due to back electron transfer (BET) from the bpy ligand to an

unoccupied d-orbital of the Mn metal which has anti-bonding character in the Mn-CO bond, and releases a CO ligand to form an electron deficient 5-coordinate species. In acetonitrile, the electron deficient 5-coordinate species binds a solvent molecule to form a new 6-coordinate $Mn(CO)_2(^L bpy)(Br)(MeCN)$ complex. However, optical absorption relies heavily on interpretation of broad absorptive features and does not provide the detailed insight into the different Mn tricarbonyl structures that would be helpful in elucidating the decomposition reaction. Additionally, the the ultrafast measurements only examine the excited-state dynamics up to a few hundred ps, yet it is clear that additional steps in the decomposition chemistry occur on longer timescales.

In chapter 6 we examine the photodecomposition reaction using time-resolved x-ray absorption spectroscopy (TR-XAS) for a series of $Mn(CO)_3(^L bpy)Br$ complexes after MLCT excitation. TR-XAS probes the electron density on the Mn metal as well as structural evolution of the ligands around the Mn center. We modify the bpy ligand with -tBu, -H, $-CF_3$ and $-NO_2$ substituents in order to tune the MLCT band and examine the effect that changing the metal-ligand interaction has on the photodecomposition reaction. Dichloroethane (DCE) and acetonitrile (MeCN) solvents are used to change the decomposition mechanism and examine possible competing reactions. The results provide important new information about the photodecomposition pathway of the $Mn(CO)_3(^L bpy)Br$ catalyst.

1.3 Nanoplasmonics

Nanoplasmonics refers to optical phenomena involving sub-wavelength nanostructures, in which the optical energy remains concentrated on the nanoscale due to localized surface plasmons.[77] For nanostructure systems rich in electron density, such as silver or gold, an optical electric field drives oscillations of the electron density within the nanostructure at the frequency of the incident field.[78] As the electron density oscillates, an induced electric field stronger than the incident electric field occurs in the environment surrounding the nanostructure.[79] Earlier studies used classical electrodynamics to investigate the enhanced electric field of isolated silver nanoparticles and pairs of nanoparticles separated by a few nanometers.[80] By modeling the system, it was found that the

nanoparticles exhibited distinct dipole, quadrupole and higher multipole plasmon resonances. Exciting those resonances would create an external electric field stronger than the incident field. The electric field enhancement is generally expressed as the square of the electric field ($|E|^2$) due to its proportionality to the intensity of light. It was found that isolated nanoparticles with triangular prisms, oblate spheroids and cylindrical rod structures all have a similar $|E|^2$ enhancements on the order of 10^4. For dimer structures with 2 nm separation the $|E|^2$ enhancement increased to 10^5, however the enhancement is sensitive to the distance between the nanoparticle. The easily tunable near-field environment led to a plethora of different structures with applications in surface enhance Raman spectroscopy (SERS) for low signal detection,[81,82] light harvesting solar cells to boost the conversion efficiency,[83–85] and driving photochemical reactions under low light conditions.[86–89]

The electric field enhancement is not the only interaction to occur between the plasmonic nanostructure and its surroundings, other interactions such as thermal heating and electron transfer can arise.[90] In the mechanism for thermal heating the oscillating surface plasmons interact with the lattice of the nanostructure through electron-phonon interactions. This interaction puts energy into the nanostructure as lattice vibrations, which then diffuses into the surrounding medium.[91] Alternatively, an electron in the nanostructure could get transferred from the metal to the surrounding medium.[90] To understand the near-field environment and the effect on a chemical systems requires the consideration of all energy and electron transfer pathways.

Chapter 7 of this dissertation is motivated by a ground breaking experiment by Tsuboi and coworkers,[86] which showed the enhanced near-field environment inducing a two-photon excitation process for a photochromic molecule deposited as a thin film over the nanoparticles using a low intensity continuous wave laser. The authors concluded that electric field enhancement between adjacent gold nanospheres was strong enough in the near-field to drive the photoisomerization reaction via non-resonant two-photon excitation from the 808nm CW laser source, based on a quadratic power-dependence for the change in absorbance after 15 min. Similar approaches to investigating nanoplasmonics included photochromic switching in solid and solution phase,[87,88,92,93] attaching molecules directly to the nanoparticle,[89,94–97] and structurally changing the size and shape of the

nanoparticles to alter the enhanced field.[98–101]

However, the details about the interactions between the nanostructure and the photochromic system remain unclear, therefore we investigate the photochromic switching on a periodically spaced gold nanorod array under one and two-photon excitation conditions. The regularity of the plasmonic array provides a well-defined substrate to convert the DAE thin film as well as a consistent electric field enhancement across the array compared with randomly placed nanospheres. Additionally, the aligned array allows the enhancement to be tuned based on incident field polarization with respect to the orientation of the aligned nanorods. For a more detailed understanding of how the photochromic reaction progresses around the plasmonic nanostructure, the conversion of DAE is simulated using calculated near-field intensities of the incident and probe light by solving the Maxwell equations. Combining the information from the experiments and simulations provides a detailed understanding for the near-field interactions between a plasmonic nanostructure and the photochromic molecules.

Chapter 2

Experimental Methods

2.1 Overview

The reaction dynamics and kinetics in this dissertation are probed using time-resolved transient spectroscopy techniques that use a two-beam design with a pump pulse and a probe pulse. For optical pump-probe spectroscopy measurements an initial pump pulse is used to generate an excited-state population of molecules, which then propagate along a reactive coordinate on the excited-state potential energy surface. Using an optical probe pulse, we monitor the evolution of the excited-state absorption spectrum. The evolution of the excited-state absorption provides insight into mechanisms and timescales for different molecular reactions such as *cis*→*trans* isomerization or decomposition reactions. To gain more structural information about the excited molecule along a reactive pathway the optical probe is exchanged for a hard x-ray probe, which is produced in the storage ring of the Advanced Photon Source at Argonne National Lab. The hard x-ray probe is tuned to the K-edge of a metal that is sensitive to the ligand identity and molecular structure. Many of the experimental details are already discussed within each chapter, therefore the emphasis of this chapter will be the technical aspects of the experiments that are not described elsewhere.

2.2 Ultrafast Optical Transient Absorption Spectroscopy

Broadband TA measurements use the modified output of a 1 kHz regeneratively amplified Ti:sapphire laser (Legend Elite, Coherent), which produces 35 fs laser pulses at 800 nm. A portion of the 800 nm laser light can be passed into an optical parametric amplifier with two stages of nonlinear fre-

quency conversion (TOPAS) to produce pump pulses in the range of 260-2600 nm. The broadband white light (WL) probe pulses with a range of 360-980 nm are made by focusing the 1280 nm signal from a home-built optical parametric amplifier (OPA) into a circularly translating CaF_2 crystal. A pair of reflective parabolic mirrors collimates, then focuses the probe beam at the sample, after which a transmission grating disperses the probe light onto a 256-element photodiode array.

The photodiode array stores the intensities on each pixel as a voltage, which is collected using a data acquisition (DAQ) card. The DAQ card is synchronized with the 1 kHz signal from the Ti:sapphire laser, which allows each WL pulse to be captured and processed for shot-to-shot detection. More details regarding the setup can be found in the dissertation of Cassandra Ward.[102] To calculate the excited-state absorption, alternating measurements with the pump beam on the sample are performed using a synchronized optical chopper. The alternating WL intensities with the pump pulse blocked by the chopper (I_{OFF}) and the pump pulse on the sample (I_{ON}) are used to calculate the change in absorbance (ΔA), shown in equation 2.1. The time-dependence of the excited-state absorption comes from the delay time between the pump and probe pulses.

$$\Delta A(t) = -log(\frac{I_{ON}(t)}{I_{OFF}}) \tag{2.1}$$

2.3 Transient X-ray Absorption Spectroscopy

The TR-XAS measurements were carried out at the Advanced Photon Source (APS) on beamline 7ID-D, using an optical pump and a x-ray probe setup.[103] The pump pulse is derived from the output of a tunable high repetition rate laser (time-Bandwidth Products, Duetto) with a center wavelength of 1064 nm and a duration of 10 ps. By focusing the output into a lithium triborate (LBO) nonlinear crystal(s) the second and third harmonic at 532 nm and 355 nm are generated respectively. The high repetition rate laser is synchronized with x-rays produced in the storage ring of the APS operating in the 24 bunch mode. In 24 bunch mode the circular storage ring has 24 circulating electron bunches, with a 153 ns spacing between each bunch, which equates to an x-ray pulse repetition rate of 6.52 MHz. The x-ray energy is tuned across the 6.510-6.905

keV range using an undulator with a water-cooled double crystal diamond (111) monochromator and focused using Kirkpatrick-Baez mirrors into the sample with a spot size of $\sim$5 μm full width at half max.[104,105] For the transient x-ray absorption measurements the samples are setup for a single pass through a liquid jet with thickness of $\sim$100 μm at 2.5 mL/min in order to prevent contamination of the signal from irreversible photoproducts.[103] Close to the sample, avalanche photodiodes with Z-1 chromium filter are set up 90 degrees from the incoming x-ray beam to detect the x-ray fluorescence of the sample and are capable of capturing the fluorescence after each x-ray pulse.[103] The fluorescence signal is typically averaged with 10^6 pulses per energy point. Due to the higher repetition rate of the x-ray probe pulses compared to the optical pulses, 13 additional x-ray pulse pass before the next optical pump pulse. Figure 2.1 illustrates the timing sequence between

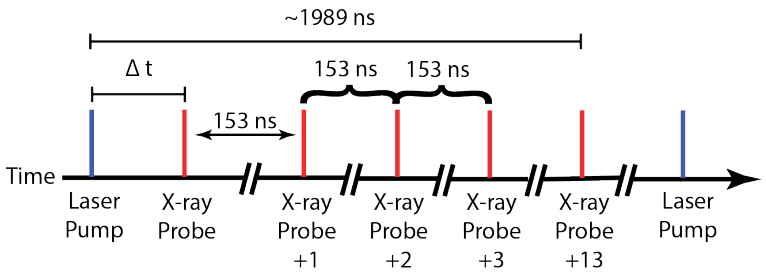

Figure 2.1: Laser timing diagram for the pump and x-ray probe sequence.

the laser pump pulse and the x-ray probe pulses. The delay between the laser pump pulse and the x-ray pulse is controlled electronically using a programmable delay line (Gigabaudics, PADL3-5-12-15355) which shifts the phase of the rf signal from the synchrotron producing. The shifted phase of the rf signal results in a shift of the laser pump pulse in time. We take advantage of the extra pulses by recording the fluorescence after each additional x-ray pulse providing incremental 153 ns delay times up to 1989 ns.

2.4 Transmission Measurements Using a Pulsed Laser

Pulsed laser light is generated using the amplified Ti:sapphire laser described above. White light continuum laser pulses are made by focusing the 800 nm fundamental into a cuvette of water. The white light beam is split using a 50% beam splitter into a signal and a reference beam. The

signal beam is focused down to 60 µm at the point where it passes through the plasmonic array. The reference beam accounts for fluctuations of the incident probe intensity when calculating the absorption. After the sample, the broadband signal and reference beams are dispersed using a transmission grating onto an 8 bit CMOS camera (Thorlabs), with dimensions of 1280 x 1024 pixels to calculate normalized intensity/absorption as a function of wavelength over the range 400-650nm. The integration time for the camera is set to 40 ms. To decrease the readout time from the CMOS camera, the range of pixels recorded is reduced to 1280 x 200 pixels for the dispersed signal and reference regions on the camera. Mechanical shutters are used to control the duration of white light and 800 nm exposure of the sample.

2.4.1 Mechanical Shutters

In order to control the light exposure on the sample, mechanical shutters (CVI Laser Optics) were installed in the beam path for the white light probe and the 800 nm conversion light. The shutters were powered using an external battery pack 6V (4 x AA), and have a response time of 60 ms for completely opening and closing the aperture. The slow response time of the shutter compared to the laser repetition rate is addressed in the CMOS camera section below. For the shutters to close they require an electronic TTL signal (>3V) which was supplied by a breakout-box, which is controllable with labview software. Figure 2.2 shows a simple Labview scheme for controlling the

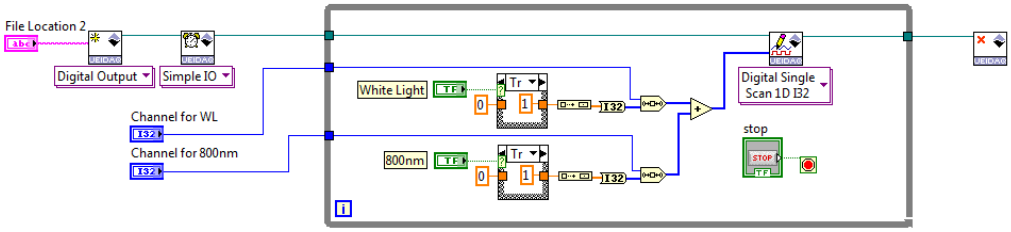

Figure 2.2: Laview diagram for the basic workings of the mechanical shutters.

shutters. "File location 2" is the path for accessing the DAQ card responsible for communicating with the breakout box. The channels for "WL" and "800 nm" are the designated channels on the

breakout box connected to the shutters in the WL and 800 nm beam lines respectively. Passing a 1 or 0 in the correct format to the Digital Single Scan VI will have the break-out box send the TTL signal to the corresponding shutter.

2.4.2 CMOS Camera

The CMOS camera (Thorlabs, DCC1545M) is a 1.3 megapixel charge coupled device (CCD) with a rolling electronic shutter. The max readout speed is 40 ms and the detector is connected to the data acquisiton computer through a USB 2.0. Labview software was written to communicate with the CMOS camera using VIs from the ThorLab website. The VIs named ExpTime, SetFPS and SetPiCI need to be set to appropriate values in order for the camera to function. In the experiments the ExpTime VI is set to 40 ms, which integrates over 40 ms. The GetImage VI gets the counts from the CCD detector. In the code, the user can specify how many frames of 40 ms integrated time they would like to average for the WL measurement. For example, to have 1 second of averaged WL, the number of frames should be set to 25 (40 ms x 25). Due to the shutter closing rate (60 ms) being slower than the camera readout (40 ms), two additional frames are added at the beginning and end of the frame sequence, which allow time for the shutter to open and close. Therefore, in the previous example with 25 frames, the actual frames recorded is 29, but the two in the beginning and two at the end are dropped due to the shutter clipping the pulse. Output files are stored as text documents.

Chapter 3

Ultrafast Dynamics of Encapsulated Molecules Reveals New Insight on the Photoisomerization Mechanism for Azobenzenes

(A version of this work was published as reference 5)

3.1 Introduction

Nature makes use of steric constraints to guide the early stages of many light-activated biological responses.[17] For example, many light-sensitive biological functions, including vision and phototaxy, begin with *cis-trans* photoisomerization in the spatially confined active site of a protein, where steric and other interactions determine the ultrafast reaction dynamics.[18–21] Similar to the way some proteins drive isomerization around a specific C=C or N=N double bond of a chromophore, synthetic cavities present an opportunity to selectively manipulate the dynamics of photochemical reactions by influencing the structural rearrangement of a molecule,[23,27,35–37,106–108] or even pre-aligning the reactants in a bimolecular reaction.[109,110] Reactions in confined environments not only open the possibility of new applications, but also provide a window on the underlying details that control the reaction dynamics.[38]

In this chapter, we use ultrafast spectroscopy to study the influence of a restricted environment on the *trans*→*cis* photoisomerization dynamics of 4-propyl stilbene (4PrSt) and 4-propyl azobenzene (4PrAz) encapsulated in a supramolecular organic cavitand.[36] Stilbene and azobenzene derivatives are prototypical photochromic compounds that are ubiquitous in applications where environmental effects could alter the reaction dynamics, including biological triggers and

probes,[111–116] molecular machines,[117,118] and photochromic materials.[119–122] Photoisomerization reactions are particularly sensitive to steric constraints, due to the large amplitude motions required for structural rearrangement. While the photoisomerization mechanism for stilbene derivatives requires out-of-plane rotation of the phenyl rings around the central C=C double bond, the mechanism for azobenzene is complicated by possible contributions from both rotation and in-plane inversion pathways.[123,124] We show below that confining these molecules within an appropriately sized cavity provides a window on the isomerization mechanism by restricting the rotation of the phenyl rings around the double bond. We observe a bifurcation between *cis* and *trans* isomers in the excited state of azobenzene that indicates a new excited-state inversion pathway that is not observed in solution.

The host-guest complexes that we study spontaneously self-assemble in aqueous solution by incarcerating a single stilbene or azobenzene molecule in the hydrophobic cavity formed by two cavitand molecules. The synthesis of the cavitand molecule, known as octa-acid (OA), and the preparation of OA_2 dimer complexes encapsulating a hydrophobic chromophore were reported elsewhere, along with detailed studies of the photochemistry inside the capsules based on steady-state measurements.[36,125–129] Stilbene and azobenzene derivatives are known to isomerize in the OA_2 capsules,[125–127] but the ultrafast excited-state dynamics have not been studied previously. In this study, we use propyl-substituted stilbene and azobenzene, because the inert alkyl chain causes additional crowding inside the capsule, and therefore exacerbates the effects of the confined environment. We note that alkyl-substituted stilbene and azobenzene have essentially the same isomerization mechanisms as the unsubstituted counterparts in solution. However, unlike solution, the *cis* isomers are the more stable structure in the capsule because crowding disproportionately destabilizes the longer *trans* isomers.[126]

3.2 Experimental Methods

The compounds OA, 4PrSt, and 4PrAz were synthesized and purified as previously reported.[125,127] Samples consist of 1 mM solutions of 4PrSt or 4PrAz in cyclohexane, or $\sim$ 0.5 mM aqueous solu-

tions of the encapsulated compounds. We make the self-assembled 4PrSt@OA_2 and 4PrAz@OA_2 complexes by sonicating 2 eq. of OA with 1 eq. of stilbene or azobenzene derivative for 30 min in water. All samples are in a 1 mm quartz cuvette.

The transient absorption (TA) and quantum yield (QY) measurements use the modified output of a regeneratively amplified Ti:sapphire laser (Legend Elite, Coherent) operating at 1 kHz. An optical parametric amplifier (OPA) with two stages of nonlinear frequency conversion (TOPAS) produces 320 nm pump pulses for both measurements. For the TA measurements, the pump beam passes though a synchronized chopper to block every other pulse for active background subtraction, and a zero-order $\lambda/2$ waveplate rotates the polarization for parallel and perpendicular orientation with respect to the probe. We attenuate and focus the pump beam to $\sim$ 120 nJ/pulse and a diameter of $\sim 200\mu m$ at the sample. Focusing a small amount of the 1200 nm signal from a second, home-built OPA into a circularly translating CaF_2 crystal produces broadband probe pulses in the range of 340-990 nm. A pair of parabolic mirrors collimate and focus the probe into the sample, where it intersects the pump at a small angle and variable time delay. We continuously translate the sample for the TA measurements in order to avoid accumulation of photoproduct in the focal volume. After passing though the sample, a prism disperses the probe light onto a 256-element photodiode array for shot-to-shot detection. We average 10^3 laser pulses per time delay for three consecutive scans for each TA measurement.

We measure *trans* $\rightarrow$ *cis* photoisomerization quantum yields ($\Phi_{t\rightarrow c}$) by measuring the change in transmission of UV laser pulses through a static sample as a function of time.[130] For both compounds, the *trans* isomer has appreciable absorption at the excitation wavelength, but *cis* does not; therefore the decrease in transmission through the sample reveals the number of molecules that isomerize. We obtain the quantum yield from the ratio of the conversion rate to the excitation rate (*i.e.* the relative change of transmission over time compared with the absolute transmission of 320 nm pulses). In order to account for small fluctuations of the laser intensity, we split the attenuated pump light into signal and reference beams with a 50% beam splitter, and then pass the former through the sample with a diameter of 1.5 mm and an incident energy of 2.5 nJ/pulse. We

measure the pulse energies of the transmitted signal and reference beams using identical integrating photodiodes at 1 kHz.

3.3 Results and Discussion

The chemical structure of OA is shown as an inset in the top panel of figure 3.1, along with the absorption spectrum of the OA_2 dimer capsule formed by encapsulating an optically transparent and chemically inert adamantane molecule. The lower two panels of the figure show the spectra of encapsulated *trans*-4PrSt and *trans*-4PrAz, respectively, as well as the spectra of the two chromophores dissolved in cyclohexane. The absorption band of OA is centered near 280 nm, and partially overlaps the ground-state absorption of 4PrSt and 4PrAz. The absorption spectra of both compounds become slightly broader and have less vibronic structure upon encapsulation, suggesting that both molecules are distorted in the capsule. Molecular dynamics calculations for encapsulated *trans*-stilbene derivatives indicate a slightly twisted structure in the ground state, compared with a planar ground state in solution.

Figure 3.2 shows the evolution of the transient absorption (TA) spectra following $\pi \rightarrow \pi*$ excitation of 4PrSt and 4PrAz at 320 nm, where there is no absorption by the OA_2 capsule. The figure shows the evolution of the TA spectra in cyclohexane (upper panels) and inside the capsule (middle panels), with the lower panels comparing the decay of the excited-state absorption bands as a function of time for each environment. Notice the different timescales for the two compounds.

The figure shows the isotropic TA spectra that we calculate from separate measurements with parallel and perpendicular polarization of the pump and probe light, $\Delta A_{iso} = (\Delta A_{||} + 2\Delta A_{\perp})/3$, in order to eliminate contributions from rotational reorientation. From the same set of measurements, we also calculate the anisotropy, $r(t) = (\Delta A_{||} - \Delta A_{\perp})/(\Delta A_{||} + 2\Delta A_{\perp})$, which provides a measure of the reorientation time for molecules in the excited state. The decay of the anisotropy reveals significantly slower reorientation in the capsules compared with solution (see figure 3.3), with the entire complex rotating on a $\sim$ns timescale, compared with tens of ps for the freely solvated molecules. Slower reorientation confirms that 4PrSt and 4PrAz are incarcerated in OA_2, and that

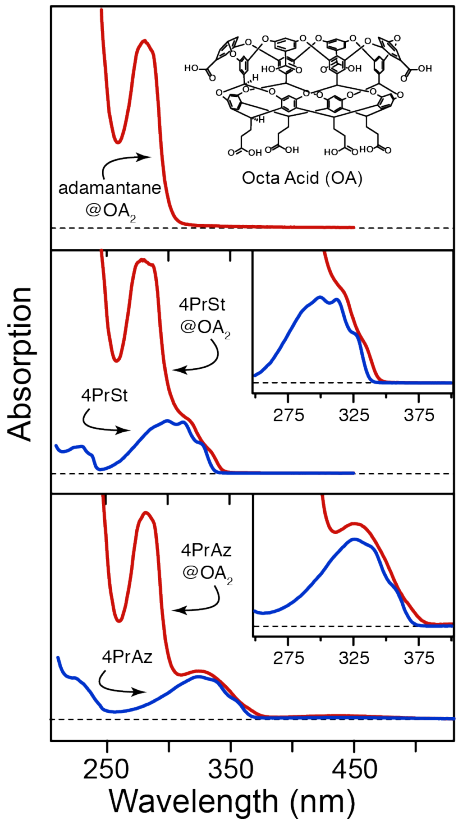

Figure 3.1: Absorption spectra of octa-acid complexes: adamantane@OA_2 (top), 4PrSt@OA_2 (middle), and 4PrAz@OA_2 (bottom). Lower panels also show the spectra of 4PrSt and 4PrAz in cyclohexane.

they do not rotate inside of the capsule.

Similar to unsubstituted stilbene,[130,131] the TA spectrum of 4PrSt in cyclohexane has a strong S_1 excited-state absorption (ESA) band centered near 580 nm that shifts and narrows slightly on a timescale of 1.3 ± 0.3 ps due to structural relaxation and vibrational cooling, and then decays with a single exponential lifetime of 86 ± 3 ps. The TA spectrum of encapsulated 4PrSt (4PrSt@OA_2) is similar to the solvated compound, except for a slight blue-shift and broadening of the ESA band, and a significantly longer excited-state lifetime of 384 ± 4 ps. The broadening of the ESA band in the capsule suggests either a more distorted structure or a broader distribution of structures compared with solution, similar to what we observe in the ground-state spectrum and simulations.

The isomerization mechanism for stilbene has been well-studied in solution.[123,131,132] After $\pi\pi^*$ excitation to S_1, stilbene molecules cross a small barrier along the torsional rotation coordinate

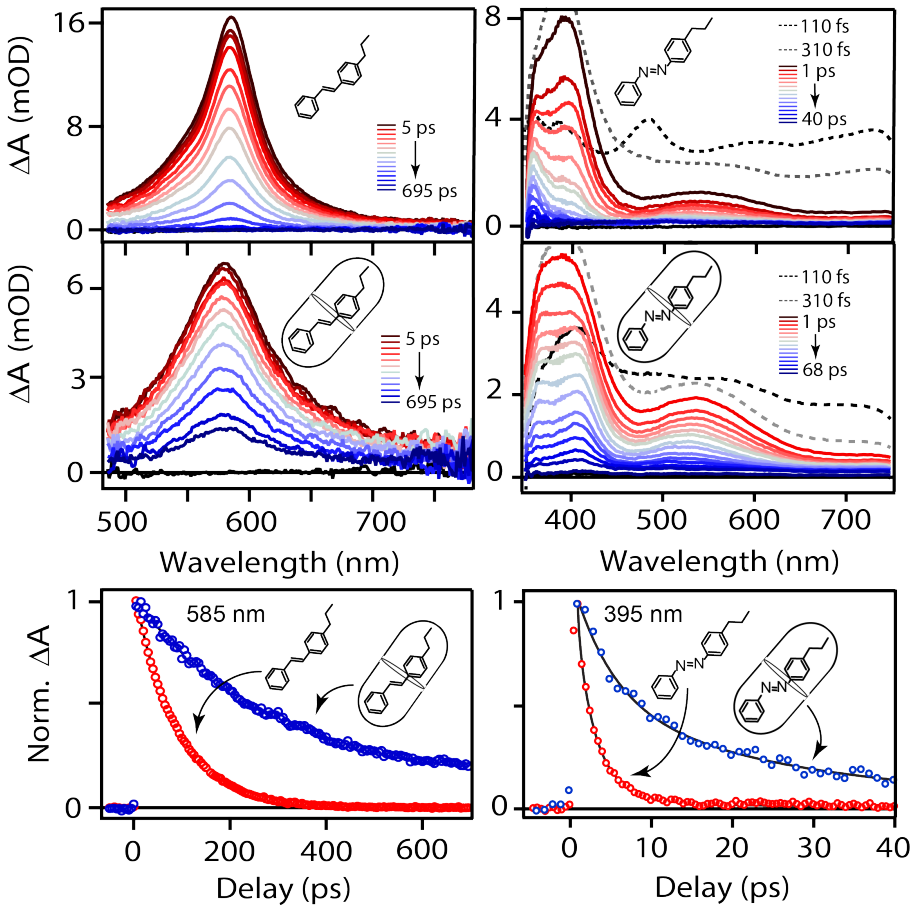

Figure 3.2: Evolution of the TA spectra of 4PrSt (left side) and 4PrAz (right side). Top and middle panels show the spectra in cyclohexane and in the OA_2 capsules, respectively. The lower panels compare the decay of the signals in the two environments, with the lines showing fits to the data using the models described in the text.

before reaching a perpendicular geometry, where there is a conical intersection (CI) that brings the molecule back to the ground electronic state.[133] The excited-state lifetime for many stilbene derivatives is on the order of tens of ps, depending on the solvent, and has been successfully described in terms of either solvent viscosity inhibiting the relative rotation of the phenyl rings, or with a solvent stabilization model where the polarity of the solvent affects the activation energy to reach the CI at perpendicular geometry.[123,134] Either way, the longer excited-state lifetime for 4PrSt@OA_2 is most likely due to restricted rotation around the C=C bond.

Passage through the CI determines the branching between *trans* and *cis* isomers when molecules return to the ground state. For stilbene in solution, this branching leads to nearly equal populations

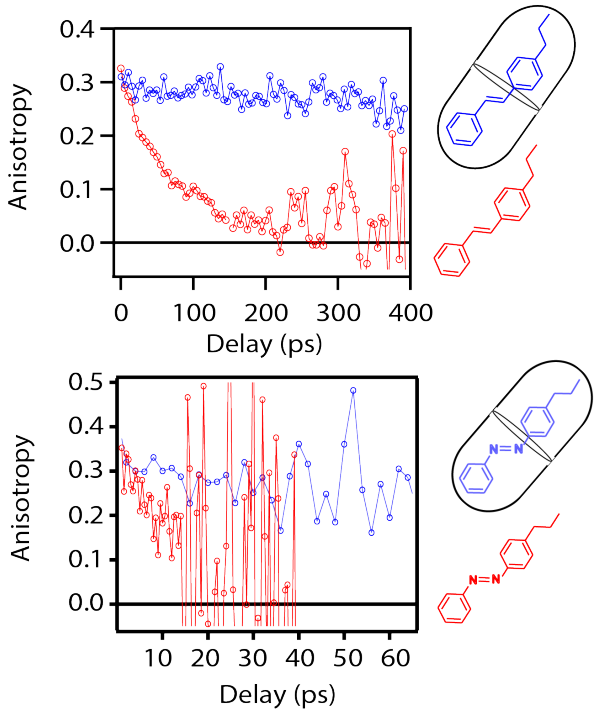

Figure 3.3: Anisotropy decay for 4PrSt/cyclohexane and 4PrSt@OA_2 (top panel), and 4PrAz/cyclohexane and 4PrAz@OA_2 (bottom panel).

of the two isomers. Importantly, the quantum yield ($\Phi_{t\rightarrow c}$) for *trans*→*cis* isomerization of stilbene is relatively insensitive to the identity of the solvent,[130,132,135] indicating that solvation does not directly affect the topology of the S_1-S_0 conical intersection. However, we find that encapsulation in OA_2 decreases $\Phi_{t\rightarrow c}$ by nearly half, from $42 \pm 6\%$ in cyclohexane to only $24 \pm 6\%$ in the capsule. The significantly lower quantum yield suggests that confinement impacts either the dynamics through the CI, or the topology of the CI itself. For example, the encapsulated molecule may pass through a CI (or a region of the conical seam) that is shifted toward the *trans* geometry due to destabilization of the perpendicular structure.

The excited-state lifetime of 4PrAz is much shorter than 4PrSt, with the former also following a more complex pathway that requires fits to the data with at least four time constants in solution and five in the capsule. One key difference between the two compounds is that excitation at 320 nm accesses the $S_2(\pi\pi^*)$ state of 4PrAz, which rapidly relaxes to the lower-lying $S_1(n\pi^*)$ electronic state. The ESA spectrum of S_2, which is evident only within the first ~300 fs of the TA spectra

for 4PrAz and 4PrAz@OA_2 (dashed lines in figure 3.2), extends across the entire probe range, with broad bands centered near 490, 600 and 710 nm. Similar to previous reports for unsubstituted azobenzene, the S_2 absorption is rapidly replaced by the S_1 absorption bands near 400 and 530 nm, which then decay within a few ps.[136]

In contrast with stilbene, the isomerization mechanism for azobenzene derivatives remains controversial, because of the competing pathways involving torsional rotation and in-plane inversion at one (or both) of the nitrogen atoms. The limit of rotational isomerization involves torsion around the N=N bond to reach a conical intersection with the ground-state at perpendicular geometry, similar to stilbene; however, azobenzene can also isomerize through an inversion pathway via rehybridization of the non-bonding electrons and in-plane bending of a phenyl ring along the Ph-N=N coordinate.[137–141] Based on the relative electronic structures of the first two excited states, early studies suggested that $n \rightarrow \pi^*$ excitation to S_1 would result in primarily an inversion mechanism, whereas $\pi \rightarrow \pi^*$ excitation to S_2 would result in primarily a rotational mechanism analogous to stilbene photoisomerization. However, more recent experimental and theoretical work indicates that a simple, single-configuration view of the excited states does not adequately describe the isomerization dynamics of azobenzene, but rather the dynamics involve an "inversion-assisted rotation" mechanism that requires concerted motion along both coordinates, even for excitation to the lower-energy $n\pi^*$ state. The situation is further complicated for $\pi\pi^*$ excitation at higher energy, because additional isomerization and relaxation channels are available in the vibrationally excited S_1 state after internal conversion from S_2.[136] Very briefly, the lowest-energy isomerization pathway on S_1 begins with in-plane motion along the inversion coordinate, and then involves some degree of rotation to access a conical seam that returns the system to the ground state. Different regions of the conical seam involving a larger degree of rotation are available at higher energy. (See the SI of reference 136 for an excellent historical review of the azobenzene isomerization mechanism.)

The top panel of Figure 3.4 shows a simplified schematic representation of the emerging mechanism for azobenzene photoisomerization following $\pi \rightarrow \pi^*$ excitation to S_2,[136,142] including the

lifetimes that we extract from global fits to the TA data for 4PrAz in cyclohexane. The fastest timescale of ∼50 fs is due to relaxation from S_2 to S_1, followed by ∼260 fs relaxation of the "hot" S_1 state. While a portion of the molecules relax into a minimum-energy geometry on the S_1 surface, a large fraction of the "hot" molecules reach the ground state on a timescale that competes with vibrational relaxation in S_1.[143] The result is a roughly biexponential decay of the ESA signal on timescales of ∼0.26 ps for the "hot" reacting molecules and ∼2.4 ps for molecules that relax on S_1 before overcoming the small barrier along the minimum energy path. Molecules return to the ground state through a CI that determines the relative branching between *cis* and *trans* isomers. Molecules that return to the *trans* structure in the ground state contribute a transient absorption feature below 400 nm that decays on a timescale of ∼ 10 ps due to vibrational relaxation and cooling in S_0.[142–145]

We model the evolution of the TA spectrum of 4PrAz in cyclohexane based on the above kinetic mechanism. Our fits to the data restrict the relative amplitudes at each wavelength according to the kinetic model in order to extract the species-associated spectra (SAS) in the top panel of figure 3.5. The SAS represent distinct populations of 4PrAz along the reaction path, including molecules in the initially excited S_2 state, the hot and relaxed S_1 states (S_1^* and S_1, respectively), and the vibrationally hot ground state of the *trans* isomer (S_0^*). The ground-state of the *cis* isomer and the relaxed S_0 state of the *trans* isomer do not contribute to the absorption in our probe window.

The spectra obtained from the fits support the proposed mechanism from above. In particular, the spectra for S_1 and S_1^* are very similar, with the latter characterized by additional broadening, which is typical for highly vibrationally excited molecules.[130,146] In other words, the relaxation of S_1^* leads to a narrowing of the ESA band, as well as a decrease of intensity in the TA signal due to the competing reaction channel directly from S_1^* to the ground state. The fits indicate that ∼ 60% of the "hot" molecules relax directly to the ground electronic state in cyclohexane.

The TA spectrum of confined 4PrAz (4PrAz@OA_2) is similar to the spectrum in solution, except for a few notable differences, including different relative intensities of the ESA bands near 400 and 530 nm, slight broadening of the bands, and a significantly longer excited-state lifetime.

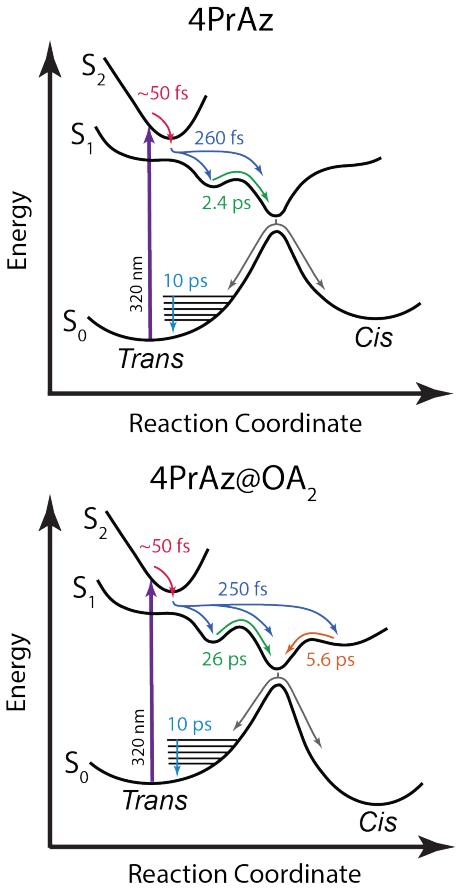

Figure 3.4: Cartoon illustration of the potential energy surfaces for 4PrAz and 4PrAz@OA_2. Arrows indicate reaction path following $\pi \rightarrow \pi^*$ excitation. Lifetimes are from global fits to the data using the kinetic model described in the text and in figure 3.5.

The differences between the two environments in many ways mirror the results for 4PrSt. However, global fits to the data for 4PrAz@OA_2 require at least five exponential time constants, compared with only four in solution. The extra lifetime indicates that there are two distinct excited-state species. Using the mechanism for azobenzene in solution as a starting point, we attempted to model the evolution of the TA spectrum of 4PrAz@OA_2 using several different kinetic schemes, but only a mechanism that includes parallel kinetics with two distinct excited-state species (in addition to S_1^*) gives a reasonable fit to the data. The successful model is represented by the schematic diagram in the lower panel of figure 3.4, and produces the SAS in the bottom panel of figure 3.5.

The SAS for the S_2 state of 4PrAz@OA_2 is similar to the S_2 spectrum in solution, except for

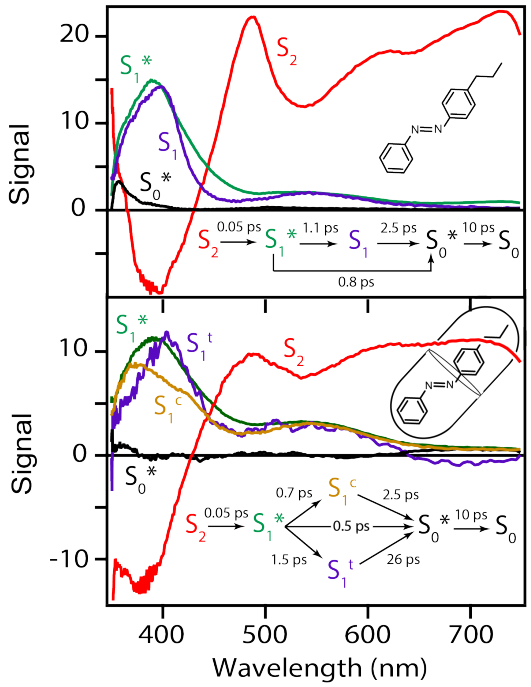

Figure 3.5: Species associated spectra (SAS) from global fits to the TA spectra for 4PrAz in cyclohexane (top) and 4PrAz@OA_2 (bottom). The kinetic models are shown as insets, and match the schematic diagrams in figure 3.4.

significant broadening of the ESA band near 490 nm that probably reflects a distorted geometry in the confined environment of the capsule. Relaxation to S_1^* occurs on a similar sub-100 fs time scale (we fix this time constant at 50 fs in our fits based on recent results from Nenov, *et al.*[136]), and both the spectrum and relaxation time of S_1^* that we recover from the fits in the capsule are similar to those in solution, indicating that the dynamics at very early delay times are relatively insensitive to confinement. However, a distinctive feature of the dynamics of 4PrAz@OA_2 is the relaxation of S_1^* into two different excited-state species, in addition to direct relaxation to the ground state. The two species have lifetimes of 5.6 ± 1.1 and 26 ± 2 ps.

Importantly, one of the spectra that we recover from the global fits has an ESA band with a maximum near 380 nm and a pronounced shoulder near 410 nm, which almost perfectly matches the excited-state spectrum of *cis*-azobenzene.[142] In separate TA measurements that will be reported in chapter 5, we observe the same, distinctive ESA band following direct $n \rightarrow \pi^*$ excitation of unsubstituted *cis*-azobenzene at 480 nm, both in solution and in the capsule. Therefore, we assign

the two excited-state species of 4PrAz@OA_2 as the relaxed S_1 states of the *cis* and *trans* isomers, S_1^{cis} and S_1^{trans}, respectively. In stark contrast with solution, this observation indicates that the confined environment allows the molecule to access the *cis* structure directly from the excited state of the *trans* isomer. This new excited-state isomerization pathway to S_1^{cis} is made possible by destabilization of the longer *trans* structure in the capsule.

The results for similarly sized 4PrSt show that the rotation channel is restricted in the capsule, therefore the excited-state isomerization to S_1^{cis} must follow a path primarily along the inversion coordinate. The important role of inversion in the isomerization of 4PrAz@OA_2 is further supported by an *increase* of the quantum yield $\Phi_{t\rightarrow c}$ from 12±3% in solution to 17±4% in the capsule (in contrast with the significant decrease of $\Phi_{t\rightarrow c}$ for 4PrSt). The larger quantum yield for isomerization of 4PrAz@OA_2 is a direct result of steric crowding inside the capsule that favors the *cis* geometry. In solution, the overall quantum yield for azobenzene depends on the initial excitation energy, with a photoisomerization yield for $\pi \rightarrow \pi^*$ excitation of unsubstituted azobenzene that is about half of the yield for $n \rightarrow \pi^*$ excitation of the same molecule at longer wavelengths.[147] The wavelength-dependence of $\Phi_{t\rightarrow c}$ in solution was attributed to a preference for the *trans* structure when molecules pass through a CI at higher energy. In other words, regions of the conical seam that are accessible at higher energy have a topology that increasingly favors a return to the *trans* structure in the ground electronic state.

Encapsulation restricts the motions available to an isomerizing molecule, and therefore drives the reaction through different regions of the conical seam compared with solution. The fits indicate that roughly half of the "hot" S_1^* molecules relax directly to the ground electronic state within the first few hundred fs, whereas molecules that remain in the excited state have a roughly 2:1 preference for the formation of S_1^{cis} over S_1^{trans}. Although we are unable to directly measure the quantum yields for each of the three pathways individually, there is likely to be a higher yield of the *cis* product from the *cis* excited-state. However, the modest increase of the overall quantum yield to only ∼17% in the capsule suggests that both "hot" S_1^* and the *trans* excited state preferentially return to the *trans* structure in S_0.

We extract lifetimes from the global fits of 5.6 ps for S_1^{cis} and 26 ps for S_1^{trans}. The excited-state lifetime of S_1^{trans} is $\sim$10 times longer in the capsule than in solution, indicating that the confined environment has a significant impact on the isomerization dynamics of 4PrAz, probably due to trapping the molecule in a distorted (*i.e.* non-planar) structure. We note that the ESA band of this species is red-shifted compared with solution, which may be a signature of the twisted structure in the capsule. A twisted geometry would inhibit photoisomerization of 4PrAz@OA_2 by restricting in-plane motion along the inversion coordinate, which was recently shown to be the initial motion along the minimum energy path of S_1.[136] Consistent with this assignment of the longer-lived ESA band as S_1^{trans}, direct excitation to the $S_1(n\pi^*)$ state of unsubstituted *trans*-azobenzene reveals a similar ten-fold increase of the exited-state lifetime inside the OA_2 capsule.

The new pathway to access S_1^{cis} following excitation to the $S_2(\pi\pi^*)$ state of 4PrAz@OA_2 is only available from the "hot" S_1^* excited state, and is made possible by the destabilization of the *trans* structure in the capsule. We note that the quantum yield does not increase for other alkyl-substituted azobenzenes, as we report in chapter 5. The unique increase of $\Phi_{t\rightarrow c}$ for 4PrAz@OA_2 is due to crowding in the capsule by the propyl substituent on one phenyl ring, combined with the flexibility of the unsubstituted phenyl ring to reorient within the capsule. In chapters 4 and 5, we examine the excited-state dynamics for a series of alkyl-substituted stilbene and azobenzene compounds to further elucidate the role that crowding in the capsule plays in determining the excited-state isomerization.

3.4 Conclusion

In summary, ultrafast spectroscopy reveals fundamentally different excited-state dynamics for 4PrSt and 4PrAz inside the cavity of a supramolecular organic cavitand than we observe for the same compounds in solution. The encapsulated molecules have longer excited-state lifetimes due to stabilization of distorted, nonplanar excited-state structures. While both 4PrSt and 4PrAz prefer the *cis* isomer in the capsule, only 4PrAz shows an increase of the quantum yield for *trans*$\rightarrow$*cis* photoisomerization. Specifically, confinement restricts out-of-plane rotation of the phenyl rings,

and therefore inhibits the photoisomerization of 4PrSt, whereas the inversion channel of azobenzene leads to a new excited-state isomerization channel for encapsulated 4PrAz that does not exist in solution. The new channel leading to the *cis* excited state following excitation of the *trans* isomer represents a fundamentally different behavior than has been observed before, and confirms the important role of inversion in the isomerization of azobenzene.

Chapter 4

Ultrafast *trans* to *cis* Photoisomerization Dynamics of Alkyl-Substituted Stilbenes in a Supramolecular Capsule

(A version of this work was published as reference 6)

4.1 Introduction

The environment plays an important role in determining the excited-state dynamics of photoactive molecules.[148–150] For example, solvation influences the reaction rates, yields, and sometimes even the identity of the products that form, simply by tuning the relative energy at key points along a reaction path.[9–13] Confined environments provide an even more direct influence on reaction dynamics by restricting the motions of the atoms in the reacting molecule through steric restrictions and other interactions with the surroundings.[22–24] Examples of confined environments include the active sites of proteins,[14–16] nanoporous materials, and self-assembled structures ranging from reverse micelles to the cavities of extended molecular frameworks,[28–34] many of which have evolved or are designed to control the reactions and/or optical properties of enclosed molecules. Manipulating the dynamics of the chromophore in a photoactive protein, for example, is essential for controlling the early steps in vision,[20,151] phototaxy,[152] and other light-responsive biological functions.[153,154] Studying the dynamics of molecules in a confined environment also offers valuable insight on fundamental reaction dynamics.[5]

Stilbene is a model system for photoisomerization that has been studied extensively.[7,8,44–55] The well-known *trans*→*cis* isomerization mechanism requires rotation of the phenyl rings around

the central C=C bond axis after excitation to the $S_1(\pi\pi^*)$ state.[45,46] The excited-state lifetime of *trans*-stilbene is typically in the range of several tens of ps, depending on the identity of the solvent, and is limited by a torsional barrier that inhibits the molecule from reaching the perpendicular geometry, where there is a conical intersection (CoIn) with the ground state. Nonpolar solvents tend to impede the barrier crossing, and therefore increase the excited-state lifetime as a function of increasing solvent viscosity,[7,8,49–51] whereas polar solvents tend to accelerate the reaction by lowering the barrier through polarization stabilization.[155,156]

Passage through the CoIn determines the branching between *trans* and *cis* isomers in the ground state, and therefore plays a critical role in determining the quantum yield of the reaction.[53] Unlike the excited-state lifetime, the photoisomerization quantum yield for stilbene is relatively insensitive to the identity of the solvent, and leads to roughly equal populations of the two isomers. The roughly equal branching between *trans* and *cis* suggests that the conical intersection is relatively symmetric with respect to the two ground-state structures, which is consistent with a minimum-energy CoIn at the perpendicular geometry. There is also a local minimum at or near the perpendicular geometry region of the potential energy surface, often called the "phantom" or p^* state.[45,54] This minimum-energy state was recently observed for *cis*→*trans* isomerization, and is very short lived due to the proximity of the CoIn.[156–158]

There is growing interest in studying photoisomerization dynamics in confined environments. Studies involving stilbene and related molecules trapped in synthetic host-guest complexes promise to offer new insight on the role of external forces (i.e. steric interactions) in selectively controlling reaction dynamics, fluorescence yields, and other properties of a chromophore.[56–58] On one hand, host-guest interactions that distort the ground-state structure of a molecule can enhance specific reaction or relaxation channels by accessing a more favorable region of the excited-state potential energy surface upon excitation.[159] For example, a tight-fitting cavitand was recently shown to suppress the fluorescence of encapsulated stilbene by rotating the molecule sufficiently far along the C=C rotation axis in the ground state that optical excitation avoids the torsional barrier in the excited state.[56] The excited molecule relaxes directly through the perpendicular CoIn to the

ground-state without time to fluoresce. Other host-guest interactions are less disruptive of the ground-state structure, and instead restrict the motions of the molecule in the excited state.[160]

The host-guest complex in this study consists of a supramolecular 'octa acid' (OA) cavitand encapsulating the series of alkyl-substituted stilbene derivatives in Figure 4.1. Water-soluble OA spontaneously forms a dimer capsule that incarcerates hydrophobic guest molecules, denoted guest@OA_2.[39,40] The interior of the OA_2 complex fits only a single stilbene molecule. The confined molecule has limited space to translate and rotate, but retains the ability to photoisomerize, as has been shown in extensive steady-state measurements.[40–43] Importantly, the addition of alkyl substituents changes the relative size and shape of the incarcerated molecule, which affects the relative stabilities of the *trans* and *cis* isomers, as well as the ability to photoisomerize around the central ethylene bridge. For example, competitive encapsulation studies show that the *cis* isomer becomes relatively more stable in the capsule with increasing chain length for a series of 4-alkyl stilbenes.[43] Encapsulation also affects the isomerization dynamics, leading to different photo-stationary states (PSS) in solution and in the capsule. The difference can be quite large, as in the case of 4,4'-dimethyl stilbene, where PSS shifts from 18:76 in favor of the *cis* isomer in cyclohexane solution to 80:20 in favor of *trans* in the OA_2 capsules.[42] In order to probe the excited-state dynamics directly, we recently measured the ultrafast spectroscopy of 4-propylstilbene and the closely related 4-propylazobenzene in the OA_2 capsule, and showed that the confined environment leads to adiabatic isomerization in the excited-state of the azobenzene compound.[5]

In this chapter, we examine the photoisomerization dynamics of encapsulated *trans*-stilbene (**1**) and six alkyl-substituted derivatives (**2**-**7**). Specifically, we use ultrafast spectroscopy to probe the excited-state dynamics, and measure the isomerization and fluorescence quantum yields of each compound in cyclohexane and inside the aqueous OA_2 capsule. We also use molecular dynamics (MD) simulations to examine the structures and relative binding energies for OA_2 complexes containing the *trans* and *cis* isomers of each compound. The combined information from these different approaches provides new insight on the photoisomerization dynamics of confined molecules.

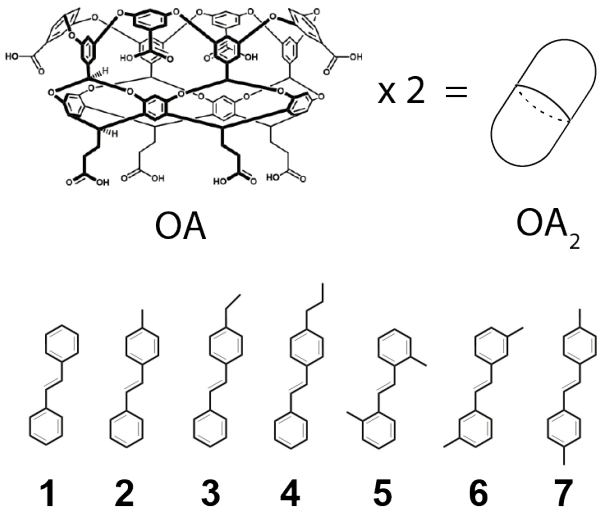

Figure 4.1: Structures of the octa acid (OA) capsule and stilbene derivatives.

4.2 Methods

Trans-stilbene (**1**) was purchased from Sigma Aldrich (>99%) and used without further purification. Compounds **2-7** and the octa acid (OA) capsules were synthesized and purified as previously reported.[42,43,161] The encapsulated samples were prepared by sonicating each compound with 2 eq. of OA in water until the compound was fully dissolved and the solution turned clear. NMR spectroscopy confirms the formation of aqueous host-guest complexes consisting of a single molecule of stilbene derivative trapped within the hydrophobic interior of an OA dimer.[42,162]. The transient absorption (TA) and quantum yield (QY) measurements use 1 mM solutions of a compound dissolved in cyclohexane, or 0.5 mM solutions of the encapsulated compound in water.

Broadband TA measurements use the modified output of a 1 kHz regeneratively amplified Ti:sapphire laser (Legend Elite, Coherent). An optical parametric amplifier with two stages of nonlinear frequency conversion (TOPAS) produces 300 nm pump pulses that are attenuated to $\sim$120 nJ and focused to a diameter of $\sim$200 μm at the sample, where they intersect the time-delayed probe pulses at a small angle. A zero-order $\lambda/2$ wave plate rotates the polarization of the pump light for parallel, perpendicular, or magic angle measurements, and a synchronized chopper blocks every other pump pulse for active background subtraction. We generate broadband probe

pulses in the range 360-980 nm by focusing the 1280 nm signal from a second, home-built optical parametric amplifier into a circularly translating CaF_2 crystal. A pair of reflective parabolic mirrors collimates, then focuses the probe beam to a diameter of $\sim$100 μm at the sample. After passing through the sample, a transmission grating disperses the probe light onto a 256-element photodiode array for shot-to-shot detection. A suitable colored glass filter ensures that we do not observe signal from the second order reflection of the grating. We typically average 10^3 laser pulses per time delay for three consecutive scans. In most cases, we continuously translate the sample in order to avoid accumulation of photoproduct in the focal volume of the laser. We also eliminate contributions from the photoproduct by minimizing the number of time steps and by mixing the solution between scans. Measuring the TA spectrum at a fixed pump-probe time delay for a period of several minutes confirms that the signal remains essentially unchanged over the duration of a scan.

We measure the quantum yields for *trans* $\rightarrow$ *cis* photoisomerization ($\Phi_{t\rightarrow c}$) from the *in situ* conversion of a static sample under continuous irradiation with 300 nm laser pulses.[1] The isomerization yield is equal to the ratio of the photo-conversion rate relative to the excitation rate, as measured by transmission of the laser pulses through the sample. Only the *trans* isomer has significant absorption at 300 nm, therefore the decrease in transmission at this wavelength is proportional to the number of molecules converted to the *cis* isomer as a function of time. A 50% beam splitter separates the attenuated laser light into signal and reference beams before the former passes through the sample with a diameter of 1.5 mm and an incident energy of 2.5 nJ/pulse. Measuring shot-to-shot energies of the signal and reference pulses at 1 kHz accounts for small fluctuations of the laser intensity, and we typically average over 100 pulse pairs to obtain the transmission through the sample as a function of time. We calculate $\Phi_{t\rightarrow c}$ from the initial rate of change of the normalized transmission at 300 nm over the first $\sim$10 seconds of irradiation, which typically gives about 1-2% conversion in the static sample.

We measure fluorescence quantum yields (Φ_{fl}) based on the relative fluorescence intensity of each sample under continuous irradiation at 300 nm in a fluorimeter (Edinburg FS920CDT).

The reference solution consists of unsubstituted *trans*-stilbene in cyclohexane, which has a known quantum yield of $\Phi_{fl}^{ref} = 0.036$.[51] We determine the QYs for the other samples using the ratio of the integrated fluorescence intensities, I_i,

$$\Phi_{fl} = \Phi_{fl}^{ref} \times \frac{I_{samp}}{I_{ref}} \times \frac{A_{ref}}{A_{samp}} \times \left(\frac{n_{samp}}{n_{ref}}\right)^2 \tag{4.1}$$

where A_i and n_i are the absorbance and index of refraction, respectively, for the sample and reference solutions at the excitation wavelength.

Molecular dynamics (MD) simulations give the ground-state structures and relative energies for the *trans* and *cis* isomers of each compound inside the OA_2 capsule. The simulations begin with the structure of OA from a previous computational study,[163] and the optimized geometry of each stilbene from B3LYP/6-31G* calculations using the Gaussian09 software package.[164–166] We calculate restrained electrostatic potential (RESP) charges and create topology files using the Antechamber tool in the Amber software package.[167] We prepared initial structures of host-guest complexes using the rigid docking procedure as implemented in the AutoDock Vina 1.5.6 software.[168] The grid covers OA, with a spacing of 1.00 Å , which is a standard value for AutoDock Vina. The MD simulations of guest@OA_2 were performed using the GROMACS 4.5.6 program[169] with the AMBER03 force field.[170] We use the SETTLE algorithm[171] to constrain the bond lengths and angles of water molecules, and the LINCS algorithm[172] to constrain the bond lengths of OA. Long-range electrostatic interactions are calculated with the particle-mesh Ewald (PME) method.[173] Starting structures obtained from the docking procedure are placed in a cubic box with dimensions of $60 \times 60 \times 60$ Å, which is then filled with TIP3P water molecules.[174] We replace 16 water molecules with Na^+ ions to neutralize the charges of OA_2, then run the MD simulation with energy minimization for 3000 steps to obtain an equilibrated structure for the production run. The final MD simulations run for 100 ns with 2 fs time steps and the number of particles, pressure, and temperature all held constant (NPT ensemble). We obtain representative structures from cluster analysis. Yasara,[175] Chimera,[176] and VMD[177] programs were used for visualization

and for the preparation of the structural diagrams. The host-guest binding energies were calculated using the molecular mechanics/Poisson-Boltzmann surface area (MM/PBSA) method.[178]

4.3 Results and Analysis

4.3.1 Ground-State Structure and Spectroscopy

The upper panel of Figure 4.2 shows the ground-state absorption spectra of compounds **1**-**7** in cyclohexane. The spectra are very similar for most of the compounds, except that the lowest-energy $\pi\pi^*$ absorption band shifts to slightly longer wavelength with increasing alkyl chain length and number of substituents. A notable outlier in the series is 2,2'-dimethylstilbene (**5**), which has broader absorption bands and no discernible vibronic progression compared with the other compounds.[51] The lack of vibronic structure for compound **5** reflects the nonplanar equilibrium geometry of this molecule due to steric crowding of the *ortho*-substituted methyl groups, which rotates the phenyl rings and disrupts conjugation along the backbone of the molecule.[54] Spectra for the other compounds all have essentially the same vibronic progression as unsubstituted *trans*-stilbene, which is planar in solution.[179–182]

The lower panel of the figure shows the absorption spectra for the same series of compounds encapsulated in OA_2. For comparison, the lower panel also includes spectra for unsubstituted stilbene in cyclohexane, as well as encapsulated adamantane, which is transparent in this wavelength range. The spectrum of adamantane@OA_2 shows that the capsule has a strong absorption band near 280 nm, but does not absorb above $\sim$300 nm. Despite the partially overlapping absorption band of OA_2, we observe a slight bathochromic shift of the lowest-energy absorption band for all seven compounds upon encapsulation. The shift is consistent with a slightly more polarizable environment inside the capsule compared with cyclohexane.[183]

Encapsulation has a significant effect on the vibronic progression of the stilbene absorption bands, depending on the identity and number of substituents. Although unsubstituted stilbene (**1**) retains essentially the same vibronic structure above 300 nm as in solution, the progression be-

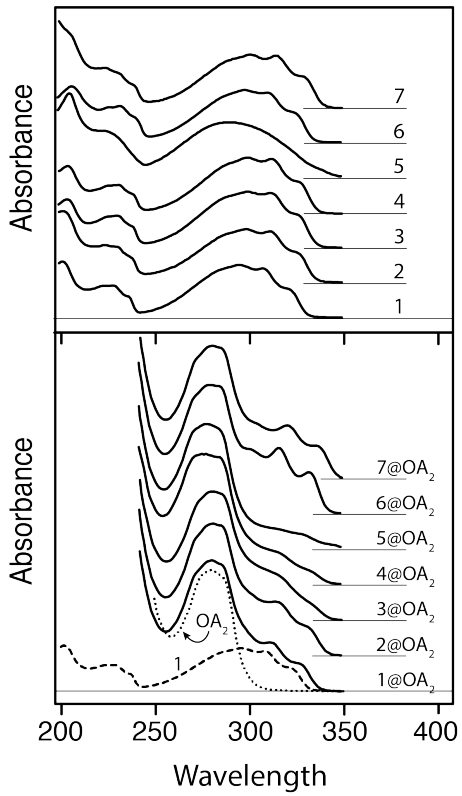

Figure 4.2: Ground-state absorption spectra of compounds **1**-**7** in cyclohexane (top panel) and encapsulated in OA_2 (lower panel). For comparison, the lower panel also includes the spectrum of **1** in cyclohexane (dashed line) and adamantane@OA_2 (dotted line).

comes less pronounced with increasing alkyl chain length for the mono-substituted compounds **2**-**4**. In contrast, the *meta*- and *para*-dimethyl-substituted compounds (**6** and **7**) have more pronounced vibronic structure in the capsule compared with solution. Similar to the structureless absorption band for compound **5** in solution, the relative degree of vibronic structure for the encapsulated compounds reflects differences in the relative geometries of each molecule inside the OA_2 capsule, as indicated by the MD simulations. Figure 4.3 shows representative structures from the simulations for both *trans* and *cis* isomers of **1**@OA_2. To see all representative structures see figure 4.12 in the appendix. Figure 4.4 show the dihedral angles for the central ethylene and each of the phenyl rings. Unlike solution, the simulations suggest that even the *trans* isomers are slightly nonplanar in the capsule.

The MD simulations also give the relative stabilities of the complexes. The binding energies for all seven compounds are listed in Table 4.1. The relative energies from the calculations show that

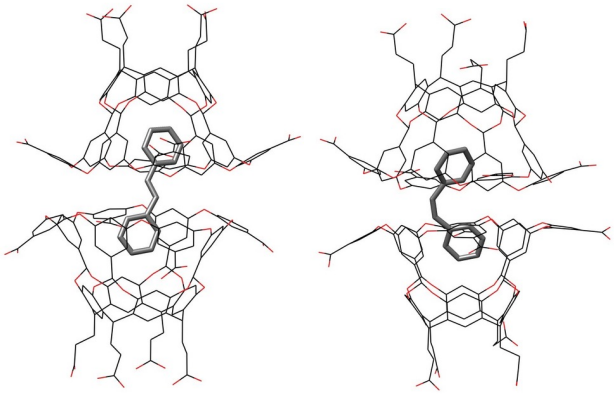

Figure 4.3: Simulated ground-state structures for the *trans* and *cis* isomers of encapsulated stilbene, **1**@OA_2.

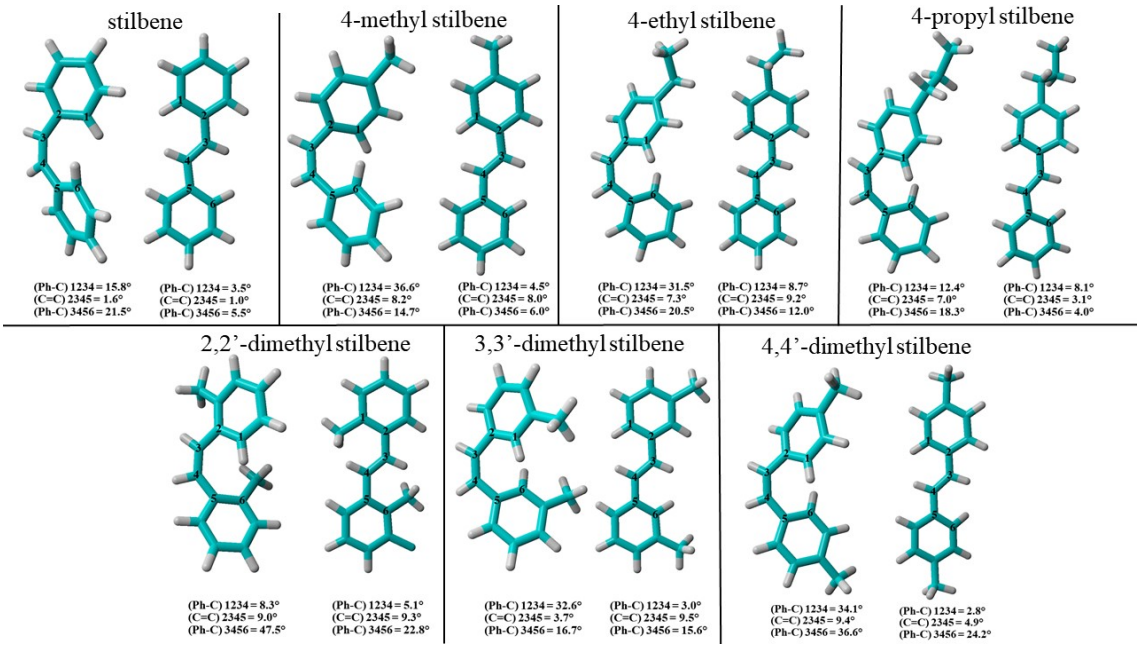

Figure 4.4: Geometries of encapsulated molecules from MD simulations.

the more stable complex (*trans* or *cis*) depends on the identity and location of the alkyl substituents. For example, the encapsulated *trans* isomer is more stable than the encapsulated *cis* isomer by 7.9 kJ/mol for **1**@OA_2, but the *cis* isomer becomes relatively more stable as the length of the alkyl chain increases for the mono-substituted compounds (**1**-**4**). The *cis* isomer becomes the more stable structure inside the capsule for the ethyl- and propyl-substituted compounds (by 10.1 and 63.7 kJ/mol, respectively), which is in sharp contrast with solution, where the *trans* isomers are more stable for all of the compounds in this study. For the series of dimethyl-stilbenes, only

the meta-substituted compound (**6**) favors the *cis* structure in the capsule. The simulations are consistent with previous experimental observations of the preferential encapsulation of one isomer over the other for each of these compounds.[43]

4.3.2 Transient Absorption Spectroscopy

Transient absorption (TA) measurements probe the excited-state dynamics of compounds **1**-**7** following $\pi\pi^*$ excitation at 300 nm. Figure 4.5 shows the evolution of the TA spectra for five of the compounds in cyclohexane (left side) and in the aqueous OA_2 capsules (right side). Spectra for the other two compounds were measured with a slight different range of probe wavelengths, and are shown in figure 4.6. All of the compounds have a strong excited-state absorption (ESA) band centered near 580-600 nm and weak stimulated emission (SE) below $\sim$420 nm.[184] The most notable difference among the spectra in solution is the relative intensity of a weak shoulder near 540-560 nm that depends on the location and number of alkyl substituents. In the capsules, the ESA bands become significantly broader, the shoulder becomes indistinguishable, and a second absorption feature around 420-460 nm becomes more pronounced. Importantly, we do not observe any transient signal following 300 nm irradiation of aqueous OA in the absence of stilbene.

The TA signals decay to the baseline within a few hundred picoseconds for all of the com-

Table 4.1: Calculated ground-state energies for *trans* and *cis* isomers of encapsulated stilbene derivatives.

Compound	E_{trans} (kJ/mol)	E_{cis} (kJ/mol)	ΔE (kJ/mol)	Expt.[a]
stilbene (**1**@OA_2)	-178.2	-170.3	+7.9	-
4-methyl stilbene (**2**)	-190.7	-189.7	+0.1	50/50
4-ethyl stilbene (**3**)	-198.7	-208.8	-10.1	cis
4-propyl stilbene (**4**)	-148.3	-212.0	-63.7	cis
2,2'-dimethyl stilbene (**5**)	-199.1	-173.2	+25.9	70/30
3,3'-dimethyl stilbene (**6**)	-190.1	-207.1	-17.0	cis
4,4'-dimethyl stilbene (**7**)	-215.4	-196.3	+19.1	trans

[a] Experimentally observed preferential solvation (*trans*/*cis*) using NMR spectroscopy, from Ref. 43.

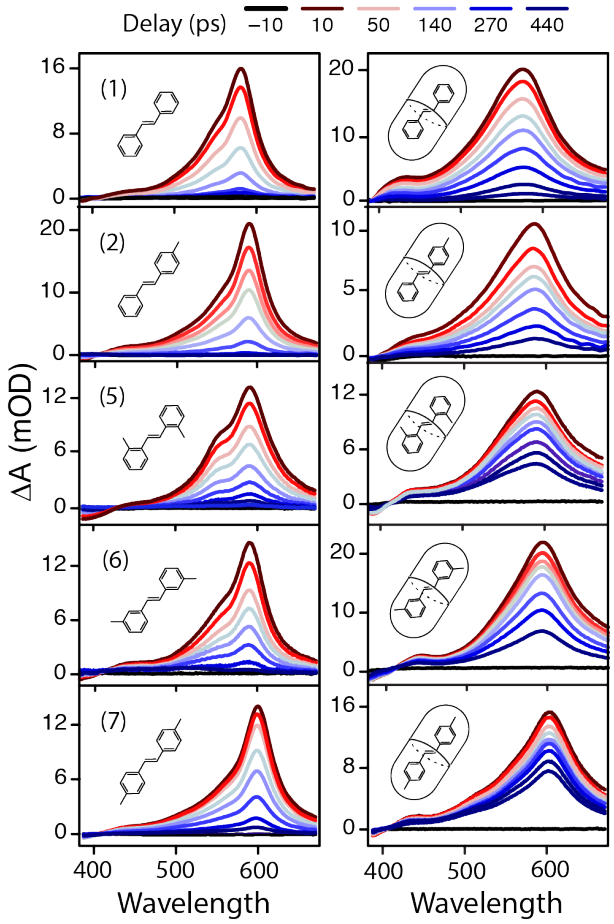

Figure 4.5: Evolution of the transient absorption spectra following 300 nm excitation of five stilbene derivatives in cyclohexane (left) and encapsulated in aqueous OA_2 capsules (right).

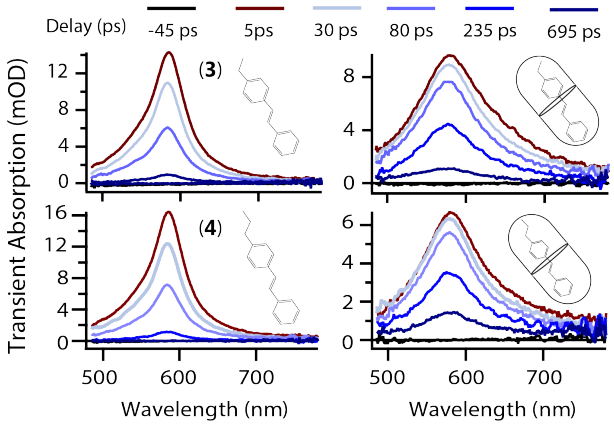

Figure 4.6: Evolution of the transient absorption spectra following 300 nm excitation of ethyl and propyl stilbene in cyclohexane (left) and encapsulated in aqueous OA_2 capsules (right).

pounds in solution, but the signals for the encapsulated molecules relax on a longer timescale that exceeds the 440 ps time window of our measurement. The normalized decay of the ESA bands for

three representative compounds is shown in Figure 4.7. In addition to the decay of the signal, we also observe a slight narrowing of the ESA bands within the first few ps following excitation. This spectral evolution is a well-known signature of structural relaxation and vibrational cooling in the S_1 excited state.[184–186] The spectral change is more subtle for molecules inside the OA_2 capsule, where the relaxed excited-state absorption band remains broader than in solution (Figure 4.8).

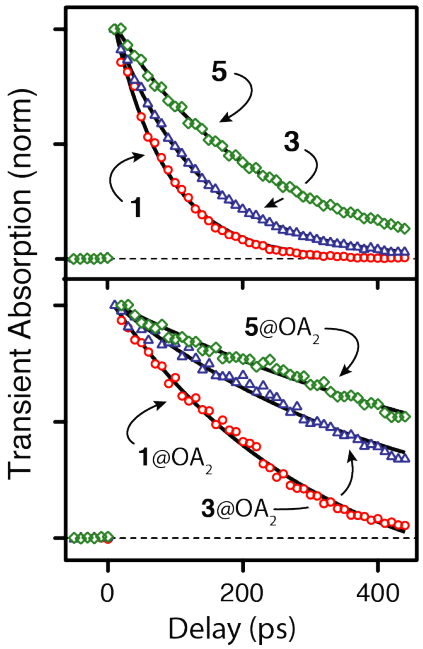

Figure 4.7: Normalized decay of the excited-state absorption bands for three representative compounds in solution (top panel) and in the OA_2 capsule. Lines are single exponential fits to the data.

Global fits to the data using a bi-exponential function reveal the timescales for vibrational cooling (τ_{vib}) and excited-state decay (τ_{decay}) for all seven compounds (see Table 4.2). The relatively large uncertainties in τ_{vib} are a result of the smaller amplitude of this component and a slight wavelength dependence of the time constant, which is a typical signature for vibrational cooling.[187] Compared with solution, the vibrational cooling times are about the same, or slightly longer, in the capsule.

The excited-state lifetimes, τ_{decay}, are sensitive to both the number and position of alkyl substituents, with lifetimes in solution ranging from 72 ps for unsubstituted stilbene (**1**) to 218 ps for 4,4'-dimethylstilbene (**7**). In general, the dimethyl substituted compounds have longer lifetimes

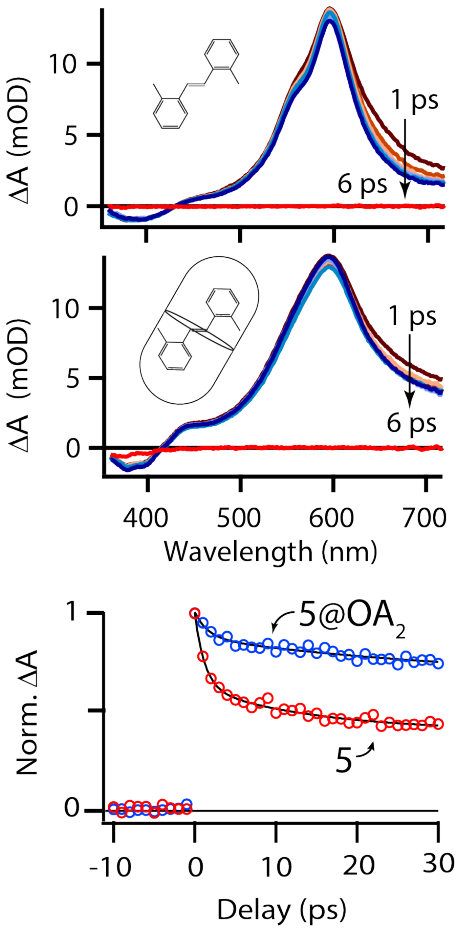

Figure 4.8: Narrowing of the excited-state absorption band of compound **5** in solution and in OA_2 over the range 1-6 ps. Bottom panel shows the decay of the normalized transient absorption signal at 710 nm, with black lines showing bi-exponential fits to the data.

than the mono- and un-substituted stilbenes. The lifetimes are consistently longer inside of the OA_2 capsules compared with cyclohexane solution, increasing by a factor of about 3-3.5 regardless of the location or number of alkyl substituents. The only exception is 4-propyl stilbene (**4**), for which the lifetime increases by $\sim$4.5 times.

Figures 4.5, 4.6, 4.7 and 4.8 show the TA signal with the relative pump-probe polarization at magic angle in order to eliminate contributions from rotational reorientation. We also measure the TA spectra for parallel and perpendicular polarization in order to calculate the time-dependent anisotropy of the ESA signal.[188] The anisotropy decays to zero as the distribution of excited molecules becomes isotropic, giving the reorientation time for molecules in the S_1 excited state, τ_{rot}. Figure 4.9 compares the anisotropy decay for representative compounds **1**, **5**, and **7** in solution

and in the OA_2 capsules.

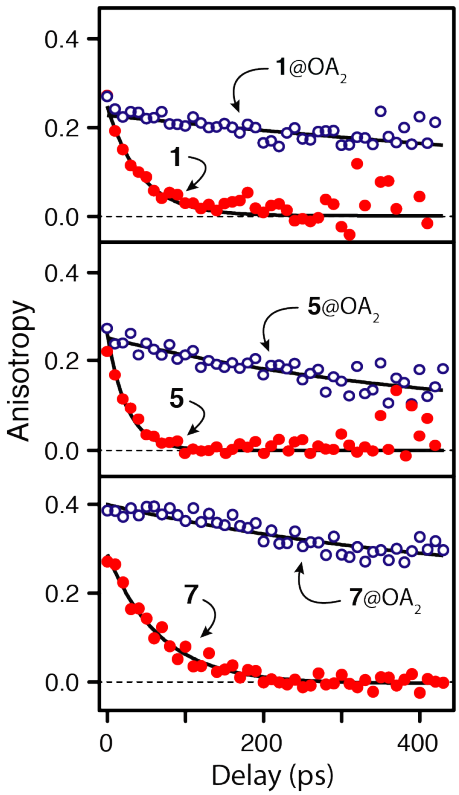

Figure 4.9: Anisotropy decay for compounds **1**, **5**, and **7** in cyclohexane (closed red markers) and in OA_2 (open blue markers). Black lines are single exponential fits to the data.

The initial value of the anisotropy is ∼0.3 for all of the samples except **7**@OA_2, which has an

Table 4.2: Excited-state lifetimes and reorientation times (in ps).[a]

Compound	cyclohexane			capsule		ratio
	τ_{vib}	τ_{decay}	τ_{rot}	τ_{vib}	τ_{decay}	$\tau_{decay}^{OA_2}/\tau_{decay}^{soln}$
stilbene (**1**)	1.5 (1.0)	72 (1)	48 (7)	4.6 (2.0)	260 (7)	3.6 (1)
4-methyl stilbene (**2**)	1.4 (0.5)	89 (1)	62 (7)	2.0 (0.8)	300 (12)	3.4 (1)
4-ethyl stilbene (**3**)	1.9 (1.0)	84 (1)	56 (2)	1.4 (1.0)	289 (1)	3.4 (1)
4-propyl stilbene (**4**)	1.3 (0.3)	86 (3)	85 (3)	6.0 (2.5)	384 (4)	4.5 (2)
2,2'-dimethyl stilbene (**5**)	3.2 (1.1)	124 (1)	41 (5)	2.9 (1.0)	430 (9)	3.5 (1)
3,3'-dimethyl stilbene (**6**)	1.8 (0.5)	119 (1)	46 (5)	4.5 (1.1)	358 (4)	3.0 (1)
4,4'-dimethyl stilbene (**7**)	2.0 (1.2)	218 (2)	61 (6)	1.6 (1.0)	670 (15)	3.1 (1)

[a] Values in parentheses are estimated 95% uncertainties.

initial anisotropy close to the maximum value of 0.4. In solution, the anisotropy decays to the baseline within about 100-200 ps, depending on the size and structure of the molecule. The relatively compact 2,2'-dimethylstilbene (**5**) has the shortest reorientation time of 41 ps, and the most extended molecule, 4-propylstilbene (**4**), has the longest reorientation time of 85 ps in cyclohexane. The reorientation times for all of the compounds in cyclohexane are listed in Table 4.2.

The anisotropy decay is much slower for the encapsulated compounds, with none of the samples becoming fully isotropic within the 440 ps time window of our measurement. The substantially slower anisotropy decays confirm that the molecules are encapsulated in OA_2, and also indicate that none of the stilbene derivatives are able to freely rotate inside of the capsule on the time scale of the excited-state lifetime. Instead, the partial decay of the anisotropy over 400 ps is consistent with the reorientation of the entire capsule containing the excited molecule. Consistent with this interpretation, a simple rotational diffusion model predicts a reorientation time of $\sim$1 ns for a particle with the outer dimensions of OA_2 (roughly 27 Å tall and 11 Å wide) in a fluid with the viscosity of water.

4.3.3 Quantum Yields

The TA measurements reveal the excited-state lifetimes, but we cannot determine the relative branching between *trans* and *cis* relaxation channels from that measurement, because both isomers are transparent in this range of probe wavelengths. Instead, we measure the isomerization and fluorescence quantum yields separately, as described in the methods section. Table 4.3 shows the values of $\Phi_{t\rightarrow c}$ and Φ_{fl} for all seven compounds in solution and in the OA_2 capsules. The fluorescence quantum yields loosely track the excited-state lifetimes both in solution and in the capsule, but the variation of the isomerization yields upon encapsulation is more sensitive to the location and identity of the alkyl substituents. Although the absolute uncertainties that we report for $\Phi_{t\rightarrow c}$ are fairly large, the *relative* values are more precise, because they come from back-to-back measurements to ensure identical experimental conditions across the entire series of compounds and in the two environments.

In solution, the isomerization yields vary from 0.39 to 0.57, and the fluorescence yields are in the range 0.03-0.05. Upon encapsulation, the isomerization yields decrease significantly for all of the compounds, but the already small fluorescence yields increase only by a factor of 1-2. For example, the isomerization yield for unsubstituted stilbene decreases from 0.51±0.05 in solution to only 0.12±0.07 in the capsule, while the fluorescence yield increases from 0.04±0.01 to 0.08±0.01. Because the fluorescence yields remain relatively small even in the capsule, the small increase of Φ_{fl} is not enough to account for the more substantial decrease of $\Phi_{t\rightarrow c}$ for the encapsulated molecules.

Table 4.3: Photoisomerization and fluorescence quantum yields.[a]

	solution		capsule		ratio
	$\Phi_{t\rightarrow c}$	Φ_{fl}	$\Phi_{t\rightarrow c}$	Φ_{fl}	$\Phi_{t\rightarrow c}^{soln}/\Phi_{t\rightarrow c}^{OA_2}$
Stilbene (**1**)	0.51 (5)	0.036 (2)	0.12 (7)	0.081 (4)	4.2 (1)
4-Methyl Stilbene (**2**)	0.46 (6)	0.030 (2)	0.15 (6)	0.050 (3)	3.0 (1)
4-Ethyl Stilbene (**3**)	0.43 (6)	0.041 (3)	0.18 (6)	0.043 (3)	2.3 (1)
4-Propyl Stilbene (**4**)	0.41 (6)	0.050 (3)	0.24 (6)	0.058 (3)	1.7 (1)
2,2'-Dimethyl Stilbene (**5**)	0.57 (6)	0.053 (3)	0.29 (6)	0.087 (4)	1.9 (1)
3,3'-Dimethyl Stilbene (**6**)	0.55 (5)	0.047 (2)	0.28 (5)	0.090 (3)	1.9 (1)
4,4'-Dimethyl Stilbene (**7**)	0.39 (5)	0.049 (2)	0.06 (9)	0.142 (3)	6.5 (3)

[a] Estimated uncertainties in parentheses. Uncertainties for $\Phi_{t\rightarrow c}$ refer to the absolute value of the quantum yield. Relative uncertainties are much lower because values are from back-to-back measurements under identical conditions, as reflected in the smaller uncertainties for the ratios of quantum yields.

In order to highlight the relative impact of confinement on the isomerization yield, Table 4.3 also shows the ratio of the quantum yields in solution and in the capsule, $\Phi_{t\rightarrow c}^{soln}/\Phi_{t\rightarrow c}^{OA_2}$, for each compound. The isomerization yields decrease upon encapsulation for all seven compounds, but the decrease of $\Phi_{t\rightarrow c}$ is not as uniform across the series as the 3-4 fold increase of τ_{decay} or the 1-2 fold increase of Φ_{fl}. For example, confinement decreases the isomerization quantum yield by less than a factor of two for compounds **4-6**, compared with a 4-fold decrease for unsubstituted stilbene, and a decrease of more than 6-fold for compound **7**. We illustrate this point in Figure 4.10 by comparing the variation of the excited-state lifetimes (top panel) and quantum yields (bottom panel) for all seven compounds in solution and in OA_2. The trend of increasing lifetime with alkyl

substitution pattern and the consistent (3-4 fold) increase of the excited-state lifetimes for all of the encapsulated compounds are evident in the top panel of the figure. In contrast, the bottom panel shows that the relative quantum yields in solution and in the capsule are more sensitive to the position and number of alkyl substituents.

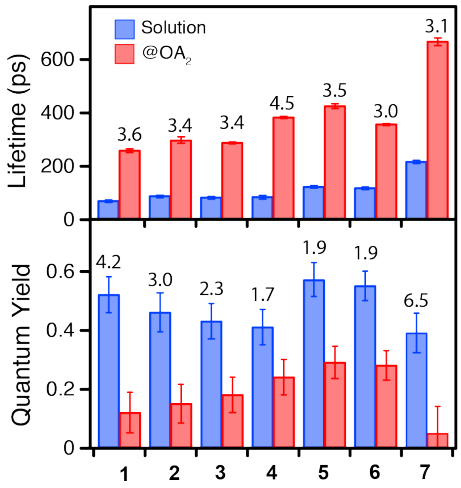

Figure 4.10: Excited-state lifetimes and quantum yields for compounds **1-7** in solution (blue bars) and encapsulated in OA_2 (red bars). Numbers above the bars give the ratio of the signal in the two environments for each compound.

Notably, the isomerization quantum yields for the series of mono-substituted compounds **1-4** show different trends in solution and in the capsules. The quantum yield decreases slightly with increasing substituent chain length in solution, but the opposite trend is observed in the capsules, where increasing the length of the mono-substituted alkyl chains gives a larger *trans* $\rightarrow$ *cis* quantum yield. As mentioned above, the quantum yields for *ortho*- and *meta*-substituted dimethylstilbene (compounds **5** and **6**) decrease only by half, but the quantum yield of the *para*-substituted compound (**7**) drops significantly in the capsule, even though the excited-state lifetimes of all three dimethyl-substituted compounds increase by roughly the same extent.

4.4 Discussion

Excited-state lifetimes and quantum yields reveal key information about photoisomerization mechanisms. In cyclohexane, the lifetimes vary across the series of stilbene derivatives due to electronic

effects from the alkyl substituents. Compared with unsubstituted stilbene, the slight increase of the lifetimes for compounds **2**-**4**, and the even larger increase for compound **7**, suggests that substitution at the *para* position may stabilize the planar structure with respect to torsional rotation in the excited state. Although solvent viscosity also inhibits the barrier crossing by restricting the rotation of the phenyl rings, **7** was shown to have a larger 'intrinsic' barrier than **1**, independent of the solvent contribution in non-polar solvents.[51] The mono-substituted compounds should be even less sensitive to solvent viscosity effects, because isomerization of **1**-**4** only requires rotation of the (smaller) unsubstituted phenyl ring, which sweeps out the same solvent volume for all four molecules. This is consistent with the similar lifetimes for **2**-**4**, even though the reorientation time for the entire molecule (τ_{rot}) increases with chain length.

The excited-state lifetimes increase by a factor of ∼3-4 for all of the compounds in the OA_2 capsule. Although encapsulation does not prevent isomerization of the stilbene derivatives,[42] our anisotropy measurement shows that there is not sufficient free space in the capsule to allow any of the molecules to fully reorient on the timescale of the excited-state lifetime. Accordingly, confinement increases the excited-state lifetime by restricting the torsional rotation of the phenyl rings, which inhibits the molecule from crossing the barrier to access the CoIn with the ground state. Notably, the compound with the largest relative increase in lifetime, **4**@OA_2, also has the longest chain length and experiences the most crowding inside the capsule. The MD simulations show significant destabilization of the binding energy for the encapsulated *trans* isomer of **4**@OA_2 compared with the other compounds. We conclude that crowding in the capsule inhibits rotation around the C=C bond (*i.e.* the barrier crossing in the S_1 excited-state) more for this compound than any of the others. The confined environment may inhibit other motions that are important for the isomerization reaction as well, such as phenyl twisting or pyramidalization.[52,189] Polarization effects are unlikely to play a major role, because the interior of the OA_2 capsule is similar to benzene and provides a similar environment for all of the encapsulated compounds.[183]

Substantial broadening of the ESA bands in the capsule points to a significant influence of the confined environment on the excited-state geometry. The broadening and lack of vibronic structure

in the excited-state spectra are consistent with distorted, non-planar structures for electronically excited molecules.[188] The spectrum of compound **5** in cyclohexane provides some clues about the relationship between the absorption spectra and molecular structure. The ground-state spectrum of **5** is very different from the others due to rotation of the phenyl rings by the *ortho*-substituted methyl groups, giving a spectrum that more closely resembles the non-planar *cis* isomer.[51] However, the $\pi\pi^*$ character of the the excited state favors a more planar structure by increasing the C-C bond order between the ethylenic bridge and the phenyl rings.[190] Thus, the ESA spectrum of **5** more closely resembles the other compounds in solution, but retains a fairly strong shoulder near 540 nm that is probably related to distortions caused by the methyl groups. The less prominent shoulder and narrower ESA bands for **2** and **7** are consistent with those molecules having a more stabilized planar geometry compared with **1**, as noted above. In contrast, all of the ESA bands are broadened and distorted to a similar degree inside the capsule, including **5**@OA_2. The substantial broadening of the ESA bands points to significant distortion of the excited-state structure for all of the encapsulated compounds. The broadening could be a signature of either a single distorted geometry,[5] or a distribution of geometries in the capsule.

Perhaps the most striking effect of confinement is the influence on the isomerization quantum yield. While the excited-state lifetime depends on the torsional rotation barrier, the quantum yield depends on the non-adiabatic dynamics through the CoIn. Specifically, the topology of the CoIn determines the branching between *trans* and *cis* isomers when the molecule returns to the ground state.[53] All seven of the stilbene derivatives have a lower $\Phi_{t\rightarrow c}$ inside the capsule, suggesting a distortion of the CoIn that favors relaxation back to the *trans* structure. The relative impact depends on the structure of the molecule, consistent with different distortions of the CoIn depending on the steric interactions of a molecule with the capsule.

We observe the largest decrease of the isomerization quantum yield for **7**@OA_2. The preference for the *trans* isomer upon returning to the ground state is not surprising for **7**@OA_2, considering the *trans* isomer of this molecule has the most stable binding energy out of the entire series of guest@OA_2 complexes. The deep stabilization of the *trans* isomer reflects a favorable packing

of the methyl groups in the narrow ends of the OA_2 capsule,[163] and is likely to persist in the excited state. Stabilization of the *trans* structure in the excited state not only increases the barrier for torsional rotation, but apparently also impacts the CoIn with the ground state.

Another important observation is the changing influence of encapsulation on the QY with increasing chain length for the mono-substituted compounds. The ratio $\Phi_{t\rightarrow c}^{soln}/\Phi_{t\rightarrow c}^{OA_2}$ decreases from 4.2 to 1.7 across the series **1**-**4**. We interpret this trend as a result of increased crowding in the capsule, which increasingly favors the *cis* isomer at the CoIn. The MD simulations and experimental preferential solvation studies[43] show that the *cis* isomer becomes increasingly favored with increasing chain length, probably due to crowding effects for the extended *trans* isomers. As the *cis* isomer becomes more favorable, we see a similar shift in the ability to access that structure in the ground state. However, we point out that even when the *cis* isomer is the more stable ground-state structure in the complex, the quantum yield still favors the *trans* isomer (*i.e.*, $\Phi_{t\rightarrow c} < 0.5$) and is lower than in solution ($\Phi_{t\rightarrow c}^{OA_2} < \Phi_{t\rightarrow c}^{soln}$). This observation points to a restriction in getting from the *trans* structure to the *cis* structure in the capsule, which is alleviated, but not eliminated with increased crowding. We comment on the nature of this restriction in more detail below.

The QYs of compounds **5** and **6** are least sensitive to the effects of confinement, decreasing by slight less than a factor of 2. The *ortho*- and *meta*-substituted methyl groups of **5** and **6**, respectively, do not extend into the ends of the capsule, and therefore may be less sensitive to confinement. This picture is supported by the faster reorientation times for compounds **5** and **6** in the solution-phase anisotropy measurements, which indicates that the *ortho*- and *meta*-substituted compounds sweep out a smaller "volume" for reorientation compared with the more extended *para*-substituted molecules. In other words, the more oblate profile of **5** and **6** may be less sensitive to the interior shape of the capsule as these molecules move along the reaction path, leading to less variation in the relative stabilization of the different structures compared with the more extended *para*-substituted compounds.

The schematic energy-level diagram in Figure 4.11 illustrates the role of confinement in tuning the excited-state dynamics. The figure shows potential energy curves along the torsional isomer-

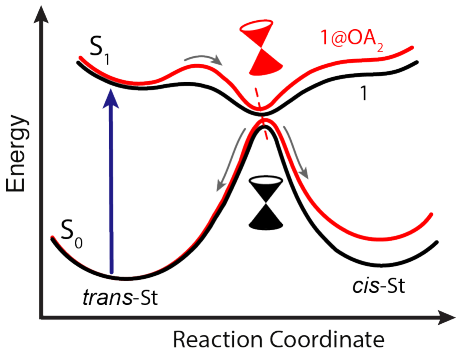

Figure 4.11: Schematic diagram of the potential energy surface along the reaction coordinate for stilbene in solution (black) and in the capsule (red). Encapsulation raises the barrier for isomerization in the excited state, and influences the conical intersection with the ground state. See text for details.

ization coordinate for the ground and excited states of a stilbene derivative. The black curves represent the potential energy in solution, and the red curves show how those potentials might be affected inside an OA_2 capsule. Specifically, longer excited-state lifetimes are a result of an increased torsional barrier in the capsule, which inhibits the molecule from accessing the CoIn at a perpendicular geometry, whereas the quantum yield is affected by changes in the topology of the CoIn. For example, destabilization of the *cis* structure in the capsule could tilt the CoIn in such a way that favors relaxation back to the *trans* ground state. The distortion could take the form of either a tilting of the CoIn to give a steeper slope of descent toward the *trans* isomer, as pictured, or simply a preference to pass through a region of the conical seam that is shifted toward the *trans* structure.[52,53,189,191] As we discuss below, destabilization of the *cis* structure in the region of the CoIn may be a transient effect, based on the starting structure of the complex.

Passage through the CoIn depends on trajectory, as well as the shape of the potential, and we would expect the path from the transition state to the CoIn to be influenced by the presence of a lower-lying phantom (p*) state.[53,189,192] It is interesting to consider whether there may be a stabilized structure similar to p* that is shifted toward the *trans* geometry, or even two separate p*-like minima on the *trans* and *cis* sides of the perpendicular geometry. In the case of 4-propylazobenzene, we showed in chapter 3 that excitation of the encapsulated *trans* isomer results in trapping of both *trans* and *cis* structures in the excited state.[5] Adiabatic isomerization in

the excited state of the azobenzene compound is made possible through an in-plane inversion coordinate that is not possible for stilbene, but nevertheless points to the ability of the capsule to stabilize new structures in the excited state that are not observed in solution. Such restrictions may be responsible for new reaction paths in confined molecules compared with their unrestricted counterparts.[22]

Finally, it is important to consider the specific role of the capsule in stabilizing or destabilizing the different structures along the reaction path, not only the ground and excited states of *trans* and *cis*, but also the transition state and p*. Specifically, stabilization is dynamic, because the MD simulations show a fairly significant displacement of the two halves of the capsule between the equilibrated structures of the *trans* and *cis* isomer complexes. While the capsule will eventually stabilize either of the equilibrium structures, the movement of the heavy capsule probably restricts the motion of the encapsulated molecule along the excited-state reaction coordinate. There is very little driving force in the excited state, where the potential is relatively flat along the torsional coordinate. The anisotropy measurements give a rough idea of the timescales involved for the relative movement of the molecule and the capsule, tens of ps for the stilbene derivatives (similar to the excited-state lifetimes) but $\sim$1 ns for the full capsule. In other words, the capsule may be largely frozen on the timescale of the photoisomerization reaction,[193] and is likely to impede torsional rotation in the excited-state. Similar to the red lines in Figure 4.11, the slow-moving capsule results in potential energy curves that favor the initial *trans* structure, even in cases when the encapsulated *cis* isomer is more stable overall. The result is both a higher barrier, as well as a distortion of the CoIn that lowers $\Phi_{t\rightarrow c}$ compared with solution for all of the molecules. Increased crowding that favors the *cis* isomer reduces, but does not fully overcome the distortion at the CoIn, because of the separation of timescales. Although beyond the scope of this work, simulations of the encapsulated molecules in the excited state would be informative.

4.5 Conclusion

Transient absorption and quantum yield measurements for a series of alkyl-substituted stilbene derivatives reveal new details about photoisomerization in confined environments. The excited-state lifetimes probe the barrier crossing on the S_1 surface, and the quantum yields provide direct insight on the non-adiabatic dynamics through the CoIn that returns the molecule to the ground state. A key result is that encapsulation inhibits *trans*→*cis* isomerization by restricting the rotation of the phenyl rings even in cases where the encapsulated *cis* isomer is more stable than *trans* in the relaxed ground state. This discrepancy between the photoisomerization dynamics and the steady-state equilibrium highlights the dynamic nature of the host-guest interaction, where the capsule favors the initial state of the molecule and is slow to respond on the timescale of the isomerization reaction.

4.6 Appendix

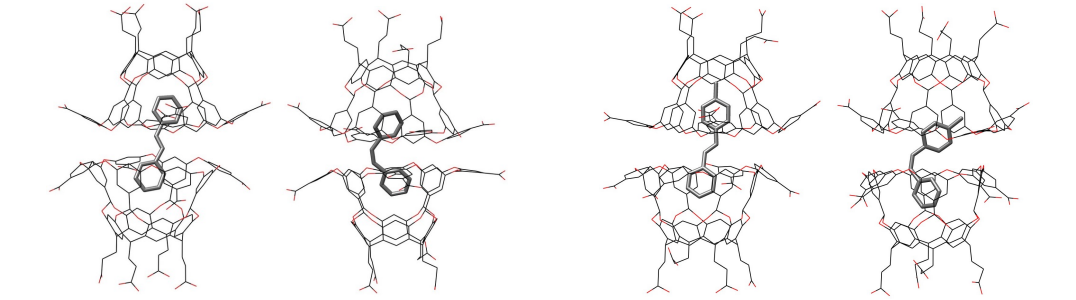

trans-**1**@OA_2 *cis*-**1**@OA_2 *trans*-**2**@OA_2 *cis*-**2**@OA_2

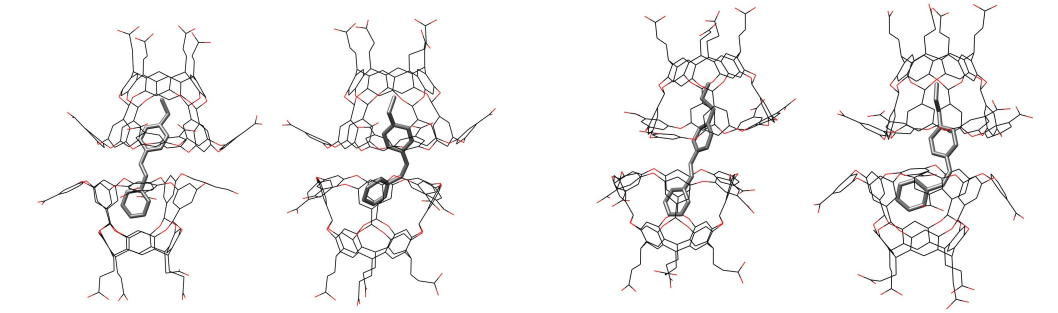

trans-**3**@OA_2 *cis*-**3**@OA_2 *trans*-**4**@OA_2 *cis*-**4**@OA_2

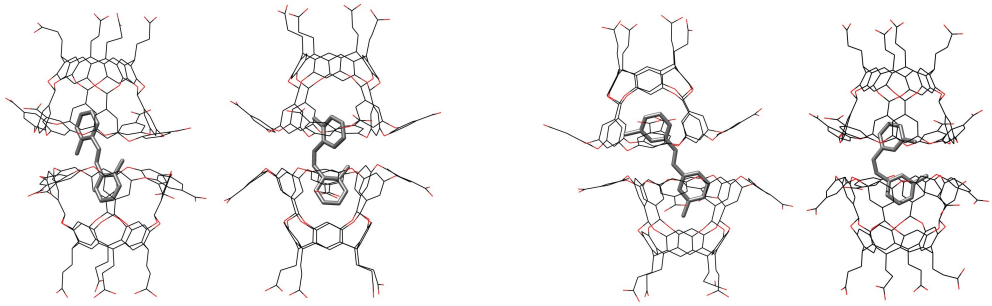

trans-**5**@OA_2 *cis*-**5**@OA_2 *trans*-**6**@OA_2 *cis*-**6**@OA_2

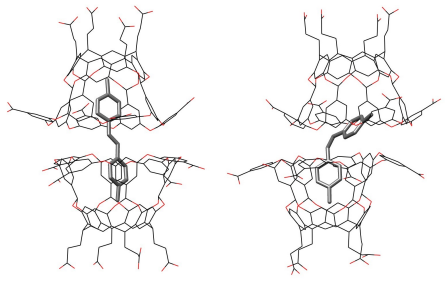

trans-**7**@OA_2 *cis*-**7**@OA_2

Figure 4.12: Structures of guest@OA_2 complexes from MD simulations.

Chapter 5

Ultrafast Dynamics of Encapsulated Azobenzenes Following $n\pi^*$ and $\pi\pi^*$ Excitation

5.1 Introduction

Photoisomerization reactions play a central role in light-sensitive biological functions such as vision and phototaxy,[17,153] as well as technological applications ranging from photochromism to molecular machines.[194–199] The environment plays an important role in facilitating the isomerization reaction for many of these light-activated processes, which often take place within the spatially confined active site of a protein, inside a nanoporous material, or in a solid-state matrix.[16,18,20,31,151] In each of these confined environments, steric effects influence the reaction rates, yields, and products that form by directing the motions of the atoms and stabilizing or destabilizing specific structures along the reaction path. Azobenzenes are prototypical photochromic compounds with interesting dynamics due to the competing rotation and inversion mechanisms for isomerization around the central N=N bond.[59–65,200–204] Given the different geometric requirements of the two reaction channels, azobenzenes are particularly susceptible to the effects of confinement.

This chapter examines the photoisomerization dynamics of *trans*-azobenzene (*t*-Az) and several 4-alkyl- and 4,4'-dialkyl-substituted *t*-Az derivatives encapsulated in a supramolecular host-guest complex using ultrafast spectroscopy. The host-guest complex offers a unique environment for probing the photoisomerization dynamics by restricting the internal rotation of the phenyl rings around the central N=N bond.[5,6] Each self-assembled complex consists of a single molecule of azobenzene encapsulated in the hydrophobic cavity formed by two water-soluble 'octa-acid' (OA)

host molecules.[40,41,205] The photochemistry of geometric isomerization and bimolecular reactions in the OA_2 cavity have been studied extensively, and we recently reported on the ultrafast photoisomerization dynamics of 4-propyl-substituted stilbene and azobenzene, as well as a series of alkyl-substituted stilbenes.[5,6] The interactions of the host-guest complex were shown to directly influence the relaxation and reaction channels of confined molecules by distorting the ground- and excited-state potential energy surfaces of the confined molecule. For example, confining alkyl-substituted stilbene molecules in the cavity of an OA_2 capsule restricts the internal rotation of the phenyl rings around the central C=C bridge, resulting in longer excited-state lifetimes and lower quantum yields for *trans*→*cis* isomerization.

There has been significant interest in understanding the excited-state isomerization for Az, including differences in the dynamics following excitation to the $n\pi*$ and $\pi\pi*$ excited states. Figure 5.1 shows the ground-state absorption spectrum of unsubstituted *t*-Az in cyclohexane and in the OA_2 capsule. The *t*-Az spectrum includes a weak $S_1(n\pi*)$ absorption band near 440 nm, and a stronger $S_2(\pi\pi*)$ band near 320 nm. The $S_2(\pi\pi*)$ band shifts to slightly longer wavelength in the OA_2 capsule, which has an overlapping absorption band at 280 nm, but does not absorb above $\sim$300 nm.[206] After exciting either absorption band of Az in solution the relaxation from the relaxed S_1 geometry requires the molecules to move along the inversion-assisted rotation coordinate before reaching the conical intersection and relaxing back to the ground-state. The inversion-assisted rotation mechanism is allowed through mixing of the nπ* and $\pi\pi$* states due the small energy gap between them.[207] The dynamics for the inversion-assisted rotation is first initiated from the planar molecular structure with movement along the inversion coordinate causing in-plane bending of the phenyl ring, this motion then transitions into out-of-plane rotation to complete the isomerization mechanism. In this chapter, we monitor the excited-state dynamics of unsubstituted Az in both environments following $n\pi*$ excitation at 470 nm and $\pi\pi*$ excitation at 320 nm.

In order to probe the role of confinement in more detail, we examine the dynamics for the series of alkyl-substituted azobenzenes in Figure 5.2. Alkyl substituents change the interaction with the capsule through increased crowding, but do not substantially affect the electronic structure of the

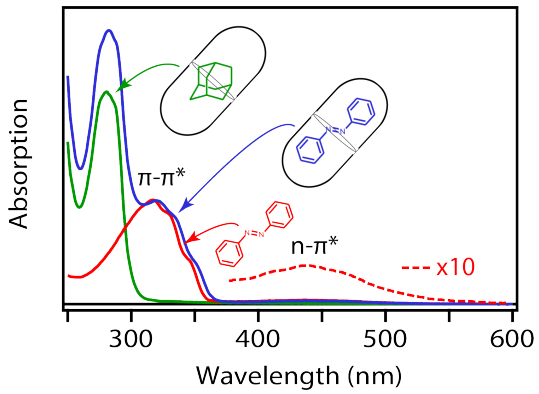

Figure 5.1: Ground-state absorption spectra of *t*-Az in cyclohexane (red), *t*-Az@OA_2 (blue), and adamantane@OA_2 (green). Adamantane is transparent in this wavelength range. The weak $n\pi*$ absorption band of *t*-Az is also shown on an expanded scale above 360 nm.

encapsulated molecules.[5] Changing the size of the encapsulated Az molecule with a series of increasing alkyl-chain lengths changes the size and structure of the molecule in the capsule, which impacts the stability of the *trans* and *cis* isomers and even the yields for the photoisomerization reaction.[6]

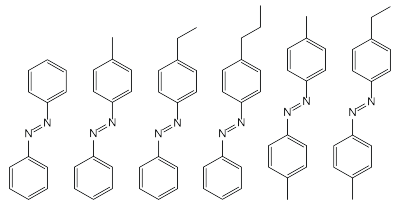

Figure 5.2: Structures of *trans*-azobenzenes (from left to right): azobenzene (Az), 4-methylazobenzene (MeAz), 4-ethylazobenzene (EtAz), 4-propylazobenzene (PrAz), 4,4'-dimethylazobenzene (Me_2Az), 4,4'-methylethylazobenzene (EtMeAz).

5.2 Experimental Details

trans-Azobenzene (*t*-Az) was purchased from Sigma-Aldrich and used as received. The octa acid (OA) and substituted *t*-Az derivatives were synthesized as previously reported.[42,43,161] We form self-assembled complexes (guest@OA_2) by sonicating 2 equivalents of aqueous OA with 1 equivalent of *t*-Az derivative until the solution is transparent.[41,208] Experiments for $n\pi*$ excitation use either an 8 mM solution of *t*-Az in cyclohexane or an 8 mM solution of encapsulated Az at pho-

tostationary state (PSS). We obtain PSS by continuously irradiating a sample of *t*-Az@OA_2 with a high-intensity 300 nm light-emitting diode to obtain a steady-state equilibrium between the two isomers in the capsule. Experiments for $\pi\pi^*$ excitation use either a 1 mM solution of the *t*-Az derivative in cyclohexane or a $\sim$0.5 mM solution of the encapsulated *t*-Az derivative. All measurements use a 1 mm quartz cuvette on a circularly translating stage to avoid accumulation of photoproduct in the laser focal volume.

The transient absorption (TA) measurements use the modified 800 nm output of a regeneratively amplified Ti:sapphire laser (Legend Elite, Coherent) operating at 1 kHz. A portion of the fundamental laser light is passed into an optical parametric amplifier (OPA) to generate pump pulses at 470 nm and 320 nm. The pump polarization is set to parallel or perpendicular orientation with respect to the probe using a zero-order $\lambda/2$ waveplate, and a pair of CaF_2 prisms compress the pump pulses to a duration $<$100 fs. The pump beam is attenuated to $<$1.2 μJ/pulse and focused to a diameter of $\sim$200 μm at the sample, where it overlaps the probe beam. The broadband probe pulses covering the range 340-990 nm come from white-light continuum generation in a circularly translating CaF_2 crystal using the 1200 nm signal from a second, home-built OPA. The probe beam is collimated and focused into the continuously translating sample using a pair of parabolic mirrors. After passing through the sample, a CaF_2 prism disperses the probe pulses onto a 256-element photodiode array for shot-to-shot detection. A synchronized chopper blocks every other pump pulse for active background subtraction, and we average 10^3 laser pulses per time delay for each spectrum. All TA spectra reported below are the calculated isotropic signals from separate measurements with parallel and perpendicular polarization of the pump and probe light in order to eliminate contributions from rotational reorientation.[188]

Separately, we measure the *trans*$\rightarrow$*cis* photoisomerization quantum yields ($\Phi_{t\rightarrow c}$) for $\pi\pi^*$ excitation by monitoring the change in transmission of 320 nm UV laser pulses through a sample as a function of time.[1,184] The increase in transmission of the UV laser pulses that we observe as a function of time is proportional to the number of molecules that isomerize from *trans* to *cis*, because only the *trans* isomers have appreciable absorption at 320 nm. We calculate the *trans* $\rightarrow$

cis quantum yield from the relative change in transmission as a function of time compared with the absolute transmission of the sample, accounting for small fluctuations of the laser intensity by simultaneously measuring the intensity of a reference beam. A 50% beam splitter separates the 320 nm laser light into signal and reference beams that are measured with identical integrating photodiodes operating at 1 kHz. The signal beam passes through the sample with a beam diameter of 1.5 mm and an incident energy of 2.5 nJ/pulse.

5.3 Results and Analysis

5.3.1 Transient Absorption Spectroscopy

5.3.1.1 Excitation to $S_1(n\pi^*)$ at 470 nm

The top panel of Figure 5.3 shows the evolution of the transient absorption (TA) spectrum following $n\pi^*$ excitation of unsubstituted *t*-Az in cyclohexane. The transient spectrum has a strong excited-state absorption (ESA) band centered near 395 nm and a weaker band near 540 nm. As reported previously, the stronger absorption band shifts and narrows due to vibrational relaxation within the first few hundred fs, and both bands decay simultaneously to the baseline within a few ps as the excited molecules return to the ground electronic state.[60,63] A weak absorption feature below 375 nm persists for up to ~20 ps due to broadening and red-shifting of the $\pi\pi*$ absorption band for the vibrationally excited *trans* isomer in the ground state.[209] Consistent with the low quantum yield for *trans*→*cis* isomerization of azobenzene, and weak ground-state absorption of both isomers in the visible, there is very little change in absorption at longer delay times due to the formation of *cis* or ground-state bleach of the *trans* isomer.

Unlike solution, the TA measurement for $n\pi*$ excitation of *t*-Az@OA_2 is complicated by a residual contribution from excitation of the encapsulated *cis* isomer. The thermal back reaction from *cis* to *trans* is much slower in the capsule compared with solution,[210] which leads to greater accumulation of the *cis* isomer over the duration of the experiment. The *cis* isomer also has a stronger absorption than the *trans* isomer at 470 nm, causing even a small population of *cis* to

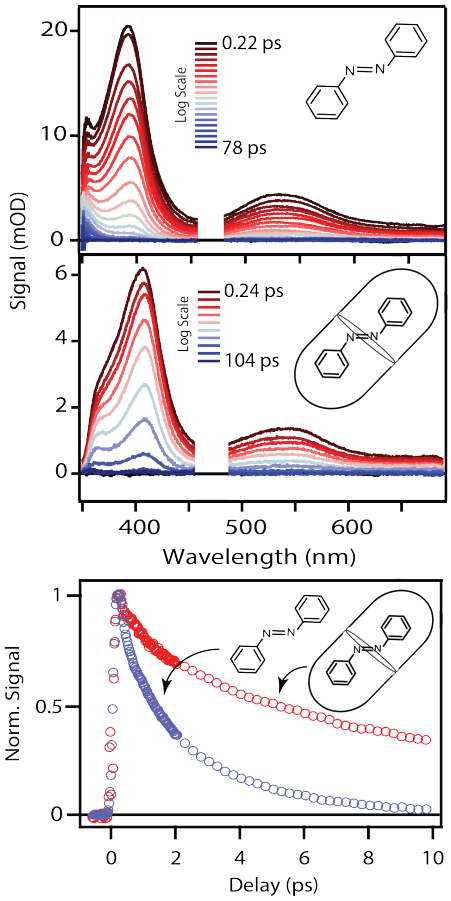

Figure 5.3: Evolution of the transient absorption spectra for Az in cyclohexane and in the OA_2 capsule following nπ* excitation at 470 nm. Bottom panel shows the decay of the normalized transient absorption signal near 400 nm.

contribute to the signal. In order to avoid variation in the relative concentrations of encapsulated *trans* and *cis* isomers, we measure the excited-state dynamics for a sample of Az@OA_2 at photo-stationary state (PSS). A benefit of the measurement at PSS is that we simultaneously probe the excited-state dynamics for both forward and reverse reactions of the encapsulated molecule.

The TA spectrum for the sample of encapsulated molecules at PSS (middle panel of Figure 5.3) includes contributions from both *t*-Az@OA_2 and *c*-Az@OA_2. Based on the static absorption spectrum of the sample at PSS in figure 5.4, we estimate that $\sim$23% of the ground-state molecules are in the *cis* isomer, which has a molar absorbance three times larger than the *trans* isomer at the excitation wavelength, and therefore gives an excited-state population that is $\sim$40% *cis* and $\sim$60% *trans*. Comparing the ground-state absorption spectrum of the sample before and after each TA

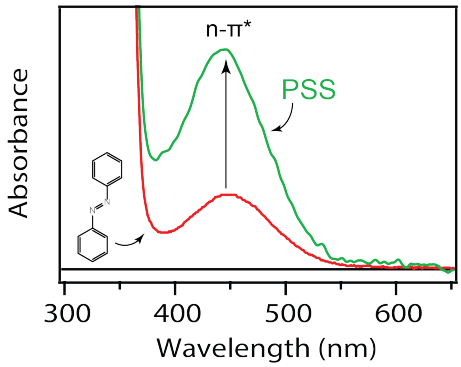

Figure 5.4: Ground-state absorption spectra of pure *t*-Az@OA_2 and a mixture of *t*-Az@OA_2 and *c*-Az@OA_2 at PSS.

measurement confirms that the relative concentration of isomers remains unchanged throughout the experiment.

Analysis of the TA data for the encapsulated molecules at PSS (see below) reveals a weak contribution from *c*-Az@OA_2, but the dominant contribution to the TA spectrum comes from *t*-Az@OA_2 and closely resembles the transient spectrum following $n\pi*$ excitation of pure *t*-Az in cyclohexane. The ESA band shifts to slightly longer wavelength in the capsule, similar to the shift of the ground-state spectrum, and decays on a slightly longer timescale, as illustrated in the bottom panel of Figure 5.3. The longer excited-state lifetime in the capsule prevents accumulation of vibrationally excited molecules in the ground state that was responsible for the positive absorption feature below ∼360 nm in cyclohexane. Additionally, the shift of the ground-state $\pi\pi*$ absorption band results in a transient ground-state bleach below ∼360 nm that we could not observe in cyclohexane for the same range of probe wavelengths.

5.3.1.2 Excitation to $S_2(\pi\pi^*)$ at 320 nm

Figure 5.5 compares the evolution of the TA spectra following $\pi\pi^*$ excitation of unsubstituted *t*-Az in solution and in the capsule. We separate the evolution of each spectrum into two panels to better represent the rapid relaxation from S_2 to S_1 within the first ∼200 fs, and the subsequent relaxation from S_1 to S_0 on the time scale of a few ps.[5] Unlike the $n\pi^*$ experiments above, we measure the dynamics following $\pi\pi^*$ excitation for samples of the pure *trans* isomer in both environments.

The measurement at PSS is unnecessary in the case of UV excitation, because the transient signal contains negligible contributions from direct excitation of the cis isomer. The *cis* isomer does not accumulate as readily in this sample,[211] and also the absorption of the *trans* isomer is substantially larger than the *cis* isomer at 320 nm. Comparing the static absorption spectra before and after each TA measurement confirms that there is minimal conversion to the *cis* isomer during the experiment.

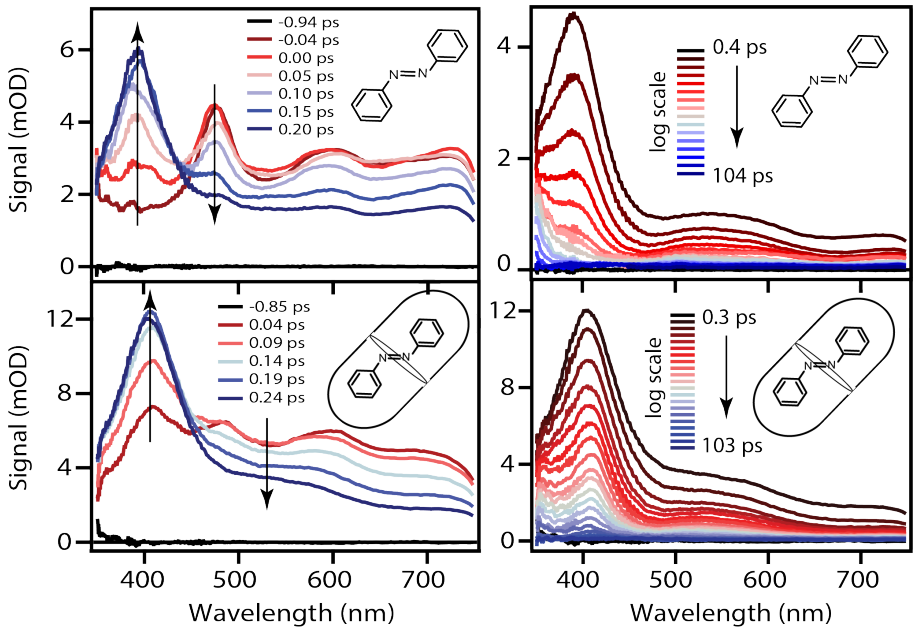

Figure 5.5: Evolution of the transient absorption spectra after $\pi\pi^*$ excitation for *t*-Az in cyclohexane (top panels) and in the OA_2 capsule (bottom panels). The left side shows first few hundred fs, right side shows evolution up to ∼100 ps.

The TA spectrum of the initially excited S_2 state has several broad ESA features in cyclohexane, including a prominent band near 485 nm and weaker bands near 600 and 710 nm.[209,212] The S_2 spectrum is similar for the encapsulated compound, except for additional broadening of the individual ESA bands. In both cases, the S_2 spectrum decays within the ∼100 fs time resolution of our experiment and is replaced by a spectrum that is very similar to what we observe following direct $n\pi^*$ excitation to S_1 at lower energy. An isobestic point near ∼450 nm confirms direct relaxation from S_2 to S_1 in both environments. The slightly broader S_1* spectrum for $\pi\pi^*$ excitation probably reflects excess vibrational energy in that state following internal conversion from the higher-energy S_2 compared with direct excitation at 470 nm.

5.3.1.3 Excitation of Alkyl-Substituted Azobenzenes at 320 nm

We probe the dynamics following $\pi\pi*$ excitation at 320 nm for the entire series of alkyl-substituted compounds (Figure 5.2) in solution and in the OA_2 capsule. Figure 5.6 compares the ground-state $\pi\pi^*$ absorption bands for the series of compounds in both environments. The ground-state spectra of all six molecules have similar vibronic structure in cyclohexane, with subtle shifts of the absorption band to longer wavelength with the addition of one or two alkyl substituents. The absorption bands shift to slightly longer wavelength upon encapsulation, especially the di-substituted compounds, *t*-Me_2Az and *t*-EtMeAz. The vibronic progression also becomes significantly less pronounced in the capsule compared with solution for the longer alkyl-substituted compounds, *t*-EtAz and *t*-PrAz. The reduced vibronic structure suggests that these molecules may have a distorted, non-planar equilibrium geometry inside the OA_2 capsule.[6]

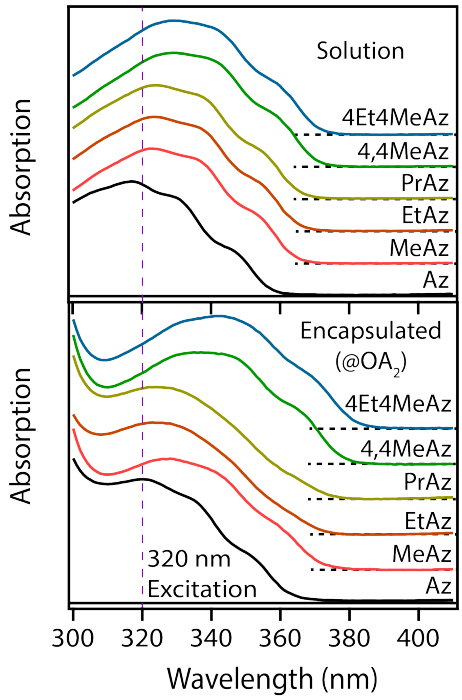

Figure 5.6: Ground-state $\pi\pi*$ absorption band for the series of *t*-Az derivatives in cyclohexane (top panel) and in the OA_2 capsule (bottom panel). Vertical dashed line indicates the excitation wavelength of 320 nm.

The TA spectra for all five of the substituted compounds (Figure 5.7 and 5.8) are very similar to the spectra for $\pi\pi*$ excitation of unsubstituted *t*-Az in the two environments, and the excited-state

lifetimes are very similar for all of the compounds in solution. However, the excited-state decay times of the encapsulated compounds are much longer than in solution, and depend on the number and length of alkyl substituents. There are also some other subtle, but important differences in the evolution of the TA spectra for the encapsulated compounds that are only evident from global fits to the data that we discuss below.

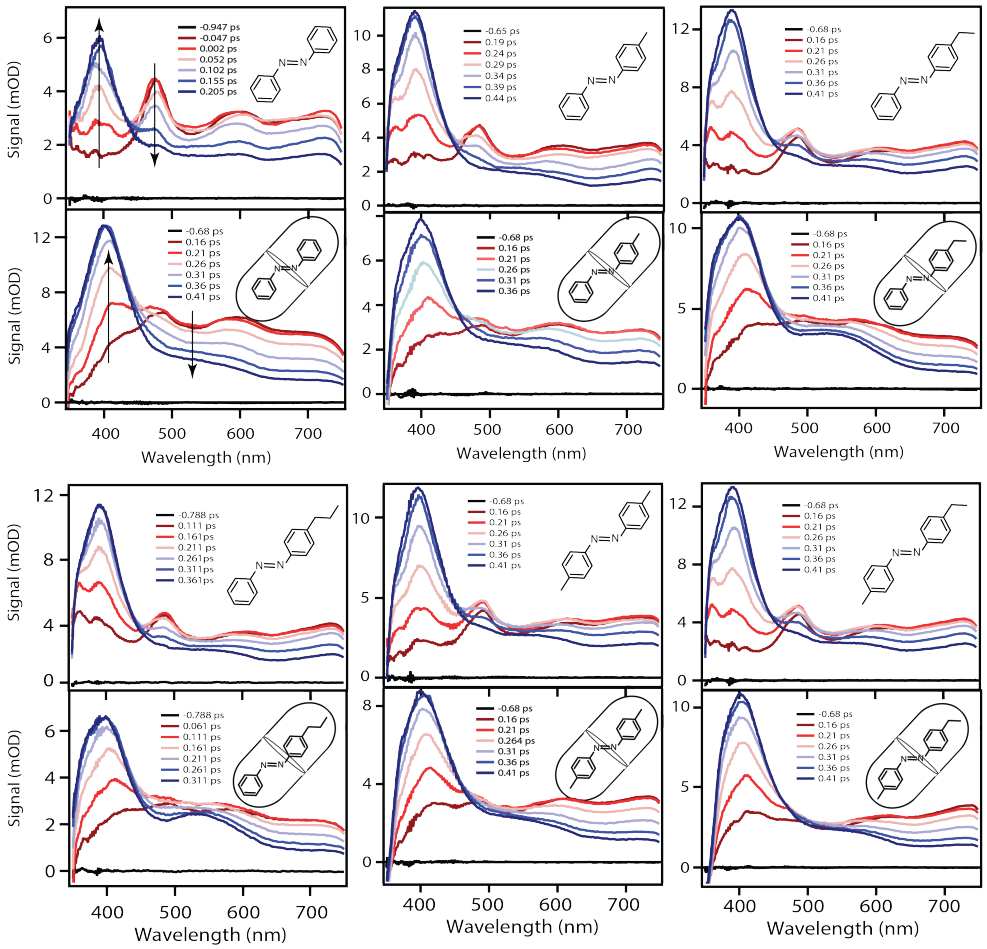

Figure 5.7: Evolution of the transient absorption spectra after $\pi\pi^*$ excitation of azobenzene in cyclohexane and in the OA_2 during the first few hundred fs.

The *trans*→*cis* photoisomerization quantum yields ($\Phi_{t\to c}$) for all six compounds are listed in Table 5.1. The quantum yields are very similar for all of the compounds in solution, ranging from 0.10 to 0.15, but vary considerably for the encapsulated compounds.[213] Notably, the quantum yield increases with chain length for the encapsulated mono-substituted compounds, from 0.05 for unsubstituted *t*-Az@OA_2 to 0.17 for the molecule with the longest alkyl chain, *t*-PrAz@OA_2. In-

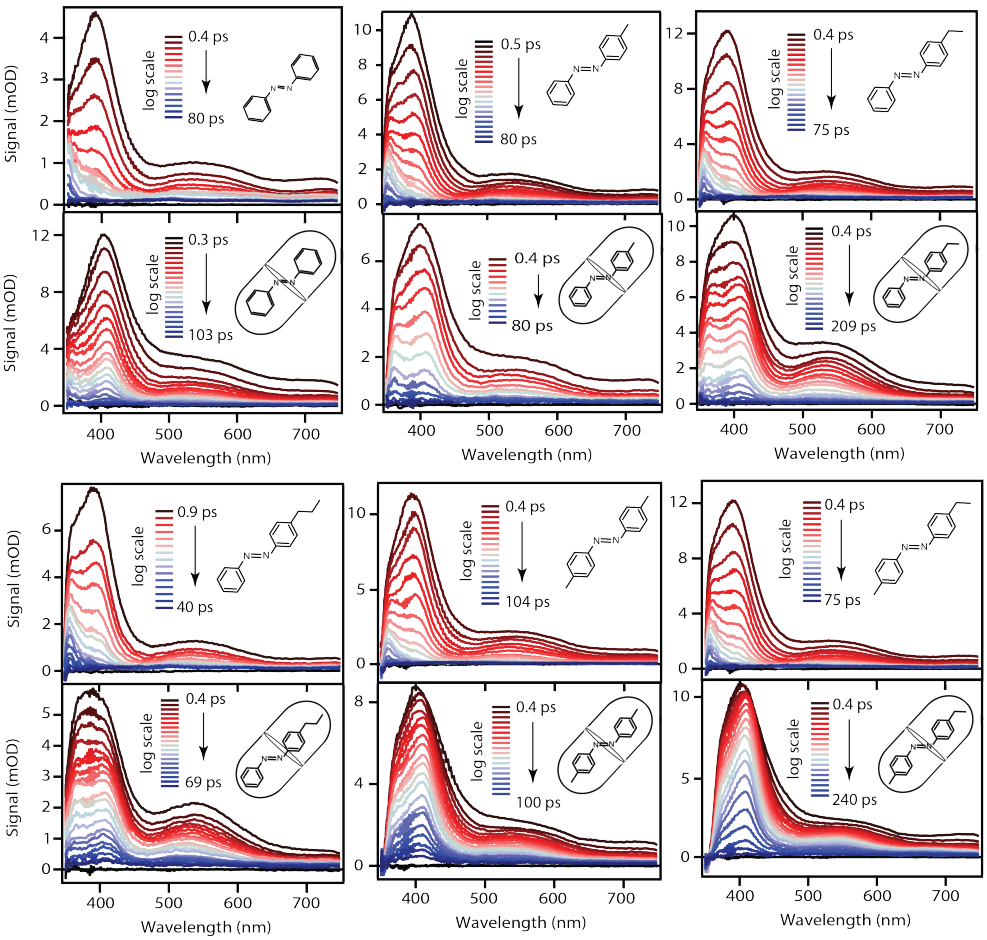

Figure 5.8: Evolution of the transient absorption spectra after $\pi\pi^*$ excitation of azobenzene in cyclohexane and in the OA_2 from ∼0.3 ps to ∼100 ps.

terestingly, the value for *t*-PrAz@OA_2 is even larger than the quantum yield for the same molecule in solution. In contrast with the mono-substituted compounds of similar total length, the quantum yields for the encapsulated dialkyl-substituted azobenzenes *t*-Me_2Az@OA_2 and *t*-EtMeAz@OA_2 are only 0.05 and 0.03, respectively, are much lower than in solution.

5.3.2 Kinetic Models

Global fits to the TA spectra reveal more detailed information about the excited-state dynamics of *t*-Az and *t*-Az@OA_2. We begin with singular value decomposition (SVD)[214] and global fits to the data with a sum of exponentials in order to determine the smallest number of time constants that are necessary to accurately reproduce the evolution of each TA spectrum, then apply target

Table 5.1: Photoisomerization quantum yields[a] and excited-state lifetimes[b] for $\pi\pi^*$ excitation

	t-Az	*t*-MeAz	*t*-EtAz	*t*-PrAz	*t*-Me_2Az	*t*-EtMeAz
Solution						
$\Phi_{t\rightarrow c}$	0.11(4)	0.10(4)	0.15(4)	0.12(4)	0.13(4)	0.13(4)
τ_{S_1} (ps)	2.6	1.8	2.3	2.5	2.4	2.6
Encapsulated						
$\Phi_{t\rightarrow c}$	0.05(3)	0.10(4)	0.12(4)	0.17(4)	0.05(3)	0.03(2)
τ_{S_1} (ps)	13	15	21	26	35	55
$\tau_{S'_1}$ (ps)	2.4	2.4	3.8	5.6	3.3	3.5

[a] For *trans*→*cis* isomerization, estimated 2σ uncertainties of the absolute quantum yield in parentheses. Relative uncertainties are smaller due to back-to-back measurement under identical conditions.

[b] From global fits to the data using kinetic models described in the text.

analysis to extract species-associated spectra (SAS) using more restrictive kinetic models.[215] The SAS represent individual states in the kinetic model, and the time evolution of the overall spectrum is restricted by the allowed pathways between states in the model. The time constants are allowed to vary to obtain the best fit, except where indicated otherwise. All of the fits include convolution with a Gaussian instrument response function with FWHM of 100 fs.

5.3.2.1 $n\pi^*$ Excitation

Figure 5.9 shows the SAS and associated time constants that we obtain from the kinetic models for $n\pi*$ excitation of the pure sample of *t*-Az in solution and the mixture of isomers in the capsule at PSS. We model the kinetics in cyclohexane based on previous work showing a competition between relaxation pathways in the excited state.[5,216] The model begins with vibrationally excited S_1* that relaxes through two competing channels, one that returns directly to the ground state in $\sim$1 ps, and a second that undergoes vibrational relaxation in S_1 before returning to the ground state on a timescale of 2.4 ps. This branching in the excited state represents a bifurcation between one pathway that directly accesses a conical intersection with the ground state and a second pathway that relaxes to a minimum-energy structure in the excited state before crossing a barrier to reach the conical intersection.[62] Both channels lead to the vibrationally hot ground state, S_0*, which then

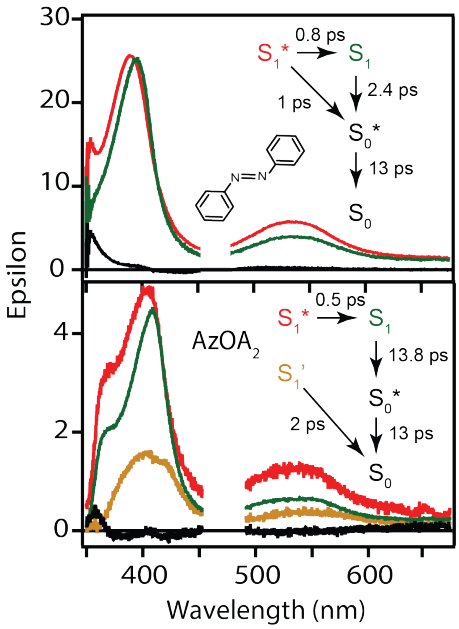

Figure 5.9: Species-associated spectra for *t*-Az in cyclohexane (top) and mixed *t*-/*c*-Az@OA_2 at PSS (bottom). The kinetic models and the lifetimes from the global fits are shown as insets. See text for details.

dissipates energy to the solvent to reach the equilibrated S_0 on a timescale of 13.0 ps. We do not distinguish between the *cis* and *trans* isomers in the relaxed ground state, because neither has an appreciable absorption in this range of probe wavelengths. Importantly, the SAS from the fits are consistent with the kinetic model, including a slight shift and narrowing of the primary ESA band from S_1* to S_1, and the tail of S_0* below 360 nm due to broadening of the hot ground-state $\pi\pi*$ absorption band for S_0* compared to S_0.[209]

The bottom panel of Figure 5.9 shows the SAS that we obtain for $n\pi$* excitation of Az@OA_2 at PSS using a kinetic model with parallel contributions for the *cis* and *trans* isomers. The kinetic model for relaxation of *t*-Az@OA_2 is similar to the model in solution, except that we do not observe a rapid decay of the ESA band within the first ps for the encapsulated molecule, and therefore do not include a direct relaxation channel from S_1* to S_0 in the capsule. Instead, the ESA band decays on a single timescale of 13.8 ps, compared with 2.4 ps in solution. Despite the very different lifetimes, the SAS for *t*-Az@OA_2 are remarkably similar to the spectra in cyclohexane. Although it is unnecessary to include ground-state vibrational cooling (S_0*→S_0) in order to accurately re-

produce the TA spectrum for the encapsulated sample, we find that adding this component with a fixed lifetime of 13.0 ps recovers a weak signature below 375 nm that is similar to the vibrationally hot S_0* in solution. The spectrum for S_0* is much noisier in the capsule because the hot ground state cools on the same timescale as the electronic relaxation from S_1.

In addition to the excited-state dynamics of the encapsulated *trans* isomer, the global fits for the sample of mixed isomers in the capsule reveal the excited-state spectrum of *c*-Az@OA_2, which decays with a lifetime of 2.0 ps. The SAS for this feature has absorption bands near 400 and 550 nm (gold spectrum in Figure 5.9) that closely resemble the ESA spectrum that was previously reported following nπ* excitation of *cis*-Az in solution.[63] Although the 2.0 ps lifetime that we measure for the encapsulated *cis* isomer is significantly longer than the $\sim$100 fs lifetime previously reported for *c*-Az in solution,[63,209,217] this difference is similar to the longer lifetime of the *trans* isomer in the capsule.

5.3.2.2 $\pi\pi$* Excitation

We analyze the evolution of the TA spectrum following $\pi\pi$* excitation of *t*-Az in cyclohexane using the same kinetic model as $n\pi$* excitation, except for the addition of an initial relaxation step from S_2 to S_1*. In order to improve the quality of the fits, we fix the $S_2 \rightarrow S_1*$ relaxation time at 50 fs, based on measurements with higher time resolution by Nenov, *et al.*[216]. The top panel of Figure 5.10 shows the resulting SAS from target analysis of the TA spectra in cyclohexane. The spectra we obtain for S_1*, S_1, and S_0* are all very similar to the spectra from $n\pi$* excitation of *t*-Az in cyclohexane, with some additional broadening of S_1* that is probably a signature of excess vibrational energy in that state following internal conversion from S_2.[184] The spectrum for S_2 is distinct from the other states, and includes a negative stimulated emission band centered near 400 nm that matches the $S_2 \rightarrow S_0$ fluorescence band that was previously reported following $\pi\pi$* excitation of *t*-Az.[64,218]

Unlike solution, the model for $\pi\pi$* excitation of *t*-Az@OA_2 requires an additional component to accurately reproduce the time evolution of the experimental TA spectrum. The additional con-

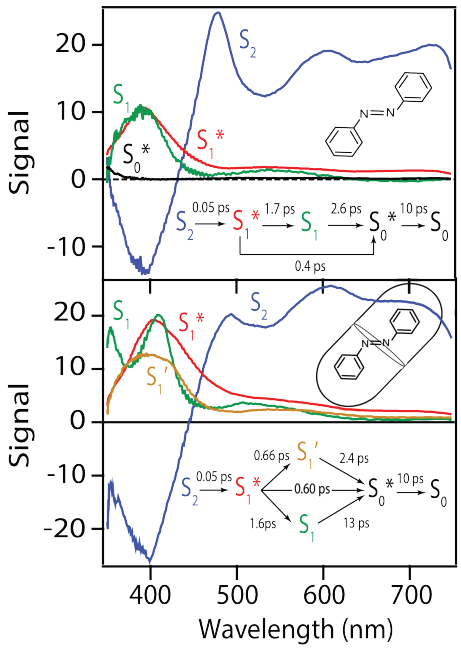

Figure 5.10: Species associated spectra for azobenzene in cyclohexane (top) and the OA_2 capsule (bottom). The spectra are from global fits to the transient absorption spectra using the kinetic models in the in set. See text for details.

tribution to the TA spectrum for *t*-Az@OA_2 compared with solution is evident from SVD and the global fits to the data using a sum of exponentials, both of which suggest that a total of at least five time constants are necessary to accurately reproduce the evolution of the TA spectrum for the encapsulated sample. Thus, we include an additional feature (S_1') for the encapsulated sample, in addition to the initially excited S_2. The kinetic model that gives the best agreement with experiment is shown in the bottom panel of Figure 5.10, along with the resulting SAS from the target analysis. We tested several different kinetic models, but only this model, which includes three distinct channels for the relaxation of S_1*, gives a good fit to the data and also is consistent with the results from above. We exclude other kinetic models based on poor fits to the data or unreasonable results, such as SAS with negative spectral features above 500 nm or artificially short lifetimes (*i.e.* <50 fs) for species other than S_2.

The SAS for the S_2 and S_1* states of *t*-Az@OA_2 are similar to the spectra in solution, and decay on roughly the same two time scales ($\sim$50 fs and $\sim$300 fs, respectively) in both environments. As before, we use a fixed lifetime of 50 fs for S_2, and convolute the fits with an instrument-limited

resolution of 100 fs. Similar to solution, but unlike the case of $n\pi*$ excitation for *t*-Az@OA_2, we observe rapid decay of the TA signal that we attribute to a direct relaxation channel from S_1* to S_0*. However, the most unique aspect of the model for $\pi\pi$* excitation of *t*-Az@OA_2 is the presence of two distinct excited-state species with lifetimes of 2.4 and 13 ps, respectively. We assign the species with a lifetime of 13 ps as the relaxed S_1 excited state of *t*-Az@OA_2, based on the similar spectrum and lifetime that we observe following $n\pi*$ excitation. Importantly, both the SAS and the 2.4 ps lifetime of the other feature almost perfectly match the spectrum and lifetime for direct $n\pi$* excitation of *c*-Az@OA_2. Thus, we tentatively assign the new species as the *cis* excited state, even though we excite only the *trans* isomer of the encapsulated compound at 320 nm. Formation of the *cis* excited state after $\pi\pi*$ excitation of *t*-Az@OA_2 implies adiabatic isomerization in the excited state.[5]

5.3.2.3 Alkyl-Substituted Azobenzenes

Global fits to the TA spectra for $\pi\pi*$ excitation of the five alkyl-substituted compounds in cyclohexane using the same kinetic model as we used for unsubstituted *t*-Az gives similar lifetimes and SAS for all six compounds. The top panel of Figure 5.11 shows the S_1 spectra, and Table 5.1 summarizes the S_1 lifetimes. The full set of SAS for each compound are presented in Figure 5.12. In contrast, the kinetic model for $\pi\pi*$ excitation of unsubstituted *t*-Az@OA_2 works well for the mono-substituted derivatives, but gives a poor fit to the data for the di-substituted azobenzenes, Me_2Az@OA_2 and EtMeAz@OA_2. In the case of the di-substituted compounds, the TA spectra do not rapidly decrease in intensity after the initial electronic relaxation to S_1*, therefore we use a kinetic model for these two compounds without the direct S_1*$\rightarrow S_0$* relaxation channel, similar to the model for $n\pi*$ excitation of *t*-Az@OA_2. Other than the fast electronic relaxation channel, the models are the same for all six encapsulated compounds, and give SAS that are very similar for the S_2, S_1*, and S_1 states of each compound. However, the lifetimes of S_1 are sensitive to alkyl substitution, and the SAS that we obtain for the second excited-state species, S_1', varies across the series of molecules.

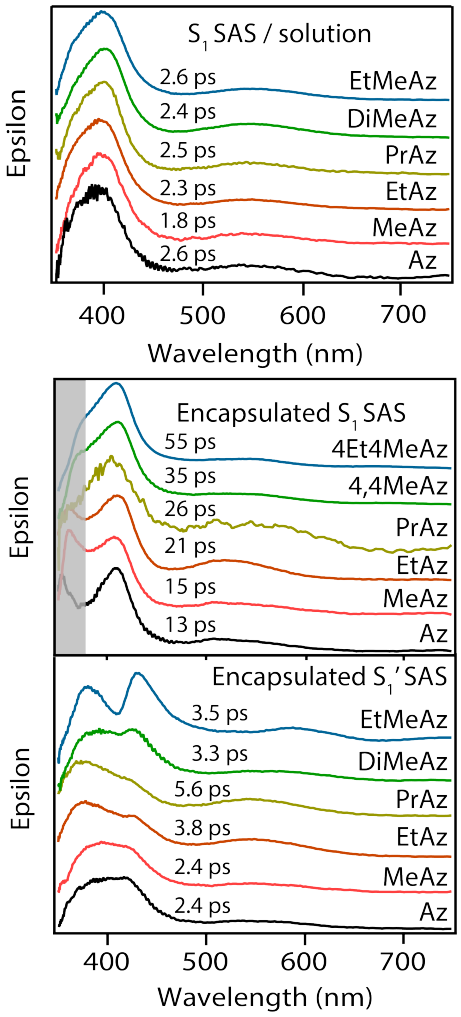

Figure 5.11: Top panel shows the species associated spectra series for S_1 in solution. Below is a stacked panel with the S_1 and S_1' SAS inside the OA_2 capsule. Shaded region is for artificial rise in the SAS.

The lower panels of Figure 5.11 compare the S_1 and S_1' spectra for the series of compounds in OA_2, and the lifetimes are summarized in Table 5.1. The fits for all of the encapsulated compounds use a fixed lifetime of 50 fs for the S_2, as before, and we hold the S_0* lifetime at 10 ps due to the insensitivity of the fit to this small-amplitude signal. The similar timescale for electronic relaxation of S_1 and vibrational cooling of S_0* appears as an artificial increase of the absorption S_1 absorption spectrum below $\sim$360 nm for some of the encapsulated compounds, therefore we shade that region of the spectrum in the middle panel of Figure 5.11.

The S_1 lifetimes increase with increasing alkyl chain length for the encapsulated compounds,

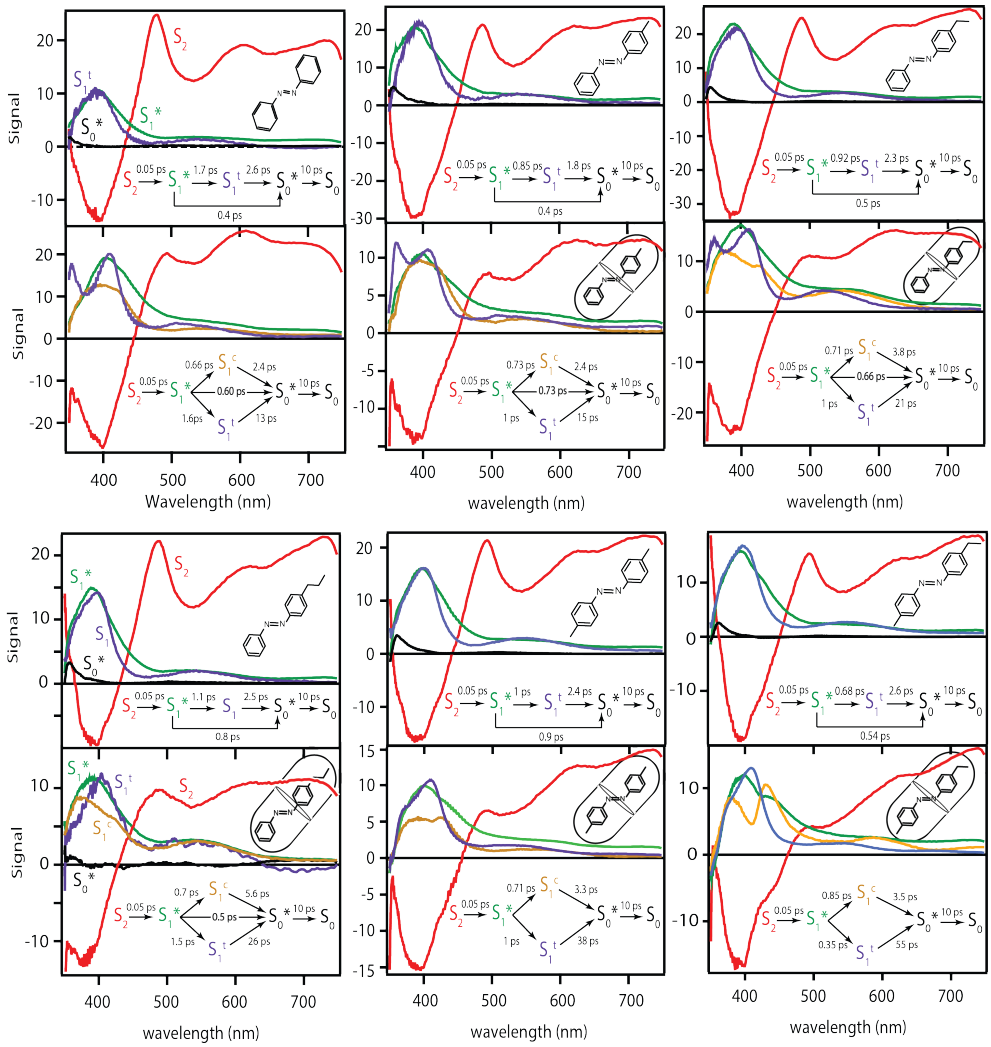

Figure 5.12: Species associated spectra for *t*-Az series after $\pi\pi^*$ excitation with the model used shown as the inset.

but the SAS are nearly the same in every case, and also resemble the S_1 spectra in solution. Although shorter than the S_1 lifetimes, the S_1' lifetimes also increase with chain length for the mono-substituted compounds. The di-substituted compounds have the longest S_1 lifetimes, but intermediate lifetimes for S_1'. Notably, the spectra for S_1' of the di-substituted compounds have a different shape than the spectra for the mono-substituted compounds, which have broadened double peaked spectral bands at 395 and 440 nm.

5.4 Discussion

5.4.1 Confined Excited-State Dynamics

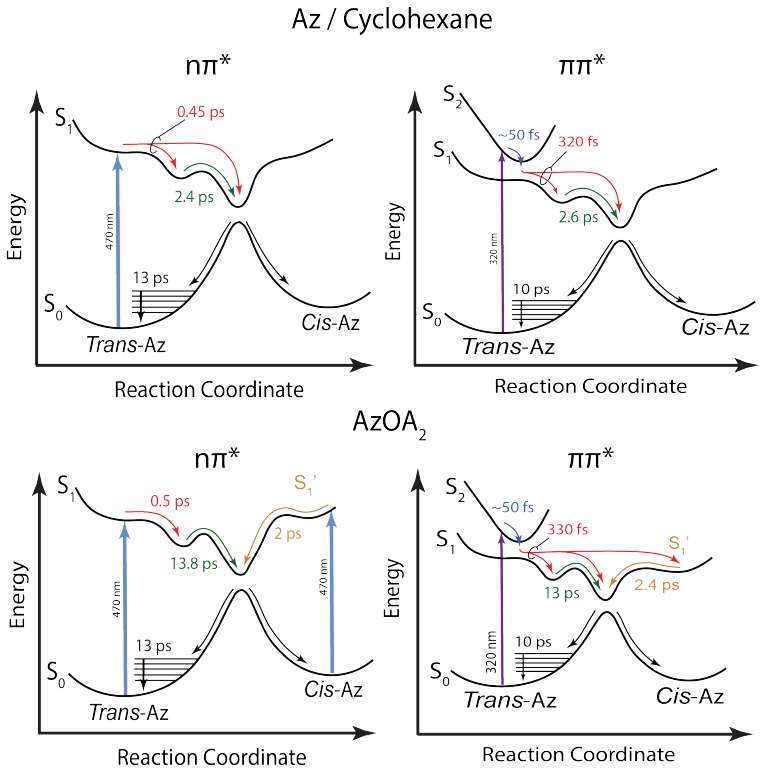

Figure 5.13: Schematic diagram of the potential energy curves for Az in cyclohexane and Az@OA_2. The left side shows the reaction pathway for nπ* excitation, and the right side shows $\pi\pi$* excitation.

The left side of figure 5.13 shows a schematic potential energy diagram for *t*-Az in solution (top), and the *cis*-Az and *t*-Az in the capsule (bottom) after nπ* excitation at 470 nm. For direct comparison, the *t*-Az mechanism after $\pi\pi$* excitation at 320 nm is shown to the right of the nπ* schemes, with the solution and OA_2 capsule environments stacked respectively. The mechanism for nπ* excitation of *t*-Az in solution has several similar pathways as that of the $\pi\pi$* excitation which was reported previously and is described briefly here.[5,209] For *t*-Az in solution, initial excitation populates the S_1 excited-state with some molecules structurally and vibrationally relaxing on the S_1 surface, while the other subset of molecules directly relax to the ground electronic state S_0 along the concerted inversion-assisted rotation coordinate before reaching a conical intersec-

tion (CoIn) that brings the molecules back to the ground-state. The CoIn determines the branching between the *trans* and *cis* isomers as the molecules return to the ground electronic state.

The encapsulated *t*-Az isomer follows a similar relaxation mechanism as in solution, except that here is not a direct pathway from S_1* to the ground electronic state. The absence of the direct pathway back to the ground state suggests the confined environment distorts the equilibrium geometry, resulting in a hindered pathway along the inversion-assisted rotation coordinate that prevents direct access to the CoIn with a lifetime of 13 ps. From the relaxed S_1 state, the molecules follow a reaction coordinate with a larger barrier to reach the CoIn, resulting from the distorted out-of-plane equilibrium geometry due to crowding in the confined environment.[6] The out of plane structure is uniquely different from Az in solution, where the minimum energy pathway starts from a planar structure on the S_1 surface.[62] In contrast, nπ* excitation of *cis*-Az in the capsule populates an excited-state with a lifetime of 2 ps. The spectrum of the *cis* excited-state is similar to the spectrum that we observe following direct $\pi\pi$* excitation of *cis*-Az in solution. The 2 ps lifetime is significantly longer than the sub 100 fs lifetime measured for *cis*-Az in solution.[209] Based on the similar spectrum of the *cis*-Az in solution and inside the OA_2 capsule we assign the S_1' species to a *cis*-like excited-state.

The illustrations on the right side of figure 5.13 show the relaxation pathway of *t*-Az in solution and in the OA_2 capsule after $\pi\pi$* excitation. Exciting the $\pi\pi$* transition adds an extra step in the mechanism for *t*-Az due to the relaxation from the very short lived S_2 state. The excited molecules relax quickly to the S_1 state, and then follow a similar pathway as we observe following nπ* excitation.[207] The similar pathway in solution is nearly identical to the SAS for the S_1* and cooled S_1 species after nπ* and $\pi\pi$* excitation, which point to similar molecular geometries for the two species after their respective excitation.

In contrast, the relaxation mechanism following $\pi\pi$* excitation for *t*-Az@OA_2 includes two separate excited-state species, in addition to the fast relaxation channel to the ground-state. One of the excited-state species is the relaxed *trans* isomer, which has a similar spectrum and lifetime after nπ* excitation of *t*-Az in the OA_2 capsule. The other excited-state species has a similar SAS as the

encapsulated *cis*-Az isomer after nπ* excitation, therefore we assign the S_1' species as the relaxed excited-state of a *cis*-like isomer. Additionally, this pathway shows that the *cis*-like geometry is accessed from the excited *trans* geometry on the S_1 surface, which is a pathway not observed after $\pi\pi$* excitation of *t*-Az in solution. The pathway to the S_1' species from the *trans* geometry happens on the time scale for accessing the CoIn directly, which suggests that if a the molecule misses the CoIn due to crowding, it could get trapped on another part of the PES. In a similar study using an encapsulated stilbene derivatives, results show the rotation channel is greatly restricted, indicating the isomerization mechanism for the *trans* to *cis* isomer in the excited-state must follow the inversion coordinate to access the *cis* isomer.[6]

5.4.2 Crowding Effects

In order to probe the role of crowding on the reaction dynamics of *t*-Az after $\pi\pi$* excitation, we probe the dynamics for increasing alkyl-chain length. In solution the relaxation mechanism after $\pi\pi$* excitation is insensitive to the substitutions, evident from the similar SAS and lifetimes (see figure 5.12). The similar lifetimes are due to the substituents having little influence on the π-conjugation, as well as being located at the para position on the phenyl ring where they cannot cause sterical hindrance during the isomerization reaction.

For $\pi\pi$* excitation across the series of *t*-Az derivatives in the OA_2 capsule, the timescale for the early relaxation from S_2 to S_1 state and the vibrational and structural relaxation on the S_1 are close to that of the solution measurements, indicating the early relaxation processes are insensitive to the confined environment.[107] For the mono-substituted Az derivatives, the relaxation on the S_1 surface follows three pathways, which lead to the relaxed S_1 *trans* geometry, ground electronic S_0 state, and the *cis*-like S_1' species. We see very similar relaxation pathways on the S_1 surface for the encapsulated di-substituted Az derivatives, with the only difference being a missing pathway directly from S_1* to the ground-state.

The series of Az derivatives in the OA_2 capsule have increasing S_1 lifetimes as the molecule becomes longer. The increasing lifetime is a result of crowding inside the capsule for longer

alkyl-chains, which increasingly distorts the geometry of the molecule. Evidence for the distorted geometrical structures in shown in the ground-state absorption spectrum, which shows Az@OA_2 and MeAz@OA_2 with vibronic structure in the spectra indicating a more planar geometry, meanwhile EtAz@OA_2 and PrAz@OA_2 show smooth spectra with no vibronic character suggesting an out-of-plane bent structure.[6] Additionally, Me_2Az and EtMeAz are the same length as EtAz and PrAz respectively, but show vibronic structure in the ground-state spectrum due the substituents being at both ends of the molecule, which lock the molecule into a more distorted structure. The effect on having an out-of-plane molecular structure in the excited states then restrict the inital in-plane bending of the inversion-assisted rotation mechanism, suggesting the first motion for the Az derivative is to planarize which is made difficult by the confined space of the capsule.

The unsubstituted and mono-substituted Az molecules that relax to the S_1' state on the S_1 potential energy surface have a similar SAS, but with subtle differences in the relative intensities of the two peaks. The small differences in the spectral shape of the SAS point to differences in the *cis*-like geometrical structure, possibly due to steric hindrance in the confined environment. The increasing lifetime with increasing alkyl chain length points to a more stabilized *cis*-like excited-state structure for longer Az derivatives. The SAS for the S_1' species of the di-substituted derivatives have a more pronounced absorption band at longer wavelengths compared with the mono-substituted S_1' SAS. Given the lack of SAS structural resemblance of the S_1' species between the mono and di-substituted Az derivatives, we do not assign the S_1' species for the di-substituted Az derivatives to a *cis*-like geometry. Instead the S_1' species for the di-substituted Az derivatives in the OA_2 capsule is likely to be a highly distorted out-of-plane structure that gets trapped due to the confined environment, and the relaxation from the out-of-plane structure has a lifetime that does not continue increase across the Az@OA_2 series. Given the unusual environment of the OA_2 capsule as well as the the highly distorted out-of-plane structure of the S_1' species, molecular dynamics simulations would provide valuable insight about the system and the interactions taking place during the photoisomerization reaction.

5.5 Conclusion

The ultrafast spectroscopy for a series of encapsulated alkyl-substituted azobenzene derivatives provides insight into the fundamental photoisomerization reaction during nπ^* and $\pi\pi^*$ excitation. In comparison to the azobenzene derivatives in solution we observe the encapsulated azobenzene molecules to have increasing excited-state lifetimes with increasing molecular length when relaxing from the S_1 state due to the increasing sterical hindrance for phenyl rotational motion within the capsule. The confined environment opens up an additional relaxation pathway leading to a S_1' species, which for the mono-substituted derivatives resembles the formation of the *cis* excited-state isomer. Restricting the excited-state dynamics with di-substitution at the 4 and 4' positions of the azobenzene molecule greatly impedes the inversion mechanism, which results in significantly lower *trans* $\rightarrow$ *cis* quantum yields and an S_1' species that has a highly out-of-plane distorted geometry. The fundamentally different behavior observed in the confined environment demonstrates the importance of understanding the unique mechanisms for the isomerization of azobenzene.

Chapter 6

Photodecomposition Mechanism for Manganese Tricarbonyl Complexes from Transient X-ray Absorption Spectroscopy

6.1 Introduction

The conversion of CO_2 into renewable, carbon-neutral fuels and chemical feedstocks is a promising route to sustainability.[66] A key step in that direction is the development of inexpensive, efficient, and robust catalysts for the selective reduction of CO_2 to CO, which can then be used as a reagent in the Fischer-Tropsch process, carbonylation, hydroformylation, or other commercially important reactions.[219–223] Metal coordination complexes, including rhenium and manganese tricarbonyl complexes, are among the most efficient molecular catalysts currently available for electrochemical reduction of CO_2. The rhenium compounds have excellent stability and efficiency, but Re is potentially toxic and too expensive to be feasible for large-scale production. The manganese complexes, on the other hand, offer a promising alternative based on a cheaper, earth-abundant, and non-toxic metal.[224,225] Unfortunately, the Mn catalysts are susceptible to photo-decomposition under exposure to visible light, which is a key limitation that must be overcome for widespread and economical conversion of CO_2.[71–74]

New design strategies to improve photochemical stability upon exposure to visible light while retaining favorable catalytic activity of the Mn complexes requires a deep understanding of the decomposition mechanism. Toward that goal, we recently examined the fundamental photochemistry for a series of Mn complexes with substituted 2,2'-bipyridine (bpy) ligands using ultrafast spectroscopy.[226] The addition of electron-donating or electron-withdrawing substituents on the bpy

ligand tunes the electronic properties of the complex, and therefore affects both the photostability and the catalytic activity of the Mn complex for CO_2 reduction.[225] Figure 6.1 shows the absorption spectra for the series of $Mn(CO)_3(^{L_2}bpy)Br$ compounds in acetonitrile, where $L = t$Bu, H, CF_3 and NO_2 are substituents at the 4 and 4' positions of bpy. The compounds have MLCT bands centered near 400, 410, 480, and 520 nm, respectively, with a much stronger bpy($\pi\pi^*$) intraligand (IL) absorption band below 385 nm. All of the compounds degrade after several minutes of exposure to ambient light, as evident from a color change of the solution and formation of a precipitate.[71] Previous measurements also detected CO in the head space of irradiated Mn(^{L}bpy) samples using gas chromatography.

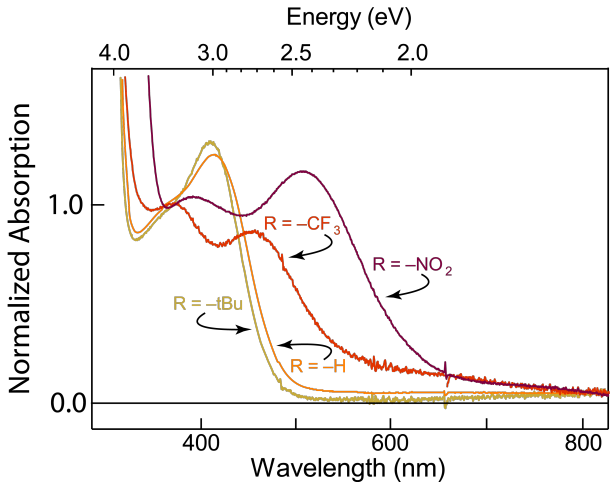

Figure 6.1: Normalized ground-state absorption for the Mn(^{L}bpy) series emphasizeing the difference in the MLCT band.

Several groups examined the photodegradation of $Mn(CO)_3$(bpy) compounds using UV-vis and IR absorption spectroscopy under continuous irradiation with light, but a complete mechanism for the decomposition of these species remains elusive.[75,76] Our ultrafast spectroscopy measurements revealed several fundamental steps in the photochemistry of the Mn complexes that may be important in the photodegradation process. The optical transient absorption (TA) measurements suggest that the earliest step involves rapid relaxation of the initial MLCT state to a dissociative ligand-field state that eliminates one of the CO ligands within ~300 fs. Our measurements also suggest that the missing CO ligand is subsequently replaced by a coordinating solvent molecule

on a timescale of 40-80 ps, depending on the identity of the bpy ligand and the solvent. Unlike acetonitrile, we did not see evidence of solvent coordination in chloroform. The TA measurements examined the reaction up to a few hundred ps, but additional steps in the decomposition chemistry occur on longer timescales. Based on steady-state measurements, the ultimate decomposition product is likely to be a Mn dimer species that is formed through diffusion-controlled bimolecular reactions. Although ultrafast spectroscopy provides more detailed information than was available from earlier steady-state measurements, the full photodecomposition mechanism of the Mn complexes remains unclear. More detailed structural information is necessary to confirm the proposed mechanism and provide feedback for the development of next-generation Mn catalysts that maintain activity while avoiding decomposition. Open questions include the structure and identities of the proposed intermediates, and especially the influence of ligand substitution and solvent identity on subsequent reactions.

In this chapter we examine the photodecomposition reaction using time-resolved x-ray absorption spectroscopy (TR-XAS) for the series of $Mn(CO)_3(^{L_2}bpy)Br$ complexes in Figure 6.1. TR-XAS probes the electron density and ligand structure of Mn on a ps-μs timescale, and therefore is uniquely suited to probing the structures and the reactions of intermediates that we were unable to probe in the optical TA measurements. As in our earlier study, we examine the photochemistry as a function the electron donating or withdrawing character of the substituted bpy ligand, and also compare the dynamics in dichloroethane (DCE) and acetonitrile (MeCN) solvents in order to capture the proposed 5- and 6-coordinate species following CO loss and solvent coordination, respectively. The results provide important new information about the photodecomposition pathway of manganese tricarbonyl catalysts.

6.2 Experimental Methods

$Mn(CO)_3(^{L_2}bpy)Br$ complexes, abbreviated as $Mn(^{L}bpy)$, were synthesized and purified using procedures described elsewhere.[226] We confirm the purity of the compounds using ^1H NMR and IR spectroscopy. Working under dim red light, we prepare a fresh sample for every run by dilution in

a volumetric flask to a concentration of 1 mg/mL. We keep all sample solutions covered or in the dark, and use only dry solvents, either acetonitrile (Fisher Scientific, $\geq$99.9%), chloroform (Fisher Scientific, $\geq$99.9%), or dichloroethane (Fisher Scientific, $\geq$99.8%).

The TR-XAS measurements were performed at beamline 7ID-D of the Advanced Photon Source (APS) using an optical pump and x-ray probe.[103] The pump pulses come from the output of a high repetition rate laser (Time-Bandwidth Products, Duetto) with a center wavelength of 1064 nm and pulse duration of 10 ps. Second and third harmonic generation in lithium triborate (LBO) crystals produces pump pulses with up to 0.6 μJ/pulse at 532 and 355 nm, respectively. We focus the pump beam to a diameter of $\sim$25 μm at the sample where it intersects the x-ray probe beam at a small angle. The laser is synchronized with the x-rays from the synchrotron operating in 24 bunch mode. In this mode, the storage ring has 24 circulating electron bunches that produce x-rays with a spacing of 153 ns (6.52 MHz repetition rate) and a duration of $\sim$80 ps. We tune the undulator and water-cooled double-crystal diamond (111) monochromator to give x-ray probe pulses in the range 6.510-6.905 keV, with $\sim$1 eV $\Delta E/E$ bandwidth. A Kirkpatrick-Baez mirror focuses the x-ray beam to a spot size of $\sim$5 μm at the sample.[104,105]

We monitor the x-ray absorption strength of the sample by detecting the x-ray fluorescence intensity perpendicular to the direction of the incident beam. We detect the fluorescence using a pair of avalanche photodiodes (APDs) on either side of the sample, with a $Z-1$ chromium filter to absorb scattered x-rays at the incident energy. The APDs measure the fluorescence intensity for every x-ray pulse, but we set the tunable laser repetition rate to 186 kHz, which below the output of the synchrotron. The laser frequency is synchronized with the rf signal from the synchrotron storage ring using a phase-locked feedback loop (Time Bandwidth Products, CLX-1100) to actively adjust the oscillator cavity length. We control the pump-probe delay electronically up to $\sim$50 ns, while simultaneously detecting the fluorescence for up to 13 subsequent probe pulses to measure delays out to $\sim$2 μs in 153 ns increments. We also measure the x-ray pulse that arrives immediately prior to the laser excitation pulse to obtain the ground-state spectrum of the sample. At each electronic time delay, we scan the incident energy to record the x-ray absorption spectrum,

typically averaging the probe signal for at least 10^6 pump pulses per point.

For the x-ray measurements, the sample flows through a round liquid jet with a diameter of $\sim$130 μm and a flow rate of 2.5 mL/min that is fast enough to refresh the sample between laser pulses.[103] Due to the high repetition rate and high intensity of the pump pulses, we discard the sample after a single pass through the jet in order to avoid background signal from the accumulation of photoproducts. Measurements in dichloroethane are complicated by strong x-ray fluorescence from the ionization of chlorine atoms. We reject the background signal by placing Teflon tape in front of the APDs to filter the low-energy x-ray fluorescence from chlorine. Even with the Teflon filter, the signal is much lower in the chlorinated solvent due to attenuation of the incident x-ray probe pulses by solvent ionization.

Optical transient absorption (TA) measurements use the modified output of a regeneratively amplified Ti:sapphire laser operating at 1 kHz. A portion of the 800 nm fundamental laser light drives an optical parametric amplifier to produce tunable UV-vis pump pulses. A second portion of the fundamental drives white-light continuum generation in a circularly translating CaF_2 crystal to produce broadband probe pulses covering the range 350-720 nm. A pair of parabolic silver mirrors collimates and focuses the probe into the sample, where it intersects the 1-2 μJ/pulse pump beam at a small angle. After the sample, the probe pulses pass through a transmissive diffraction grating and onto a 256 pixel photodiode array for shot-to-shot detection. A synchronized chopper blocks every other pump pulse for active background subtraction, and we average 10^3 pulses per time delay. We circulate the sample solution through a quartz flow cell with 0.5 mm path length for the optical measurements.

6.3 Results

The top half of figure 6.2 shows the evolution of the TA spectrum for Mn(^{H}bpy) after 410 nm excitation in MeCN. The evolution at a probe wavelength of 610 nm is shown in the upper-right panel with delay times up to 3 ps on a linear time scale to show the sub ps decay before switching to a logarithmic scale to show signal changes on the tens of ps timescale. In the lower half of the figure,

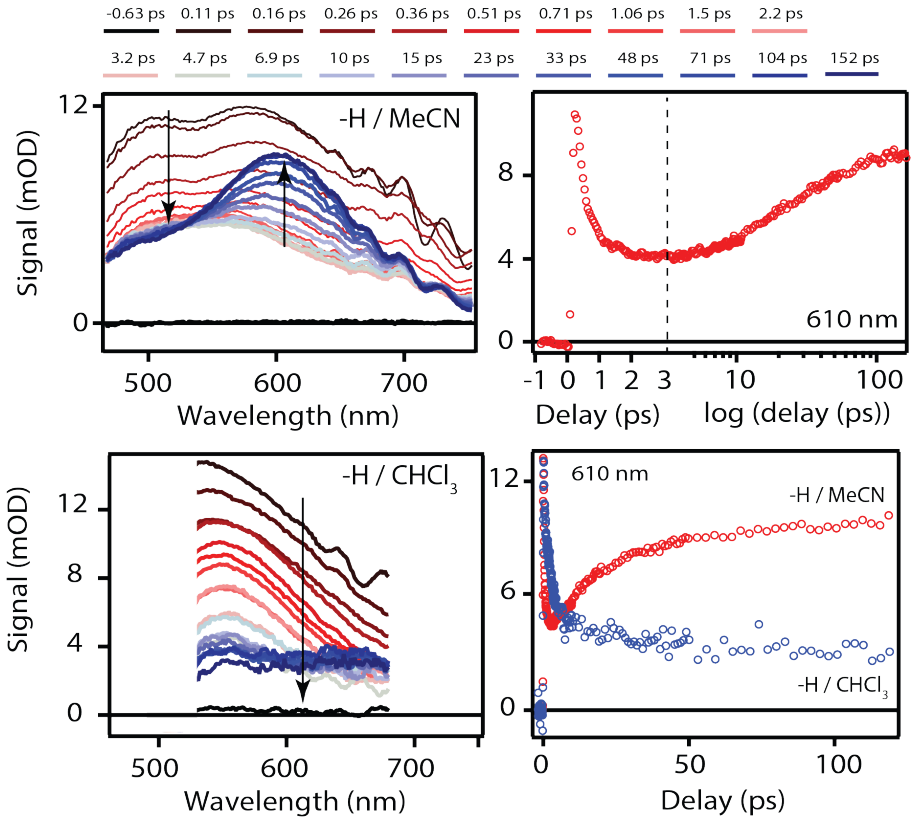

Figure 6.2: Ultrafast transient absorption for Mn(^{H}bpy) in MeCN (top) and chloroform (bottom) with the excited-state decay at 610 nm to the right.

the TA spectrum for Mn(^{H}bpy) after 470 nm excitation is shown in chloroform with the decay at 610 nm to the right and the excited-state decay in MeCN in blue for comparison. The evolution of the TA spectrum is identical for excitations at 355, 420, 470 and 532 nm. For Mn(^{H}bpy) in MeCN the excited-state absorption has a broad spectrum with bands at 510 nm and 590 nm, which quickly decay on the sub-ps time scale due to BET from the bpy ligand to the Mn that leads to CO loss. The electron returns to a higher-lying $d_{x^2-y^2}$ or d_{x^2} orbital of Mn that is dissociative with respect to the Mn-CO bonds, resulting in the loss of an equatorial CO ligand. After the CO release a 5-coordinate Mn complex species is in solution before the growth of an absorption feature at 610 nm on a timescale of 30 ps that we attribute to formation of a 6 coordinate Mn(^{H}bpy)-MeCN complex.[226] Solvent coordination does not occur in chloroform or dichloroethane, therefore the 5 coordinate species survives in theses solvents. In the case of Mn(^{tBu}bpy) and Mn(^{CF_3}bpy) a similar excited-state evolution is observed in the MeCN solvent on the timescales of 39 and 18

ps respectively, indicating a comparable photodissociative pathway compared to the Mn(^{H}bpy) compound.[226]

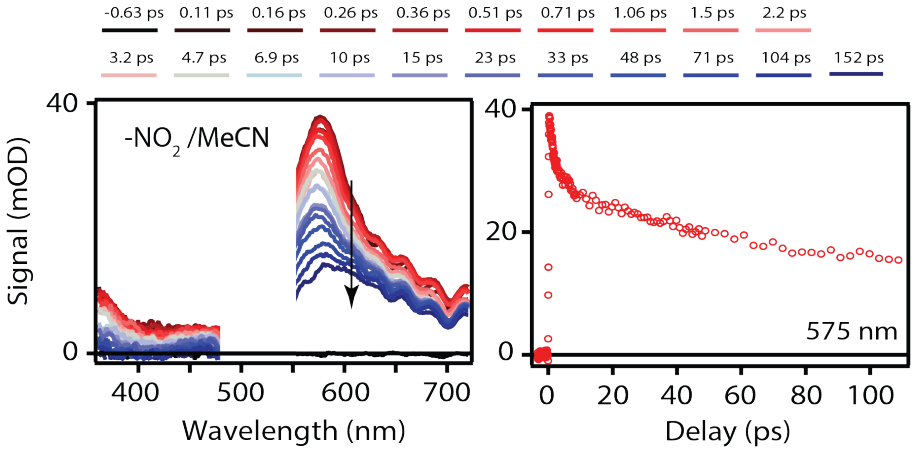

Figure 6.3: Ultrafast transient absorption for Mn(^{NO_2}bpy) in MeCN with the excited-state decay at 575 nm to the right.

The TA spectroscopy for Mn(^{NO_2}bpy) is very different from the other three compounds, suggesting a different relaxation pathway after exciting the MLCT band of this compound. Figure 6.3 shows the excited-state absorption decay for Mn(^{NO_2}bpy) in MeCN after exciting the MLCT at 520 nm, with the excited-state decay at a probe wavelength of 575 nm shown to the right. The pump region of the spectrum is removed due to scattering. The Mn(^{NO_2}bpy) excited-state absorption has a maximum at 590 nm attributed to the bpy anion ([bpy$^{\bullet}$]$^{-}$). The excited-state absorption partially decays on a sub-ps timescale, followed by a slower decay on the hundreds of ps timescale. Due to the NO_2 substituents stabilizing the [bpy$^{\bullet}$]$^{-}$, BET does not occur resulting in no CO ligand dissociation. Therefore, the slow decay of the TA is the relaxation of the [bpy$^{\bullet}$]$^{-}$.

6.3.1 TR-XAS of Mn(^{H}bpy) in MeCN and DCE

Figure 6.4 shows the ground-state XAS K-edge for Mn(^{H}bpy) in MeCN at 6.551 keV with a small pre-edge feature and fine structure oscillations above the edge. Although the Mn complex has a formal oxidation state of Mn^{I}, the position of the edge energy better resembles a formal Mn^{III} in comparison with prior measurements for Mn oxides.[227] The substantially higher K-edge

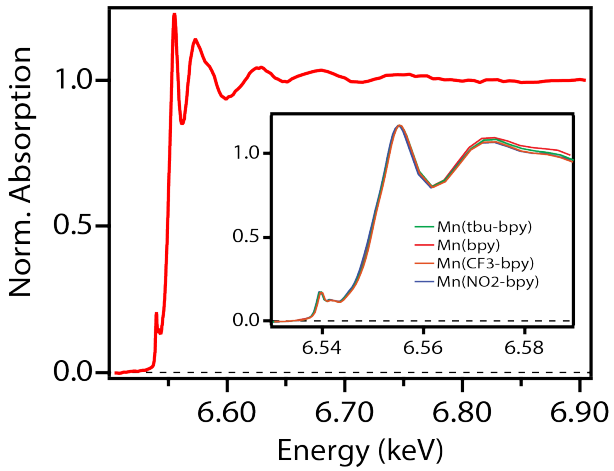

Figure 6.4: Ground-state XAS for Mn(^{H}bpy) and the 3 Mn(^{L}bpy) substituted compound series.

for the formal Mn^{I} complex is due to the strong π-backbonding of the CO ligands, which pulls electron density away from the Mn center. The strength of the pre-edge feature indicates how well the unoccupied 3d orbitals mix with the 4p orbitals and depends on the symmetry of the ligand field. Axial ligands have a larger impact on the unoccupied 3d orbitals and therfore have a strong influence on the pre-edge absorption. The ground-state spectrum of Mn(^{H}bpy) is the same in both MeCN and DCE solvents. The inset compares the XANES region of the spectrum for all 4 Mn(^{L}bpy) compounds. The ground-state XAS for the series of Mn(^{L}bpy) compounds are nearly identical.

Figure 6.5 shows the evolution of the transient spectrum for the Mn(^{H}bpy) complex in MeCN after MLCT excitation at 355 nm. The top left column shows delay times up to 50 ns, with longer delay times in the middle panel. The bottom left panel shows the TR-XAS for Mn(^{H}bpy) in DCE. When measuring Mn(^{H}bpy) in DCE we were not able to capture the 13 additional x-ray pulses before the next pump pulse. The change in the pre-edge signal is shown in the inset with an arrow to denote the direction of change. To the the right of each TR-XAS figure is the difference spectrum at each time delay, which is calculated by subtracting the ground-state XAS spectrum from the TR-XAS. We include the evolution of the TR-XAS difference signal at 6.55 keV in the inset with a fit using a single exponential decay convoluted with a Gaussian response function. In the case of Mn(^{H}bpy) in MeCN the K-edge shifts by $\sim$3 eV to lower energy at early

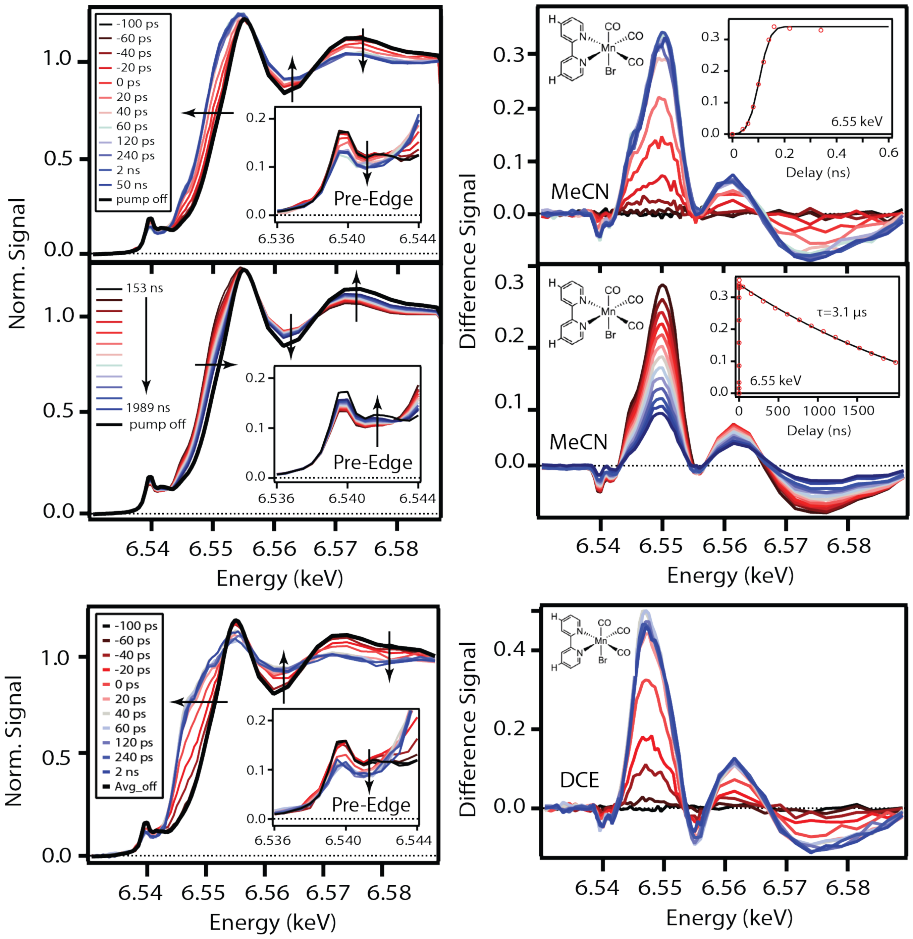

Figure 6.5: TR-XAS for the Mn(^{H}bpy) tricarbonyl complex in acetonitrile during the first 50 ns shown in the top left panel, with difference spectrum to the right. Middle panel is the continuation of the TR-XAS for Mn(^{H}bpy) complex on the ns timescale with difference spectrum to the right. TR-XAS for the Mn(^{H}bpy) complex in DCE is shown in the bottom panel with difference spectrum to the right.

delay times, indicating an increase of electron density on the Mn. The edge shifts back to higher energy with a 3.1 μs lifetime. The edge shift results in a strong positive signal at $\sim$6.550 keV in the difference spectrum, with a small shoulder at lower energy. The small shoulder decreases in strength relative to the peak at 6.550 keV over the first 50 ns. Additionally, the edge shift is accompanied by changes in the XANES region above the edge, which become more pronounced again on the μs timescale. The difference signal decrease on the μs timescale for Mn(^{H}bpy) in MeCN, however complete recovery back to the the baseline is not expected due to the formation of photodecomposition products. The pre-edge feature is a forbidden 1s $\rightarrow$ 3d transition caused

by the d orbitals mixing with the Mn p-orbitals.[228] At early times the pre-edge feature initially decreases in signal strength without any evidence of shifting, before recovering signal strength on the μs timescale. The transient spectrum for Mn(^{H}bpy) in DCE has a similar shift of the K-edge to lower energy at early delay times, however the energy shift of $\sim$6 eV is twice the shift in energy compared to Mn(^{H}bpy) in MeCN. In DCE the pre-edge feature for Mn(^{H}bpy) decreases in absorption strength, similar to Mn(^{H}bpy) in the MeCN solvent.

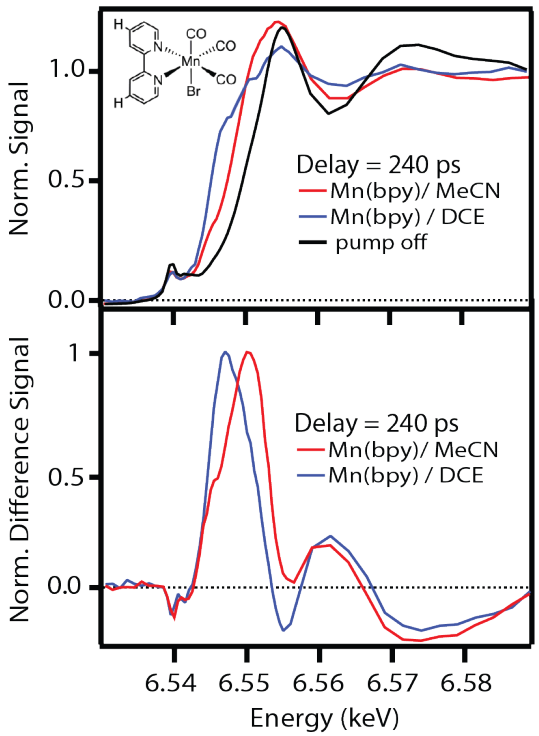

Figure 6.6: Ground-state Mn(^{H}bpy) XAS in black with the TR-XAS at 240 ps for the Mn(^{H}bpy) complex in MeCN and DCE, bottom panel shows the difference spectrum for the Mn)bpy complex in the respective solvents.

To highlight the different spectra in the two solvents, figure 6.6 compares the ground-state x-ray spectrum of Mn(^{H}bpy) with the transient and difference spectra at a delay of 240 ps for the Mn(^{H}bpy) complex in MeCN and DCE. In the transient spectrum the Mn(^{H}bpy) complex in DCE has a larger edge shift of 6 eV to lower energy as well as a greater reduction in the fine structure after the edge compared to Mn(^{H}bpy) in MeCN. The variation in the transient spectrum for Mn(^{H}bpy) in the two solvent environments translate to difference spectra with the largest difference at $\sim$6.550 keV shifted to lower energy of 6.548 eV for Mn(^{H}bpy) in DCE. The difference spectrum

has a peak intensity is at 6.548 keV, which is 3 eV lower than Mn(^{H}bpy) in MeCN. Additionally, the strong difference signal does not have a lower energy shoulder. The difference spectrum for Mn(^{H}bpy) in DCE also appears to overlap the small shoulder of the Mn(byp) difference signal in MeCN.

6.3.2 TR-XAS for Mn(^{L}bpy)

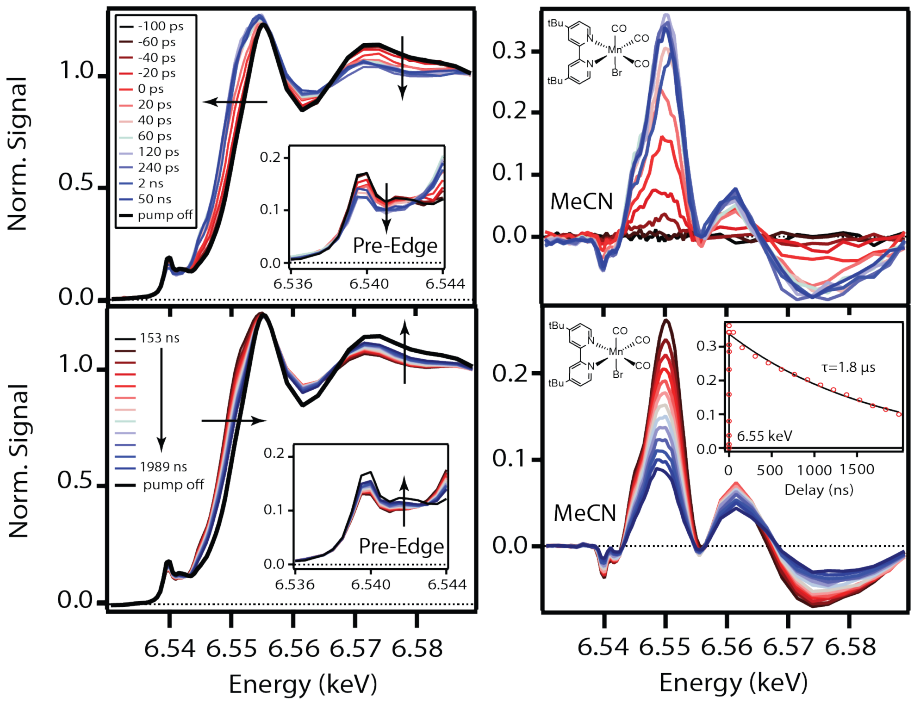

Figure 6.7: TR-XAS for the Mn(^{tBu}bpy) tricarbonyl complex in MeCN is shown on the left, with difference spectrum to the right.

Figures 6.7, 6.8 and 6.9 show the TR-XAS for Mn(^{tBu}bpy), Mn(^{CF_3}bpy) and Mn(^{NO_2}bpy), respectively, in MeCN. The evolution of the spectra for Mn(^{tBu}bpy) and Mn(^{CF_3}bpy) have similar 3 eV edge shifts to lower energy and reduced oscillations above the edge as the Mn(^{H}bpy) compound. We fit the decay of the difference signal to a single exponential convoluted with a response function to yield lifetimes of 1.8 and 3.4 μs, compared with the 3.1 μs lifetime for Mn(^{H}bpy).

Of the four compounds Mn(^{NO_2}bpy) has the most substantial differences in the TR-XAS spectrum and the longest lifetime. Figure 6.9 shows the evolution of the transient spectrum for the

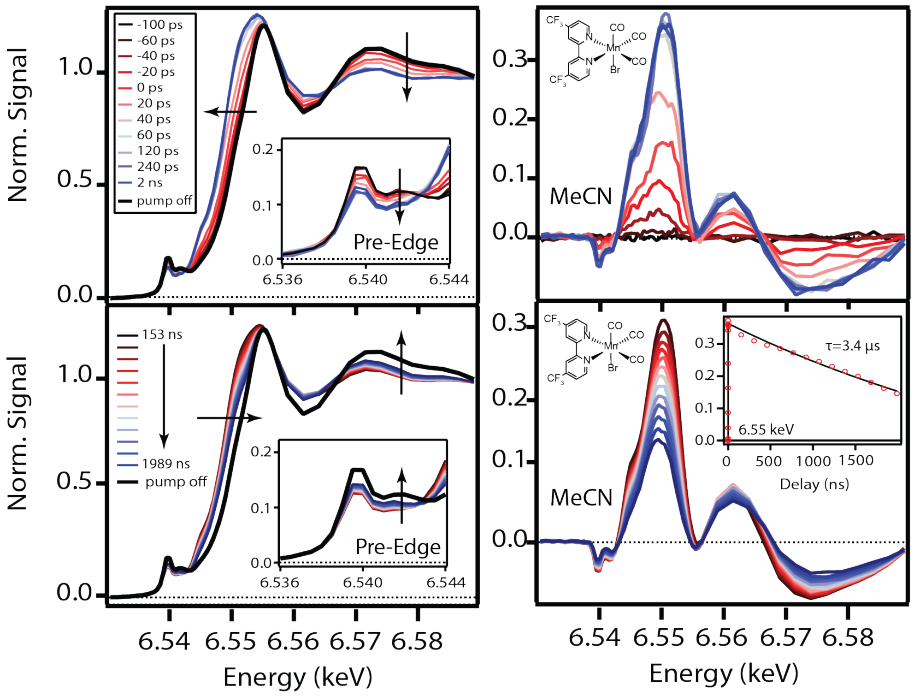

Figure 6.8: TR-XAS for the Mn(^{CF_3}bpy) tricarbonyl complex in MeCN shown in the top group of 4 panels, with difference spectrum to the right.

Mn(^{NO_2}bpy) complex in MeCN after MLCT excitation at 532 nm in the top panel with the difference spectrum to the right. The lower panels show the TR-XAS and difference signal on hundreds of ns timescale. The transient spectrum for Mn(^{NO_2}bpy) has a different K-edge, as well as oscillations after the edge, which points to a different structure for the scattering atoms. Although the edge shifting to lower energy and the weakening of the post edge oscillations is similar to the other Mn(^{L}bpy) compounds, the evolution on the ns timescale is significantly different. From 153 ns to 1989 ns the TR-XAS for Mn(^{NO_2}bpy) complex recovers more slowly compared to the other Mn(^{L}bpy) compounds. The slow recovery is most notable in the difference signal, where the amplitude at 6.550 keV decreases only slightly over the 2 μs delay range. Additionally, the decrease in the difference amplitude could be due the sample flowing out the the x-ray path, or relaxation The shoulder at 6.545 keV also disappears on the 2μs.

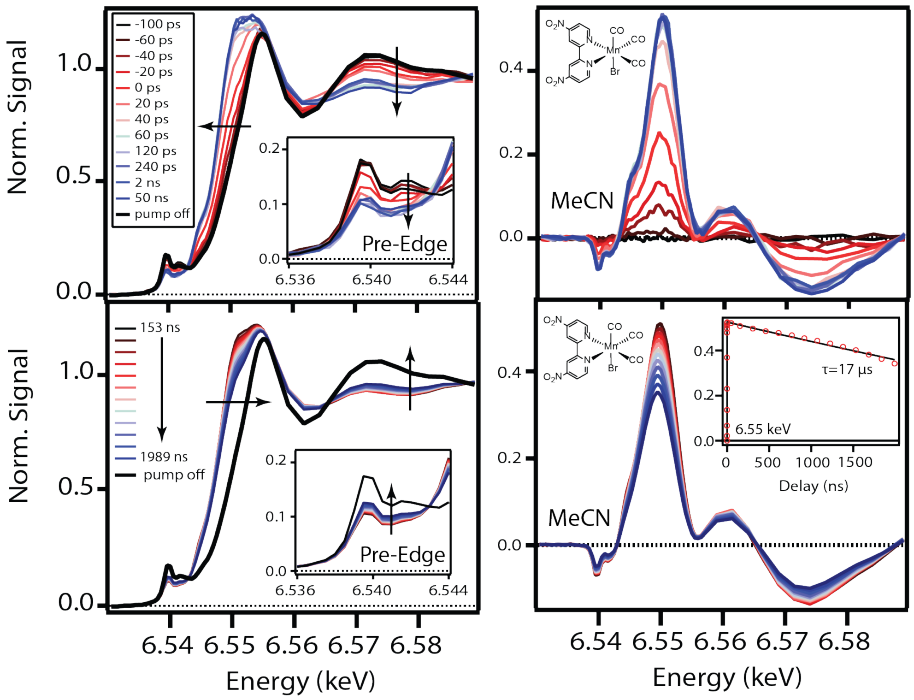

Figure 6.9: TR-XAS for the Mn(^{NO_2}bpy) tricarbonyl complex in MeCN during the first 50 ns shown in the top left panel, with difference spectrum to the right. Middle panel is the continuation of the TR-XAS for Mn(^{NO_2}bpy) complex on the ns timescale with difference spectrum to the right.

6.4 Discussion

The K-edge energy is related the oxidation state and how much electron density is on the Mn center, which is directly affected by the identity bound ligands. For the Mn(^{L}bpy) complexes, the ground-state energy of the K-edge is 6.551 keV in the starting complex, which is significantly higher in energy compared to most formal Mn^{I} complexes. The increased K-edge energy better matches a formal Mn^{III} such as Mn_2O_3 and is due to the strong π-backbonding from the CO ligands, which pull electron density away from the Mn atom.[227–229] The bromide ligand in the complex acts as an electron donor, which contributes to the electron density on the Mn center through mostly σ donation, with an increase in π donation when along p_x or p_y axes. However the electron density contribution from the bromide ligand is minimal compared to the withdrawing nature of the 3 CO ligands. This points out that even in the XAS for the Mn(CO)$_3$(^{L_2}bpy)Br complexes, the CO ligands have a substantial effect on the K-edge energy and is consistant across the series of complexes.

Figure 6.10 displays the photodecomposition mechanism for Mn(CO)$_3$(^{L_2}bpy)Br (L = tBu, H,

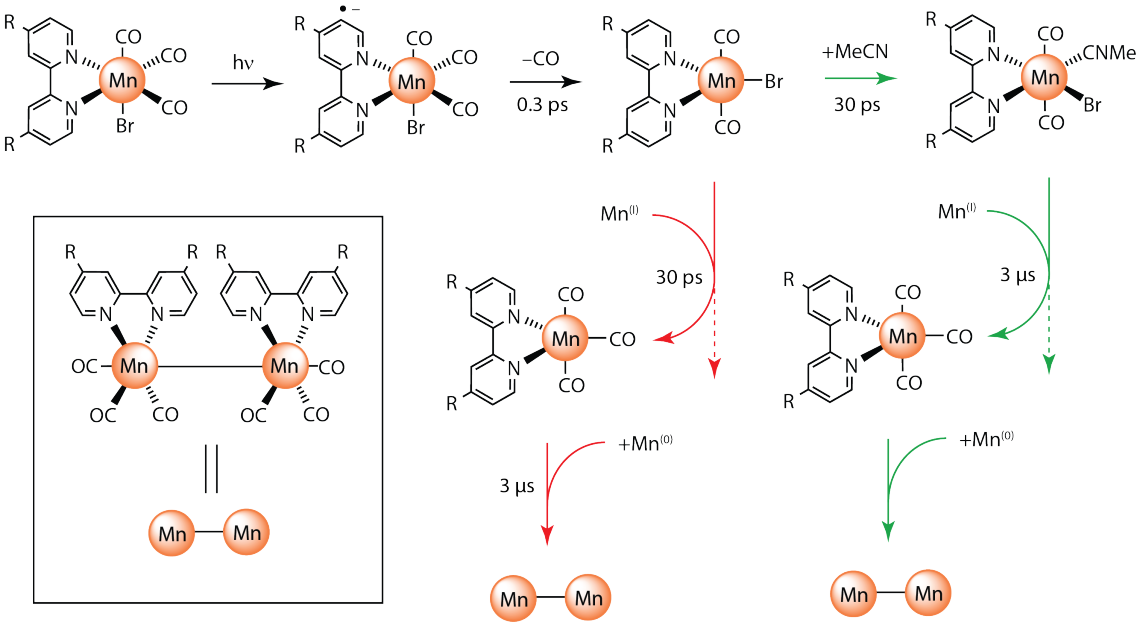

Figure 6.10: Photodecomposition mechanism for $Mn(CO)_3(^{L_2}bpy)Br$ (L = tBu, H, CF_3) complexes after MLCT excitation, red and green arrows show the two competing pathways.

CF_3) complexes after MLCT excitation, with the red and green arrows denoting competing reaction pathways. Due to the x-ray probe pulse duration of ∼80 ps, resolving transient $Mn(^{L}bpy)$ species before the BET is not possible. Following the BET for $Mn(^{tBu}bpy)$, $Mn(^{H}bpy)$ and $Mn(^{CF_3}bpy)$, an equatorial CO ligand dissociates from the Mn center concerted with ligand reorganization within 0.3 ps. After relaxation/ligand reorganization an electron deficient 5-coordinate $Mn(^{L}bpy)$ species exists for tens of ps before reacting via two possibly competing mechanisms. In the pathway with green arrows, a nearby coordinating solvent molecule such as MeCN binds to the Mn center on the tens of ps timescale to form a more stable 6-coordinate $Mn(^{L}bpy)$-MeCN complex with the bromide equatorial and two CO ligands in the axial position. Being a better reducing agent, the $Mn(^{L}bpy)$-MeCN species goes on to reduce the starting $Mn(CO)_3(^{L_2}bpy)Br$ complex on a 3 μs timescale to a Mn^0 ($Mn(CO)_3(^{L_2}bpy)$) complex. The Mn^0 species then forms a dimer with another Mn^0 species on a timescale outside of our measurement range. Alternatively, in the pathway with red arrows the 5-coordinate species reduces the starting $Mn(CO)_3(^{L_2}bpy)Br$ complex to a Mn^0 species on the tens of ps timescales, which then dimerizes with a second Mn^0 species on the 3 μs

timescale.

In the TR-XAS, the K-edge shifts to lower energy for Mn(^{tBu}bpy), Mn(^{H}bpy) and Mn(^{CF_3}bpy) in MeCN due to the Mn center becoming more electron rich. The K-edge shift is constant with the reorganization of the ligands after CO loss, which has already been shown to be sensitive to the CO ligands in the ground-state XAS. The reorientation of the ligands suggests that when MeCN bonds to the Mn metal, the CO ligand will move to the axial position and the bromide ligand to an equatorial position. With the axial CO ligands *trans* to each other the π-backbonding of the two axial CO ligands competes for electron density from the Mn center, which results in more electron density remaining on the Mn center. The weakly bound MeCN molecule to the Mn center does not strongly change the electron density on the Mn center and therefore virtually does not effect the K-edge.

The other possible pathway for the decomposition reaction is for the 5-coordinate species to reduce the starting Mn^I species to Mn^0, which involves the loss of a bromide. With the bromide ligand removed from the Mn center, the 3 CO ligands relax to form a distorted trigonal bipyramidal structure.[230] Due to the distorted structure having poor overlap for π-backbonding, more electron density would reside on the Mn center causing the K-edge to shift to lower energy. For Mn(^{H}bpy) in DCE we suppress solvent coordination to the Mn center, therefore the TR-XAS at 240 ps is either the 5-coordinate complex or the Mn^0 species. Additionally, the K-edge in the TR-XAS has a 6 eV shift to lower energy. The larger edge shift is inconsistent for the 5-coordinate species to reduce the Mn^I to Mn^0 because the Mn^0 has 3 CO ligands involved in π-backbonding compared to the 5-coordinate species which has a bromide and 2 CO ligands. Both the 5-coordinate and Mn^0 have a similar distorted trigonal bipyramidal like structure, which reduces the electron density involved in the CO ligand π-backbonding, but the bromide is a σ-donor of electron density. Therefore, the 6 eV edge shift for Mn(^{H}bpy) in DCE is due to the two weakened π-backbonded CO ligands and the σ-donor which increase the electron density on the Mn center more than the three weakened π-backbonded CO ligands of the Mn^0 species.

6.4.1 Shifting of the K-edge

The K-edge for Mn(^{tBu}bpy), Mn(^{H}bpy) and Mn(^{CF_3}bpy) in MeCN shifts to higher energy on the μs timescale. The shift indicates that the Mn center is losing electron density, through a bimolecular mechanism. As previously described, the Mn(^{L}bpy)-MeCN complex reduces the Mn^{I} complex to form a formally Mn^0 species with a distorted trigonal bipyramidal structure. During the reduction of Mn^{I} the Mn(^{L}bpy)-MeCN complex is oxidized to Mn^{II}, which is unstable and decomposes. For the distorted trigonal bipyramidal structure of Mn^0, the CO ligands have poor overlap for π-backbonding resulting in more electron density on the Mn center, however without the bromide ligand the net electron density on the Mn center presumably decreases causing the K-edge to shift to higher energy. In the competing reaction, the Mn^0 complex is already present in the solution, which will react with another Mn^0 complex to form a Mn-Mn dimer. However, an investigation into the XAS for the $Mn_2(CO)_{10}$ dimer and the $Mn(CO)_5$ show no change in the K-edge energy.[228] The results from the $Mn_2(CO)_{10}$ contradict the observed K-edge shift to higher edge energy in our TR-XAS, which again support the Mn(^{L}bpy)-MeCN complex mechanism.

In the case of the stronger electron withdrawing -NO_2 groups on the bpy ligand, BET from the MLCT state occurs but does not facilitate the loss of a CO ligand, therefore this compound requires a different explanation for the 3 eV shift in the TR-XAS. After exciting the MLCT, the electron is stabilized on the bpy ligand by the -NO_2 groups. While the electron is stabilized on the bpy, the π-backbonding for the equatorial CO is weakened at the same time as the Mn-Br σ bond is strengthened. The lengthening CO bond allows the bromide ligand to begin moving toward the equatorial position. The BET puts the electron back into the original d-orbital from which it was excited, thereby strengthening the Mn-CO bond and weakening the Mn-Br bond, which allows the bromide to move to the equatorial and the CO to the axial positions.[231,232] The ligand rearrangement with CO ligands in the axial position cause the K-edge in the XAS to shift to lower energy. After the ligand rearrangement of the Mn(^{NO_2}bpy) species the K-edge does not shift back to higher energy, suggesting the electron density on the Mn center remains unchanged. However, near the top of the K-edge a small change in the TR-XAS signal occurs on the μs timescale.

6.4.2 Intensity of the Pre-edge

Across the series of Mn(^{L}bpy) compounds in MeCN the pre-edge feature shows a fairly consistent decrease in signal intensity. The pre-edge feature is a dipole-forbidden 1s $\rightarrow$ 3d transition allowed by mixing of the 3d and 4p orbitals, which depends on the symmetry around the Mn center. Quadrupole transitions can also contribute to the pre-edge intensity, but are significantly weaker compared to the transition from mixed d-p orbitals, therefore changes in quadrupole intensities are not considered for the pre-edge signal decrease. From the ground-state XAS, the pre-edges features have nearly identical intensities for all the compounds, because the same symmetry around the Mn center. However, as described in the above paragraphs, ligand rearrangement occurs with the axial bromide trading places with an equatorial CO ligand. With the CO ligands in the axial position the molecule has more centrosymmetry character compared to the ligand arrangement with the CO and Br ligands in the axial position, which decreases the pre-edge intensity. Additionally, the unoccupied d orbitals responsible for the transition depend on the identity of the two axial ligands and the migration of the electron donating bromide to an electron accepting CO has a large effect on the pre-edge intensity. On the μs time scale for Mn(^{tBu}bpy), Mn(^{H}bpy) and Mn(^{CF_3}bpy) we see the pre-edge signal intensity increase due the loss of the centrosymmetry. The increase in the pre-edge intensity is consistent with the Mn(^{L}bpy)-MeCN species reducing the Mn^{I} complex to form the Mn^{0} species, which results in decrease of the more centrosymmetric molecules. Additionally, dimer formation is inconsistent with the increasing pre-edge for the same reason that the K-edge does not describe dimer formation. The investigation into the XAS for the $Mn_2(CO)_{10}$ dimer and the $Mn(CO)_5$ do not have different pre-edge intensities.[228]

6.4.3 Fine-structure

The oscillation pattern above the rising edge is due to scattering of the outgoing electron from nearby atoms. The fine structure reagion of the XAS is much more sensitive to the structure of the Mn(^{L}bpy) complex. Shortly after exciting the MLCT the oscillations decrease compared to the ground-state XAS. Unfortunately, the x-ray probe is not sensitive to only the optically excited

Mn(^{L}bpy) species, therefore the TR-XAS contains some ground-state signal as well the excited Mn(^{L}bpy) species. Not only is the XAS shifted for the two Mn(^{L}bpy) species but the scattering atoms have different bond lengths which mean the two overlapping XAS cancel out to produce the weakened oscillation. As for the two possible decomposition mechanisms, the decrease in oscillations seems to be more sensitive to the structure of the ligands because the Mn(^{NO_2}bpy), which does not lose a CO ligand, has a decrease in oscillations. However, the complexity of the decomposition makes interpreting the change in oscillations difficult without having higher resolution XAS of the fine structure region. Measuring the EXAFS and modeling would provide a significantly higher degree of detail about the structure and bond distances for the various species and reactions in the photodecomposition of Mn(^{L}bpy).

6.5 Conclusion

Using TR-XAS we examine the photodecomposition reaction for a series of Mn(^{L}bpy) compounds, which provide structural information out to 2 μs in delay time. After exciting the MLCT band in the ground-state, the Mn(^{tBu}bpy), Mn(^{H}bpy) and Mn(^{CF_3}bpy) compounds release a CO ligand after the BET from the bpy ligand, where as Mn(^{NO_2}bpy) does not show any ligand dissociation. In place of the lost CO ligand, the MeCN solvent will bind to the Mn metal center, however the solvent to metal coordination can be suppressed using DCE. For all the compounds in acetonitrile after MLCT excitation the TR-XAS show a 3 eV shift to lower energy due to ligand rearrangement involving the axial bromide and an equatorial CO ligand. The rearrangement also causes changes in the post-edge oscillations and pre-edge features. On the μs timescale we see evolution the TR-XAS K-edge back to higher energy with an increase in pre-edge intensity suggesting the formation of a Mn-Mn dimer species. The information gathered in this chapter provides the framework for future investigations into the photodecomposition reaction for the Mn(^{L}bpy) compounds.

Chapter 7

Probing the Plasmonic Near-Field Enhancement of a Gold Nanorod Array

7.1 Introduction

In recent years nanoplasmonics have acquired greater interest from the science community predominantly due to their adaptation into multiple fields of chemistry research.[78,233] A few of the applications using surface plasmons include surface enhanced Raman spectroscopy (SERS) for low signal detection,[81,82] light harvesting solar cells to boost the conversion efficiency,[83–85] and driving photochemical reactions under low light conditions.[86–89] All of these applications are made possible when the electron density in subwavelength sized gold nanoparticles respond to a specific frequency of electromagnetic radiation. The electron density oscillates with the electric field and are called surface plasmons.[81,234]

The surface plasmons continue to oscillate at the frequency of the incident electric field and at maximum displacement from equilibrium very intense electric fields are produced near the surface of the gold nanoparticle.[79] The emphasis of this chapter will be on investigating the enhanced electric field mechanism for energy transfer in the near-field between the gold nanorod and the surrounding medium, which will help to elucidate the fundamental of the plasmonic system. However, competing energy relaxation mechanisms such as thermal heating and electron transfer also contribute in energy transfer to the surrounding medium.[90] The thermal heating mechanism progresses when the surface plasmons relax through internal electron-phonon interactions, which produces thermal energy that diffuses into the surrounding medium.[91] Electron transfer from the nanorod

into the surrounding medium occurs when the absorption of a photon promotes a free electron to a higher energy level which relax through electron-electron scattering. During this time the energy is redistributed and the energetic electron can be transferred from the metal to the nearby surrounding medium through orbital mixing.[90] It is important to consider all the possible energy transfer pathways into the surrounding medium, so chemical reactions in the enhanced near-field can be explicitly understood.

A ground breaking experiment by Tsuboi and coworkers showed enhanced plasmonic fields inducing a two-photon photochromic reaction using an 808nm continuous wave (CW) laser for excitation.[86] A very common photochromic diarylethene derivative (DAE) was deposited over randomly distributed spherical gold nanoparticles on a glass substrate. DAE was chosen for its thermal stability[235] and well documented photosiomerization reaction[236,237].

The open-ring isomer is converted through the ring-closing reaction to form the closed-ring isomer using UV excitation below 350nm. The closed-ring isomer has a characteristic visible absorption spectrum at 600 nm, which can be easily excited into, thereby initiating the ring-opening reaction. The absorption band in the visible spectrum was used to monitor the photochromic reaction progress.[86,235] During their investigation Tsuboi concluded the electric field enhancement between adjacent gold nanospheres was strong enough in the near-field to drive the photoisomerization reaction via non-resonant two-photon excitation from the 808nm CW laser source, based on having a quadratic power-dependence for the change in absorbance after 15 minutes.[86] Other similar approaches to investigating nanoplasmonics have included photochromic switching in solid and solution phase[87,88,92,93] attaching molecules directly to the nanoparticle[89,94–97] and structurally changing the size and shape of the nanoparticles to alter the enhanced field.[98–101]

In order to manipulate the use of nanoplasmonics for conducting chemistry in the near-field a more detailed understanding about the interactions and mechanisms is needed. To further examine the mechanism of nanoplasmonic field-enhanced reactions of DAE, we describe in this chapter switching on an array of periodically spaced gold nanorods on a glass substrate. The regularity of the plasmonic array provides a well-defined substrate to convert the DAE thin film as well as a con-

sistent electric field enhancement across the array compared with randomly placed nanospheres. The aligned array also allows the enhancement to be tuned based on incident field polarization with respect to orientation of the aligned nanorods. To convert DAE we use 800 nm pulsed femtosecond laser irradiation. Under the pulsed conditions the two-photon excitation (2PE) process is favored over one-photon excitation (1PE). To support the experimental results and gain a more detailed understanding of how the photochromic reaction progresses in the plasmonic system, the change of absorption due to conversion of DAE was simulated using a simple model. The model calculates the change in absorption based on calculated near-field intensities of the 800 nm and probe light by solving the solutions to the Maxwell equations. Polarization anisotropy is included in the simulation to account for the subtle angle differences in the near-field vectors around the nanorod for the 800 nm and probe light, even though their incident polarization is identical. The model only accounts for electric field interactions with molecules in the near-field of the nanorod array, and gives excellent agreement with the experimental results.

7.2 Materials and Methods

We use a plasmonic array of gold nanorods that was described previously as a substrate for femtosecond-switching of electron diffraction.[238] The array was fabricated using electron-beam lithography and consists of regularly spaced gold nanorods on a glass substrate. Each nanorod is approximately 170 nm long by 80 nm wide, with a 10-20 nm gap between the tips of the nanorods along their long axis and a spacing of approximately 80nm between rows. The entire array is 100 μm x 100 μm. The array is designed to have a plasmonic resonance at 800 nm for polarization along the long axis of the nanorods.[238] Before each measurement, the array is placed in hexanes for cleaning and to remove any foreign substances. After drying with nitrogen, 10 μl of DAE dissolved in hexanes is pipetted onto the surface and allowed to dry leaving a thin film of DAE molecules on the plasmonic array. For comparison, a thin film of DAE on only a glass substrate is prepared using the same technique for measurements in the absence of the gold nanorods. The thickness of a typical film on glass was measured to be 60nm using ellipsometry. The film is formed with

DAE in the open-ring structure, where it is then irradiated with a 310nm LED (Thorlabs, 40 mW) until photo-stationary state (PSS) is reached. PSS is achieved when the concentrations of DAE in both the open and closed-ring structures remains constant, identifiable by the absorption spectrum remaining the same after additional 310nm irradiation. A film with a thickness of 60nm equates to an approximate absorbance value of 0.10 at 580 nm.

We used pulsed laser irradiation to convert the DAE to the open isomer and to measure the transmission. An amplified Ti:sapphire laser (Legend Elite; Coherent) produces 35 fs laser pulses with a center wavelength of 800 nm and 1 kHz repetition rate. We use the optical transmission of white light continuum laser pulses obtained by focusing the 800 nm fundamental into a cuvette of water to generate white light continuum for the probe light, to monitor the number of molecules in the closed-ring isomer. The white light probe is split with a 50% beam splitter into a signal and a reference beam. The signal beam is focused down to 60 μm at the point where it passes through the plasmonic array. The reference beam accounts for fluctuations of the incident probe intensity when calculating the absorption of the DAE sample. After the sample, the broadband signal and reference beams are dispersed using a transmission grating onto an 8 bit CMOS camera (Thorlabs), with dimensions of 1280 x 1024 pixels to calculate normalized intensity/absorption as a function of wavelength over the range 400-650nm. The exposure of the sample to the white light probe beam was limited to less than one second per absorption measurement using mechanical shutters in order to minimize resonant photoswitching by the weak probe field. Under these conditions, photochromic switching of the molecule in the film due to the probe light was negligible for all measurements. To probe the electric field enhancement we use the fundamental 800 nm for non-resonant excitation of the photoswitch in the closed form, and measure the change in transmission of the visible probe light due to photochromic switching to the open form. A beam diameter of 0.6 mm at the sample ensures an even distribution across the entire array, and we use a variable neutral density filter to set the incident intensity of 6, 30 and 60 GW/cm2. The exposure time is controlled by a mechanical shutter. When the measurement is completed, UV irradiation converts DAE back to the initial photo-stationary state. We observe complete recovery, ensuring that only

the reversible, cycloreversion reaction took place and that no damage occurred to the sample during the experiment.

The enhancement of the electric field relative to the incident field for the 800 nm and 580 nm probe exposure is calculated for a unit cell with dimensions of 110nm x 195nm that contains a single gold nanorod. The software package COMSOL Multiphysics solves the Maxwell's equations in frequency domain and accurately calculates how a nanostructure will interact with incident electromagnetic radiation. Periodic boundary conditions were used account for interactions between the nanorods. The calculated field is used to simulate the absorbance decay for the photoswitch on the plasmonic array.

7.3 Results and Analysis

7.3.1 One and Two-Photon Photochromism

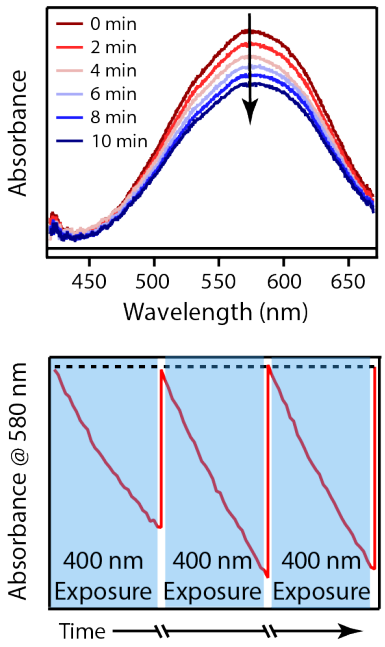

Figure 7.1: Top panel shows the decreasing ground-state absorption for the cDAE isomer thin film on a glass substrate after resonant 400 nm exposure. In the bottom panel, cyclization of the absorption at 580 nm shows the cDAE isomer converting to the oDAE isomer under 400 nm exposure and then back to the cDAE isomer under 310 nm UV irradiation.

The top panel in figure 7.1 shows the decreasing ground-state absorption for the cDAE isomer thin film deposited on a glass substrate after incrementing the duration of resonant 400 nm exposure. The decreasing absorption band is due to the conversion from the cDAE to oDAE isomer, which does not absorb in the visible wavelength range. After conversion to the oDAE isomer, the sample is converted back to the cDAE isomer using a 310 nm UV LED, and is shown in the bottom panel with 3 cyclization intervals where the absorption at 580 nm returns to the starting absorption. The recovery of the absorbance at 580 nm indicates efficient cyclization along with no evidence for damage to the sample, even after several irradiation cycles. Although the DAE molecules are in the solid phase, the spectroscopy behavior matches that for DAE in solution.[236,239]

The cDAE isomer absorbance at 800 nm is very weak and is easily overlooked as a possible excitation wavelength. To estimate the absorbance at 800 nm we use the Urbach tail approximation, which describes the decay of the absorbance tail as an exponential decay.[240] From the exponential fit to the tail of the absorption band yields an absorbance at 800 nm on the order of 10^{-4} compared with the maximum absorbance of 0.10 at 580 nm. Using an 800 nm continuous-wave laser with an intensity of 3 watts/cm^2 yields a 3.2% conversion to the oDAE isomer after 15 minutes, indicating the cycloreversion reaction can be initiated via one-photon at 800 nm. The one-photon excitation process for initiating the cycloreversion reaction is a first order process, and the rate of conversion increases linearly with increasing the excitation intensity. However, the cycloreversion reaction can also be initiated via two-photon excitation, which requires very high peak intensities on the order of GW/cm^2.

Figure 7.2 shows the ground-state absorption decreasing for cDAE over 40 minutes with exposure to high intensity 800 nm laser light, which drive a two-photon excitation process. The decrease in absorption is due to the cycloreversion reaction converting the cDAE to oDAE isomer. The nonlinear excitation process increases the rate of the cycloreversion reaction, which goes as the square of the intensity, and becomes more dominant at high intensities compared to the one-photo excitation process. To show how changing the intensity of the 800 nm laser light changes the conversion rate, the bottom panel in 7.2 shows the normalized absorbance decay at 580 nm

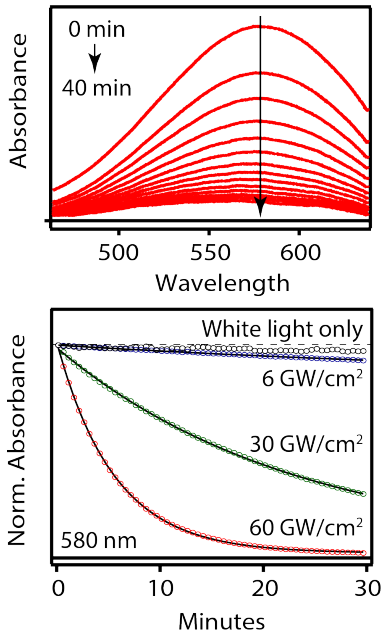

Figure 7.2: Ground-state absorption of cDAE thin film on a glass substrate after non-resonant pulsed 800 nm exposure, with the bottom panel showing the aborbance decay at 580 nm for different laser intensities.

for three different intensities with an exponential fit as the solid black line. Additionally, we show that the white light probe is not contributing substantially to the absorption change, which remains nearly constant for 30 minutes in the absence 800 nm exposure. Using the rates from the exponential fits, we measure the power dependence of the excitation process to be 1.8, which indicates a dominant two-photon process.

7.3.2 Photochromism in the Near-Field of Nano-Plasmonic Array

To monitor the two-photon activated cycloreversion reaction we use the cDAE isomer absorption band, due to the clear distinction in spectroscopy between the two isomers. Figure 7.3 has the cDAE isomer absorption on the plasmonic array (black) and on the glass substrate (red) to show that no changes to the spectrum are caused due to the different environment. Both spectral bands have an absorbance band centered near 580 nm with subtle differences due to variations of film thickness and beam distortion due to transmission through imperfect film. The green line at the baseline shows the oDAE isomer on the plasmonic array does not absorb in the in the wavelength

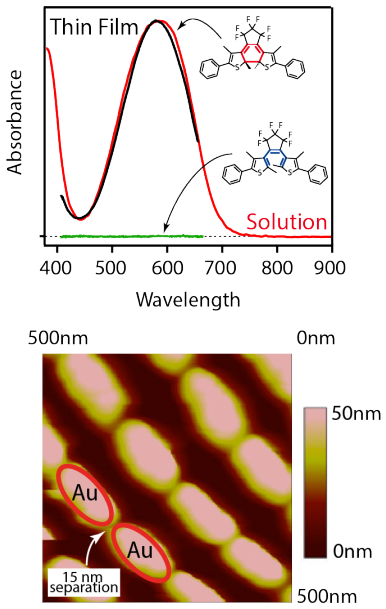

Figure 7.3: Top panel shows the absorption spectrum for the cDAE isomer on the plasmonic array (black) and the glass substrate (red) for comparison. The oDAE does not absorb in the wavelength range evident by the flat absorption shown in green. The bottom panel is the atomic force microscopy image for a portion of the plasmoic array.

range, therefore any change in the cDAE absorption is due to conversion to the oDAE isomer. In the bottom panel of figure 7.3 an atomic force microscopy image for a small portion of the plasmonic array is displayed, and shows the patterned array and some of the imperfections that exist such as size and shape. Although the image appears to have the gold nanorods touching, they are in fact separated by $\sim$15 nm, as shown in previous SEM microscopy images.[238]

The direct comparison between the reaction rate of the cDAE isomer on glass and the array is made in figure 7.4, which shows the rate of decay to be initially faster for the plasmonic array substrate. Both measurements are conducted at the same incident intensity of 60 GW/cm^2. The faster decay for the photoswitch on the plasmonic array is due to the higher electric fields around the nanorod. Importantly, a single exponential describes the decay of the photoswitch on the glass substrate, but the decay of the photoswitch on the array requires at least a bi-exponential curve to adequately fit the data. We ascribe no physical meaning to the two components of the bi-exponential fit, except to indicate more than one switching rate contributes to the absorbance change. The calculated enhancement (E/E^0) to the incident field is displayed in bottom panel

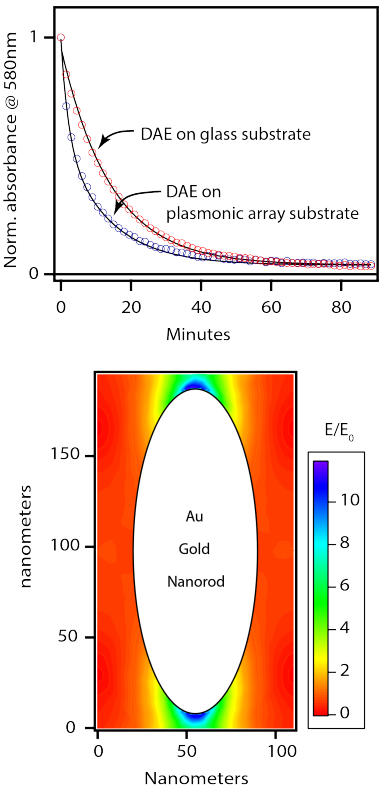

Figure 7.4: Absorbance at 580 nm with DAE on glass substrate (red) and plasmonic array (blue), exponential and bi-exponential fits (solid lines) are applied respectively. Irradiation intensity is 60 GW/cm2. Bottom panel show the calculated relative electric field enhancement to the incident field.

of figure 7.4 for a single nanorod, which has a maximum enhancement located at the tips and a minimum at the sides of the nanorod for incident 800 nm polarization along the long axis of the nanorod. This is only a 2D cut through the nanorod where the maximum enhancement occurs. The distribution of intensities around the nanorods creates a spatial dependence which is why molecules near the tips will convert DAE to the open-ring structure of DAE faster, eventually bleaching that area before others. This distribution also explains why the absorption decay in figure 7.4 is unable to be fit to a single exponential. The reaction is observed to proceed very quickly at the tips of the nanorod where the electric field is the strongest, but the weaker field at the sides of the nanorod convert molecules at a slower rate. A distribution of rates is therefore observed in the measurement and so the decay rate is an average of all the different rates around the nanorods, yielding bi-exponential behavior for the absorption decay.

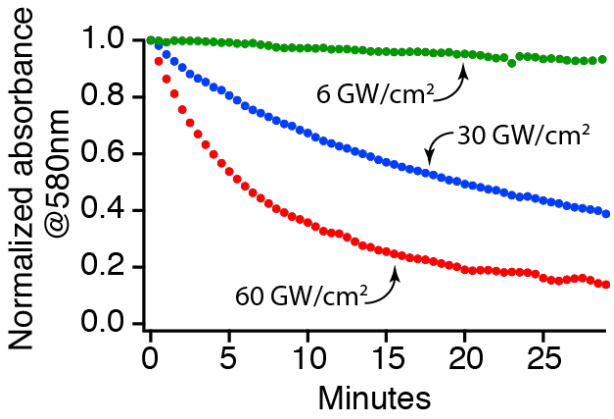

Figure 7.5: Measured absorbance decay of DAE on the plasmonic array at 580 nm for pulse energies of 1, 5, and 10 μJ/pulse which correspond to intensities of 6, 30, and 60 GW/cm^2.

Figure 7.5 shows the absorption decay at 580 nm for the DAE film on the array with 800 nm intensities of 6, 30 and 60 GW/cm^2. The initial rate of decay has the same quadratic power dependence as DAE on the glass substrate, indicating a dominating two-photon process. To emphasize the depletion relative to the incident field at the sides of the nanorods, the polarization of the probe was rotated by 90° with respect to the 800 nm polarization, which remains aligned along the long axis of the nanorod. Changing the incident polarization of the probe changes the near-field by giving an enhancement of the probe field at the sides of the nanorod, where the conversion of molecules due to vertically polarized 800 nm field is reduced.

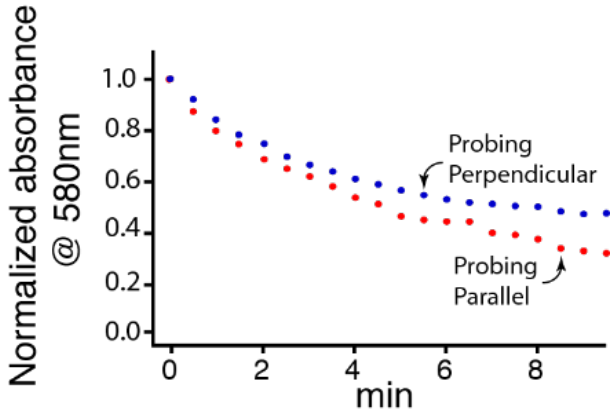

Figure 7.6: Absorption decay for DAE thin film on the plasmonic array while probing parallel and perpendicular.

The absorption signal decays faster when the probe has parallel incident polarization compared

with a probe that has been rotated to be perpendicular to the 800 nm polarized field, shown in figure 7.6. The difference in conversion for the two experimental decays is entirely due to different spatial probing profiles. When probing parallel the enhanced electric field profile is similar to the pump, with the strongest fields at the tips. However, when the probing field is rotated to be perpendicular the enhancement to the incident field is maximized on the sides of the nanorod where most of the closed-ring DAE molecules remain. This makes the probe more sensitive to those molecules on the sides of the nanorod yielding an absorbance with less change after 10 minutes.

7.3.3 Simulating the Absorption Decay of DAE on Glass

We simulate the absorbance decay of DAE using a transmission equation that takes into account both one and two-photon excitation at 800 nm. We calculate the change of intensity of the probe light ΔI,

$$\Delta I = N I_0 \Delta z (\phi_{1PA} + \frac{\phi_{2PA}}{h\nu} I_0) \tag{7.1}$$

based on the initial intensity I_0, N is the number density for molecules in the closed-ring isomer, Δz is the apparent film thickness (60 nm), ϕ_{1PA} and ϕ_{2PA} are the one and two-photon absorption cross sections at 800 nm, respectively. The change in intensity of transmitted light is converted into the change in molecules in the closed-ring isomer using a quantum yield of 2%.[184,235,236,241] The quantum yield expresses the number of molecules that get converted per excitation event, regardless of one or two-photon absorption. In order to accurately reproduce the change in absorption in the limit of a fully bleach sample, we calculate the change of molecules after 10 ms of 800 nm exposure.

With both the small absorbance at 800 nm and the film thickness (60 nm), the one-photon cross section at 800 nm is calculated using basic equations for a sample's absorbance of light and yields a value of $1x10^{-22} \frac{cm^2}{molecule}$. The two-photon cross section is the only undefined value and is used as a fitting parameter for simulating the high intensity absorbance decays. The two-photon cross section is determined to be 5.5 GM. This value is within the range of other experimentally

determined two-photon cross-sections.[184] The simulated absorbance decays track the experiment very well using the parameters described above, and are shown as the solid lines in figure 7.2. Excellent agreement with experiment is achieved by varying only the incident intensity for the three simulations. The incident intensity is attenuated by 5% in order to account for reflection losses described by the Fresnel equations. One advantage of using the simulation is to extract the percent contribution of molecules excited with one and two-photons. This simple model assumes only electric field interactions to convert the photoswitch molecules and will be of great use later in modeling the spatial dependence around the nanorods.

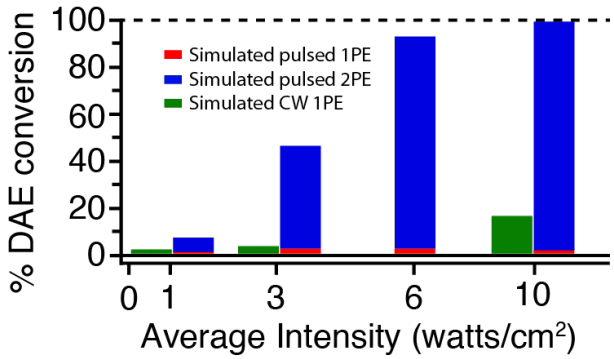

Figure 7.7: Bar chart shows the percent conversion after 15 mins with the breakdown of contributions from one- and two-photon excitation.

In order to compare the one and two-photon contributions to the net absorbance change, we calculated the fraction of molecules converted after 15 minutes using 10 ms step sizes of pulsed 800 nm exposure as a function of average intensity, shown in figure 7.7. This is displayed as a stacked bar graph where red is one-photon and blue is two-photon excitation contribution to the net conversion of the photoswitch sample. Pulsed excitation result in >98% of the net change in absorbance be due to the two-photon excitation at all intensities, reiterating that the dominate excitation mechanism is two-photon. To support this result we conducted the CW simulations where the intensity is too low to drive a two-photon process. The same average intensities were used as in the pulsed simulation. The simulated CW laser results are shown as the green bars. Given the two-photon cross section of 5.5 GM, under CW irradiation the intensity would need to be increased by >8 orders of magnitude in order for the two-photon excitation process to compete

with the one-photon process.

7.3.4 Simulating the Absorption Decay of DAE on Plasmonic Array

To simulate the absorbance decay of the photoswitch on the plasmonic array, the same simple model for simulating the absorbance decay on the glass substrate is used. Although, because of the distribution of intensities around the gold nanorod, conversion of the photoswitch molecules is calculated using a 2D grid with 10 ms time steps and the same dimensions as the enhanced field unit cell in figure 7.4. This overly simple model takes into account only the spatial dependence of the field strength from the calculated enhancement profiles. Probing the conversion of molecules to the open-ring isomer will have a weighted change in intensity dependent on the incident intensity. The weighted intensity change provides the sensitivity to the positions with the strongest intensity because that is where the greatest intensity change exists. Below, we consider additional factors in the simulation, including polarization anisotropy.

Although, the near-field simulated decays shown in figure 7.8 (top), do not give perfect agreement with the experiment, it does give the correct trends. Modifications to the model were made however to better represent the physical parameters in the experiment. The simulated signal initially decays too fast. In order to compensate for the rapid initial decay of the simulation, we decreased the field enhancement by 62% bring the maximum enhancement for the 800 nm profile from 13.5 to 5.1. The near-field calculation assumes a perfect ellipse shaped nanorod in a vacuum, neither condition is present in our experiment and so a lower enhancement is expected for the experimental array. A similar reduction is also applied to the probe field for consistency. The incident intensity is reduced by 60% due to the simulated signal decays being too fast even after the enhanced field reduction. Reduction of the incident intensity is to account for missing nanorods and damage to the plasmonic array, as well as the polarization anisotropy of the 800 nm and 580 nm probe in the near-field which will be discussed later. With the above modifications to the model, the simulated dashed trends in figure 7.9 (top) are produced. The only parameter that changed between the three simulations is the incident intensity.

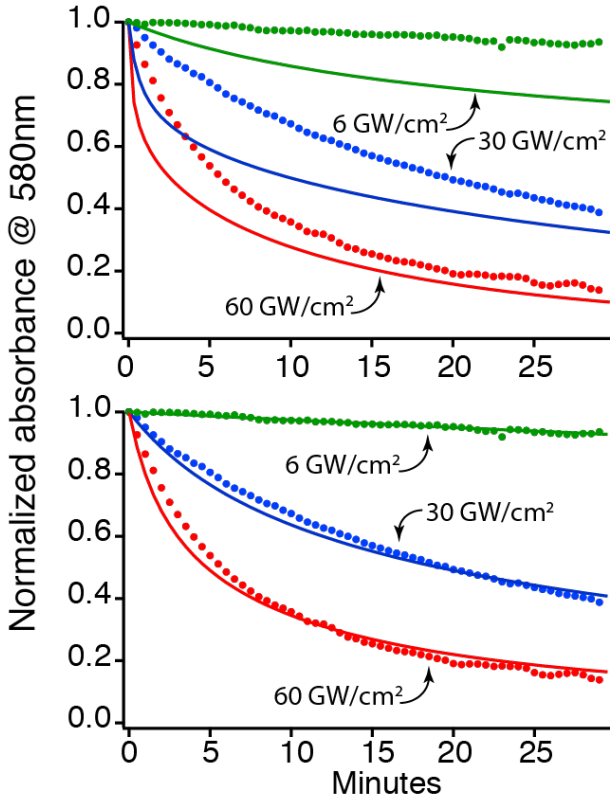

Figure 7.8: Top panel shows the simulations for the absorbance decay at 580 nm without polarization anisotropy and the bottom panel includes the anisotropy.

In an attempt to reduce the rapid simulation decay of the dashed lines in figure 9 (top) without reducing the incident intensity, the physical act of performing the measurement was examined. Due to the high intensity at the poles it is speculated that conversion is happening prior to the measurement taking place or the detector is not able to measure the rapid signal decay due to the one second of signal averaging during the measurement. Removal of the first simulated absorbance value is thought to compensate for such events. This did solve the rapid decay problem however the longer time decay limit of the simulation did not match the experiment and so was not included in the simulations.

The simulations up to this point in the chapter have neglected polarization anisotropy, however it provides an explanation for the slower absorbance decay rates observed in the experiment. Even for vertically polarized incident 800 nm and probe light, the wavelength dependence of the plasmon resonance produces slight variations in the directionality of the vector fields.

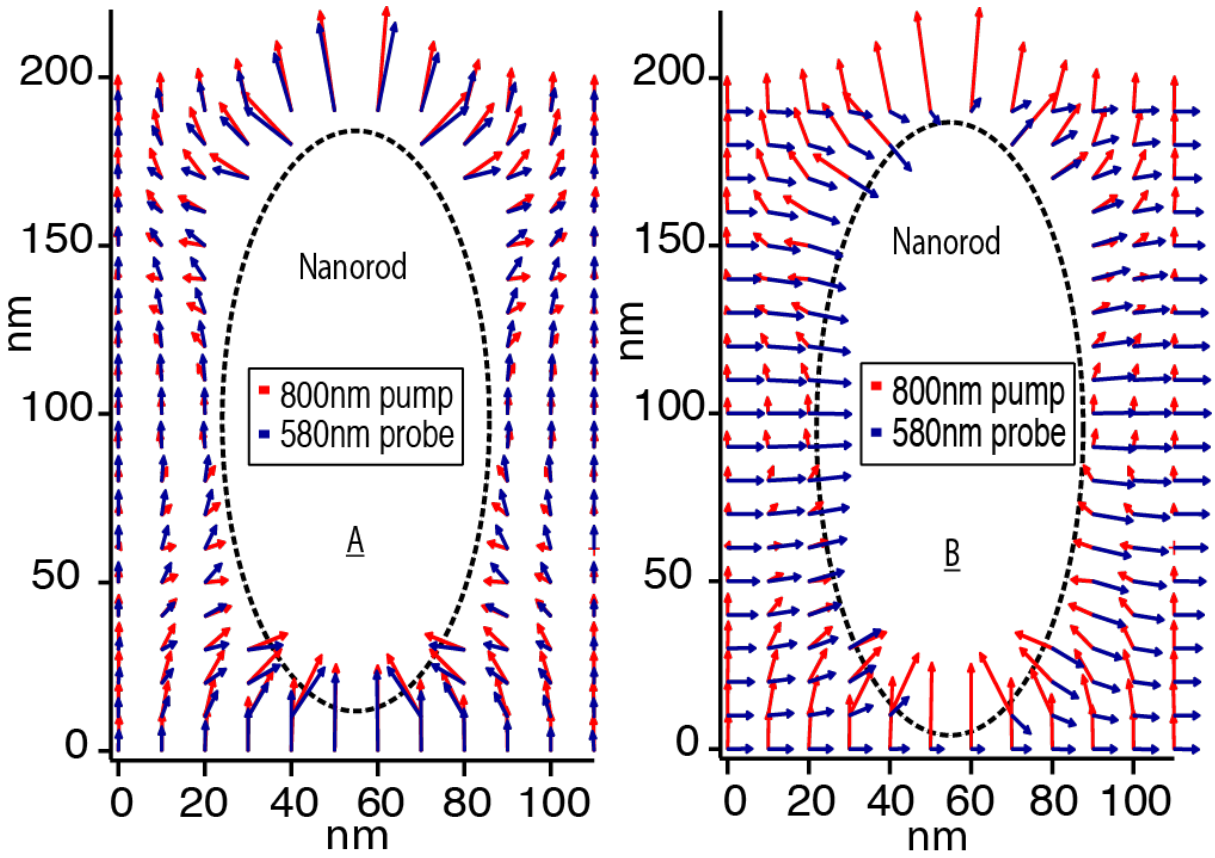

Figure 7.9: Left panel shows the vector field for vertical polarized 800 nm pump (red) and 580 (blue) while the right panel shows the vector field for a 90 degree rotated probe.

This is made evident in the calculated vector fields which is shown in figure 7.9. The 800 nm (red) and the 580 nm probe (blue) have vertical incident polarizations. This generates the greatest enhancement at the tips of the nanorod and is evident by the length of the arrow in each case. To help visualize figure 7.9, the magnitudes of the arrows are normalized and then square rooted due to the large difference in magnitude for some vectors. The value of this figure however, is in showing the direction of the electric field and how it changes as a function of position. At the tips of the nanorod in figure 7.9A the electric field vectors are similar in magnitude and direction. However, moving around the nanorod shows how the 800 nm and 580 nm probe vectors are no longer pointing in the same direction. At some points the angle between the two vectors is as large as 40 degrees even though the incident fields have parallel polarization. The difference in alignment of the 800 nm and 580 nm probe electric field vectors in the near-field will slow down

the absorbance decay rate. The slower rate is due to the 580 nm probe being less sensitive to converted DAE molecules. Figure 7.9B shows the case for when the 580 nm probe is perpendicular to the 800 nm. On the sides of the nanorod near 90 degree angles are present between the 800 nm and 580 nm probe vectors. When the angle between the 800 nm and 580 nm polarizations is near 90 degrees the observed absorbance will be decreased by nearly 66% in accordance with the anisotropy equations. At other locations around the nanorod the vectors are found to be pointing in the same direction despite the perpendicular orientation of the incident light fields.

Now we simulate the absorbance decay including polarization anisotropy at the different positions around the nanorod. The results show very good agreement with the experiment in figure 7.8 (bottom) as the solid lines. With the addition of polarization anisotropy the incident intensity is only reduced by 5% to account for reflection losses, because its reduction previously was to account for polarization anisotropy which is no longer needed. The enhancement to the electric field is kept at a reduction of 62% for both the 800 nm and 580 nm fields. At too high of intensities the photoswitch molecules will decompose and be unable to participate in the measured absorbance decay. To handle the rapid decay problem a damage threshold parameter was added. At intensities above $1.5x10^{11}\frac{watts}{cm^2}$ the photoswitch molecules are presumed to be damaged and are removed from the simulation.[242] The damage threshold parameter also accounts for missing nanorods and damaged areas to the array. Those areas will contribute less to the rapid conversion of photoswitch molecules, resulting in a slower initial rate. It is important to remember that the simulation is two dimensional, therefore the maximum enhancement will decrease with movement along the third dimension axis. Despite the simplicity of the model, these minor adjustments lead to simulated absorbance decays that give very good agreement with the experiment, as displayed in figure 7.8 (bottom) for the three different incident intensities.

To simulate the spatial probing, the enhanced electric field profile for a perpendicular probe field is used to probe the near-field after interaction with a vertical 800 nm electric field profile. It is apparent the perpendicular probe field is enhanced on the sides of the nanorod however the enhancement relative to the incident intensity is lower compared to the vertical probe. The mag-

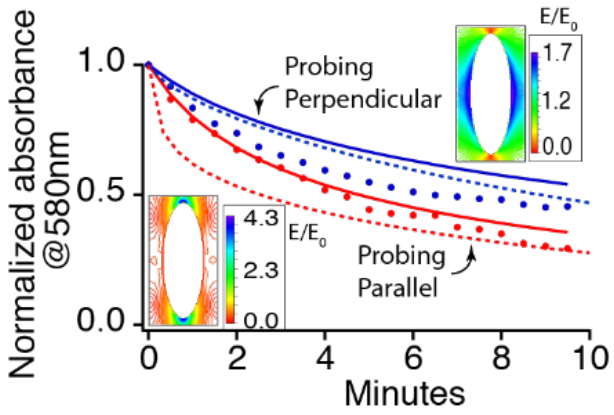

Figure 7.10: Absorbance at 580 nm with DAE on glass substrate (red) and plasmonic array (blue), exponential and bi-exponential fits (solid lines) are applied respectively. Irradiation intensity is 40 GW/cm2. Bottom panel show the calculated relative electric field enhancement to the incident field.

nitude of the perpendicular probe field enhancement is reduced in order to account for the smaller curvature of the nanorod compared to the tips. Even though the shorter horizontal dimensions of the nanorod give a plasmon resonance at shorter wavelengths, and is closer to the probe wavelength of 580 nm, the enhancement for the horizontal probe is less than the vertical probe. The 800 nm electric field profile is least sensitive to the molecules on the sides of the nanorod, where the perpendicular probe will have more sensitivity to those molecules. This produces the slower decaying absorbance in figure 7.10 (dashed lines) which show good trend agreement with the experiment. This simple model is only considering the spatial dependence of the enhanced electric field to simulate the change in absorbance, but neglects the relative polarization of the 800 nm and probe electric fields in the near-field. With the incorporation of polarization anisotropy in the simulation, the results (solid lines) show greater agreement with the experimental measurement.

7.4 Discussion and Conclusion

Incorporating the differences in electric field vector angles into the simulation along with the damage threshold of $1.5x10^{11}\frac{watts}{cm^2}$ significantly improved the agreement between simulation and experiment. This is still a simple model only taking electric field interactions into account. Probing

such a system with a transmission technique will emphasize not just where the strongest fields exist but also where the angle between the 800 nm and 580 nm probe polarizations is minimized. In the case of high intensities, a physical limit is acknowledged for the breakdown of the photoswitch molecule. However, it is likely other physical parameters or contributing to the decreased absorbance decay such as damage to the plasmonic array and neglecting the third dimension of the DAE film. Unlike a surface enhanced Raman spectroscopy measurement where molecules in the strong fields produce stronger signals, our system destroys the molecules. Leaving the observed absorbance decay to be comprised of molecules converting on the sides of the nanorod. We emphasize that our transmission measurement probes a different subset of molecules than would be observed using SERS.

The entirety of this chapter has focused on one type of interaction a plasmonic nanoparticle can have with molecules in its near-field and that is with the strong electric field produced from oscillating surface plasmons. By ignoring all other interactions, this one mechanism for interaction was able to explain all the observables in our experimental measurements. Thermal conversion has already previously been ruled out from taking part in contributing to the cycloreversion reaction due to its thermal stability. Another possible contribution to the cycloreversion reaction is hot electron transfer. This would involve exciting an electron in the gold nanorod to the lowest unoccupied molecular orbital (LUMO), then with mixing of the orbitals between the DAE molecule and the gold an electron transfer could occur. This is limited greatly by the distance dependence, and could only be a dominant contributing mechanism for distances up to a couple nanometers from the gold surface. Therefore, the hot electron transfer is unable to explain the degree of conversion in our experiments.

We have shown the conversion rate of DAE in the presence of periodically spaced plasmonic nanorods is increased under 800 nm irradiation due to the enhanced electric field. This conversion process is dominated by two-photon excitation. Probing the conversion required a greater level of detail due to the distribution of intensities that exist around the nanorod. This distribution caused preferential probing in the regions with the strongest field which for polarization along length

of the nanorod was the tips of the nanorod. Rotation of the 580 nm probe to be perpendicular with respect to the 800 nm polarization does not yield a large enhancement from the nanorod but is sensitive spatially to where majority of the closed-ring DAE molecules exist. This opens up the possibility to selectively probe different regions around the nanorod based on polarization. A simple simulation for the transmission of light through a sample yielded good trend agreement for both glass and plasmonic array substrates when only the intensity of the 800 nm and 580 nm probe fields were considered. However, it was apparent that the polarization anisotropy played a more significant role in reducing the initial decay rates. With the polarization anisotropy included in the simulation the agreement to the experiment was very good. The model accurately reproduces all of the experimental observables using only electric field interactions to convert the photoswitch. For this system the mechanism for the interaction of the plasmonic nanorod with molecules in the near-field is entirely attributed to the electric field enhancement.

Chapter 8

Summary and Future Directions

Throughout this dissertation we have used ultrafast transient electronic absorption spectroscopy and transient x-ray absorption spectroscopy to examine the kinetics and dynamics of photo-activated molecules in the condensed phase in order to gain insight into the fundamental chemistry that governs the reactive pathways. It has been shown that the environment plays an important role in restricting or enhancing different reactive pathways which influence the reaction rates, yields and products formed. By elucidating the interactions between a photo-activated molecule and its environment we gain a more detailed picture of the excited-state relaxation mechanisms, as well as providing a starting point for understanding how the environment can control chemistry for much more complex systems such as bio-molecules. The investigated photo-activated systems include confining alkyl-substituted stilbene and azobenzene molecules inside of an OA_2 capsule, elucidating the photodecomposition mechanism for a manganese tricarbonyl complex in coordinating and non-coordinating solvents, and using the plasmonic field from an array of hold nanorods to drive nonlinear excitation of a photochromic molecule.

The investigation into how confined environments affect the excited-state kinetics and dynamics began with encapsulating a stilbene molecule inside the OA_2 capsule. Stilbene was chosen for being a model system for photoisomerization with a well-known *trans-cis* isomerization mechanism. Additionally, stilbene also contains the fundamental components for more complex photoisomerization reactions found in vision and phototaxy, which can take place in crowded biological environments. The confined environment was shown to affect the planar ground-state structure of the stilbene molecule, resulting in the stilbene structure to be bent slightly out of plane. Although not the case for stilbene, the slight change in structure could pre-align other molecules

into a geometry primed for excited-state chemistry. From the ultrafast transient spectroscopy the excited-state lifetime for stilbene in the OA_2 capsule is lengthened due to the steric restrictions for the phenyl ring to rotate in the excited-state. The confined environment is also shown to decrease the *trans*→*cis* isomerization quantum yield, caused by changes to the excited-state potential energy surface geometry near the conical intersection as a result of destabilizing the *cis* isomer.

We changed the length of the stilbene molecule inside the OA_2 capsule using alkyl-substituents which effect the amount of crowding felt by the molecule. By decreasing the room for the stilbene molecule to rotate in the OA_2 capsule a longer excited-state lifetime is measured. Although, for the lengthened stilbene derivatives the quantum yield is shown to decrease less compared to the shorter stilbene derivatives. Crowding the stilbene derivatives in the the OA_2 capsule demonstrates how the environment can restrict the isomerization pathways while also changing the ratio of photoproducts formed. Investigating the excited-state dynamics and kinetics using alkyl-substituted stilbene derivatives has revealed new details about photoisomerization in confined environments.

Following the encapsulated stilbene work we then encapsulated an azobenzene molecule, which is a prototypical photochromic compound similar to stilbene but with more degrees of freedom to move during the isomerization reaction. The ability for azobenzene to isomerize by rotation or inversion made the mechanism for the excited-state relaxation heavily debated. The ultrafast transient absorption measurements show that in comparison to solution, the encapsulated azobenzene molecule has an increased lifetime which increases with the molecular length using alkyl-substitutions. The increased lifetime is due to the increased sterical hindrance for rotation of the phenyl within the capsule. We also observe an additional pathway in the excited-state leading to an S_1' species and is attributed to the *cis* isomer for the mono-substituted azobenzene derivatives. This pathways is not observed for azobenzene in solution and shows how the confined environment can facilitate different reaction pathways in the excited-state. The di-substituted azobenzene molecules in the OA_2 capsule showed restrictive motion to the inversion mechanism which resulted in significantly lower *trans*→*cis* quantum yields. Additionally, the S_1' species for the di-substituted azobenzene molecule in the capsule is suggested to be a highly out-of-plane distorted geometry.

Future work involving calculations would help to gain insight into what the distorted structure might look like and provide details about the relaxation mechanism from the distorted structure.

Moving forward with the confined environment, we can use the capsule to look at aromatic cation radicals following multi-photon ionization. From other studies, it has been shown that exciting the guest species can transfer an electron to the capsule and then to a species outside of the capsule.[128] This would leave the cation species in the capsule which would also possibly act as a barrier for recombination with the electron. It is known that in nonpolar solvents the dynamics following ionization can be described as the classical diffusion of ions in a Coulombic field. However, in polar solvents the dynamics are significantly different due to the reorganizing solvent around the cation species.[243] In addition to the solvent reorganization, the cation species will vibrationally and structurally relax on the femto- to picosecond timescale.[244] An important factor in this system is the cation - electron distance, which cannot be shorter than the Onsager radius. If the cation and electron are too close then geminate recombination will dominate the reaction process. Having the OA_2 capsule acting as a barrier will increase the probability for the electron and cation to remain separated. Additionally, this study would be informative for how the capsule responds to a charged guest species.

Another possible future direction for the capsule project is to measure bimolecular reactions inside the OA_2 capsule. Bimolecular reactions in solution are difficult to measure due to the diffusion limited rate and low number density.[149] However, bimolecular reactions have importance in biological settings where the highly crowded environment play a role in dynamical process, for example, the rate of a reaction might increase if the crowding positions the molecules favors the transition state.[245,246] In order to measure the bimolecular reaction both molecules will be encapsulated, after photo-excitation the reaction could be monitored using ultrafast absorption spectroscopy. The information from this investigation would yield fundamental information about the energy barrier for the reaction as well as measure the the timescale for the bimolecular reaction directly.

For the photodecomposition of a manganese tricarbonyl complex, the focus was on elucidat-

ing the mechanism for photodecomposition, where we used a combination of ultrafast transient absorption and x-ray absorption spectroscopy in this investigation. From the ultrafast transient absorption we observed the excited MLCT state of the manganese tricarbonyl complex which relaxes by BET resulting in the loss of a CO ligand to form a 5-coordinate species. The 5-coordinate goes on to react via two possible competing pathways, the first involving solvent coordination to the Mn center and the second suggests the 5-coordinate Mn species reduces the starting compound to form a Mn^0 species. Using DCE, a non-coordinating solvent, forces the decomposition reaction to follow a single pathway, however the ultrafast absorption signal was not very sensitive to the different Mn complex structures. Therefore we conducted transient x-ray absorption measurements on the sample to extract the structural information about the various species in the photodecomposition reaction of the manganese tricarbonyl complex. The XAS K-edge shift to lower energy show the difference between the 5-coordinate and the solvent-coordinated species, as well as the evolution of the XAS on the μs timescale. The information gained from the x-ray measurements support the solvent-coordinated species being the dominating pathway in the photodecomposition mechanisms. In order to provide a more definitive idea for the Mn complex strucutre during the decomposition reaction, x-ray measurements focusing on the fine structure region are needed. Additionally, modeling will be required to fit the fine structure, which will also aid in interpreting the photodecomposition reaction.

The environment surrounding a plasmonic nanostructure is known to interact with the near-field through a variety of mechanisms such as thermal, electron transfer, or strong electric fields. However, we only focus on understanding the strong electric field interaction to increase the conversion rate of DAE molecules. Pulsed 800 nm laser light was used to drive the placmonic resonance of a periodically spaced gold nanorod array with a thin film of DAE molecules over it. The induced electric field drives a two-photon excitation of the DAE molecules. Probing the conversion required a greater level of detail due to the distribution of intensities around the nanorod. The different intensities result in preferential probing in the regions with the stronger electric fields. Additionally, the probe has its own intensity profile around the nanorod with a slight difference in

polarization compared to the 800 nm laser light. We used a simple simulation, which incorporated the different intensity profiles and polarizations for the 800 nm and probe light, for the transmission of light through the sample. The results from the simulation showed good trend agreement with the experiment. The information gained from examining the interaction between the DAE molecule and the plasmonic nanoparticle emphasizes the importance of understanding the reaction environment which aids in interpreting the results of the measurements.

Chapter 9

Bibliography

[1] Ward, C. L.; Elles, C. G. Cycloreversion Dynamics of a Photochromic Molecular Switch via One-Photon and Sequential Two-Photon Excitation. *J. Phys. Chem. A* **2014**, *118*, 10011–10019.

[2] Young, L. et al. Roadmap of ultrafast x-ray atomic and molecular physics. *Journal of Physics B: Atomic, Molecular and Optical Physics* **2018**, *51*, 032003.

[3] Kubelka, J.; Hofrichter, J.; Eaton, W. A. The protein folding 'speed limit'. *Current Opinion in Structural Biology* **2004**, *14*, 76–88.

[4] Fuss, W. Hula-twist cis–trans isomerization: The role of internal forces and the origin of regioselectivity. *Journal of Photochemistry and Photobiology A: Chemistry* **2012**, *237*, 53–63.

[5] Otolski, C. J.; Raj, A. M.; Ramamurthy, V.; Elles, C. G. Ultrafast Dynamics of Encapsulated Molecules Reveals New Insight on the Photoisomerization Mechanism for Azobenzenes. *J. Phys. Chem. Lett.* **2019**, *10*, 121–127.

[6] Otolski, C. J.; Mohan Raj, A.; Gaurav, S.; Prabhakar, R.; Ramamurthy, V.; Elles, C. G. Ultrafast *trans*→*cis* photoisomerization dynamics of alkyl-substituted stilbenes in a supramolecular capsule. *JPCA* **2019**, in press.

[7] Rothenberger, G.; Negus, D.; Hochstrasser, R. Solvent Influence on Photo-Isomerization Dynamics. *J. Phys. Chem.* **1983**, *79*, 5360–5367.

[8] Courtney, S.; Fleming, G. Photoisomerization Of Stilbene In Low Viscosity Solvents - Comparison Of Isolated And Solvated Molecules. *J. Phys. Chem.* **1985**, *83*, 215–222.

[9] Hynes, J. Chemical-Reaction Dynamics In Solution. *Annu. Rev. Phys. Chem.* **1985**, *36*, 573–597.

[10] Fleming, G.; Wolynes, P. Chemical-Dynamics In Solution. *Physics Today* **1990**, *43*, 36–43.

[11] Elles, C. G.; Crim, F. F. Connecting chemical dynamics in gases and liquids. *Annu. Rev. Phys. Chem.* **2006**, *57*, 273–302.

[12] Carpenter, B. K.; Harvey, J. N.; Orr-Ewing, A. J. The Study of Reactive Intermediates in Condensed Phases. *J. Am. Chem. Soc.* **2016**, *138*, 4695–4705.

[13] Garcia-Meseguer, R.; Carpenter, B. K. Re-Evaluating the Transition State for Reactions in Solution. *Eur. J. Org. Chem.* **2019**, 254–266.

[14] Imamoto, Y.; Kataoka, M.; Liu, R. Mechanistic pathways for the photoisomerization reaction of the anchored, tethered chromophore of the photoactive yellow protein and its mutants. *Photochem. Photobio.* **2002**, *76*, 584–589.

[15] Mandal, D.; Tahara, T.; Meech, S. Excited-state dynamics in the green fluorescent protein chromophore. *J. Phys. Chem. B* **2004**, *108*, 1102–1108.

[16] Gozem, S.; Luk, H. L.; Schapiro, I.; Olivucci, M. Theory and simulation of the ultrafast double-bond isomerization of biological chromophores. *Chem. Rev.* **2017**, *117*, 13502–13565.

[17] Ernst, O. P.; Lodowski, D. T.; Elstner, M.; Hegemann, P.; Brown, L. S.; Kandori, H. Microbial and animal rhodopsins: Structures, functions, and molecular mechanisms. *Chem. Rev.* **2014**, *114*, 126–163.

[18] Vengris, M.; van der Horst, M.; Zgrablic, G.; van Stokkum, I.; Haacke, S.; Chergui, M.; Hellingwerf, K.; van Grondelle, R.; Larsen, D. Contrasting the excited-state dynamics of

the photoactive yellow protein chromophore: Protein versus solvent environments. *Biophys. J.* **2004**, *87*, 1848–1857.

[19] Kukura, P.; McCamant, D.; Yoon, S.; Wandschneider, D.; Mathies, R. Structural observation of the primary isomerization in vision with femtosecond-stimulated Raman. *Science* **2005**, *310*, 1006–1009.

[20] Polli, D.; Altoe, P.; Weingart, O.; Spillane, K. M.; Manzoni, C.; Brida, D.; Tomasello, G.; Orlandi, G.; Kukura, P.; Mathies, R. A.; Garavelli, M.; Cerullo, G. Conical intersection dynamics of the primary photoisomerization event in vision. *Nature* **2010**, *467*, 440–443.

[21] Gozem, S.; Luk, H. L.; Schapiro, I.; Olivucci, M. Theory and simulation of the ultrafast double-bond isomerization of biological chromophores. *Chem. Rev.* **2017**, *117*, 13502–13565.

[22] Liu, R.; Hammond, G. The case of medium-dependent dual mechanisms for photoisomerization: One-bond-flip and Hula-Twist. *Proc. Nat. Acad. Sci.* **2000**, *97*, 11153–11158.

[23] Liu, R. S. H.; Hammond, G. S. Reflection on medium effects on photochemical reactivity. *Acc. Chem. Res.* **2005**, *38*, 396–403.

[24] Parthasarathy, A.; Ramamurthy, V. Water-soluble octa acid capsule as a reaction container: Templated photodimerization of indene in water. *J. Photochem. Photobiol. A* **2016**, *317*, 132–139.

[25] Douhal, A. Ultrafast Guest Dynamics in Cyclodextrin Nanocavities. *Chemical Reviews* **2004**, *104*, 1955–1976.

[26] Szejtli, J. Introduction and General Overview of Cyclodextrin Chemistry. *Chemical Reviews* **1998**, *98*, 1743–1754.

[27] Duveneck, G.; Sitzmann, E.; Eisenthal, K.; Turro, N. Picosecond laser studies on

photochemical-reactions in restricted environments: The photoisomerization of *trans*-stilbene complexed to cyclodextrins. *J. Phys. Chem.* **1989**, *93*, 7166–7170.

[28] Mariano Correa, N.; Silber, J. J.; Riter, R. E.; Levinger, N. E. Nonaqueous Polar Solvents in Reverse Micelle Systems. *Chem. Rev.* **2012**, *112*, 4569–4602.

[29] Walton, I. M.; Cox, J. M.; Coppin, J. A.; Linderman, C. M.; Patel, D. G. D.; Benedict, J. B. Photo-responsive MOFs: light-induced switching of porous single crystals containing a photochromic diarylethene. *Chem. Comm.* **2013**, *49*, 8012–8014.

[30] Hermann, D.; Emerich, H.; Lepski, R.; Schaniel, D.; Ruschewitz, U. Metal-Organic Frameworks as Hosts for Photochromic Guest Molecules. *Inorg. Chem.* **2013**, *52*, 2744–2749.

[31] Dolgopolova, E. A.; Moore, T. M.; Ejegbavwo, O. A.; Pellechia, P. J.; Smith, M. D.; Shustova, N. B. A metal-organic framework as a flask: photophysics of confined chromophores with a benzylidene imidazolinone core. *Chem. Comm.* **2017**, *53*, 7361–7364.

[32] Samanta, D.; Gemen, J.; Chu, Z.; Diskin-Posner, Y.; Shimon, L. J. W.; Klajn, R. Reversible photoswitching of encapsulated azobenzenes in water. *Proc. Nat. Acad. Sci.* **2018**, *115*, 9379–9384.

[33] Williams, D. E.; Martin, C. R.; Dolgopolova, E. A.; Swifton, A.; Godfrey, D. C.; Ejegbavwo, O. A.; Pellechia, P. J.; Smith, M. D.; Shustova, N. B. Flipping the Switch: Fast Photoisomerization in a Confined Environment. *J. Am. Chem. Soc.* **2018**, *140*, 7611–7622.

[34] Ferreira, P.; Ventura, B.; Barbieri, A.; Da Silva, J. P.; Laia, C. A. T.; Jorge Parola, A.; Basilie, N. A Visible-Near-Infrared Light-Responsive Host-Guest Pair with Nanomolar Affinity in Water. *Chem. Eur. J.* **2019**, *25*, 3477–3482.

[35] Muraoka, T.; Kinbara, K.; Aida, T. Mechanical twisting of a guest by a photoresponsive host. *Nature* **2006**, *440*, 512.

[36] Ramamurthy, V. Photochemistry within a water-soluble organic capsule. *Acc. Chem. Res.* **2015**, *48*, 2904–2917.

[37] Otte, M. Size-selective molecular flasks. *ACS Catal.* **2016**, *6*, 6491–6510.

[38] Valentini, A.; Rivero, D.; Zapata, F.; Garcia-Iriepa, C.; Marazzi, M.; Palmeiro, R.; Galvan, I. F.; Sampedro, D.; Olivucci, M.; Manuel Frutos, L. Optomechanical control of quantum yield in *trans-cis* ultrafast photoisomerization of a retinal chromophore model. *Angew. Chem., Int. Ed.* **2017**, *56*, 3842–3846.

[39] Gibb, C. L. D.; Li, X.; Gibb, B. C. Adjusting the binding thermodynamics, kinetics, and orientation of guests within large synthetic hydrophobic pockets. *Proc. Nat. Acad. Sci.* **2002**, *99*, 4857–4862.

[40] Ramamurthy, V. Photochemistry within a water-soluble organic capsule. *Acc. Chem. Rev.* **2015**, *48*, 2904–2917.

[41] Parthasarathy, A.; Kaanumalle, L. S.; Ramamurthy, V. Controlling photochemical geometric isomerization of a stilbene and dimerization of a styrene using a confined reaction cavity in water. *Org. Lett.* **2007**, *9*, 5059–5062.

[42] Parthasarathy, A.; Ramamurthy, V. Role of free space and weak interactions on geometric isomerization of stilbenes held in a molecular container. *Photochem. Photobio. Sci.* **2011**, *10*, 1455–1462.

[43] Samanta, S. R.; Parthasarathy, A.; Ramamurthy, V. Supramolecular control during triplet sensitized geometric isomerization of stilbenes encapsulated in a water soluble organic capsule. *Photochem. Photobio. Sci.* **2012**, *11*, 1652–1660.

[44] Hammond, G.; Saltiel, J.; Bradshaw, J.; Turro, N.; Lamola, A.; Vogt, V.; Counsell, R.; Cowan, D.; Dalton, C. Mechanisms Of Photochemical Reactions In Solution .22. Photochemical Cis-Trans Isomerization. *J. Am. Chem. Soc.* **1964**, *86*, 3197–3216.

[45] Saltiel, J. Perdeuteriostilbene. Role Of Phantom States in cis-trans Photoisomerization of Stilbenes. *J. Am. Chem. Soc.* **1967**, *89*, 1036–1037.

[46] Orlandi, G.; Siebrand, W. Model For Direct Photoisomerization Of Stilbene. *Chem. Phys. Lett.* **1975**, *30*, 352–354.

[47] Saltiel, J.; D'Agostino, J. Separation Of Viscosity And Temperature Effects On Singlet Pathway To Stilbene Photoisomerization. *J. Am. Chem. Soc.* **1972**, *94*, 6445–6456.

[48] Greene, B.; Hochstrasser, R.; Weisman, R. Spectroscopic Study Of The Picosecond Photoisomerization Of Stilbene. *Chem. Phys. Lett.* **1979**, *62*, 427–430.

[49] Saltiel, J.; Sun, Y. Intrinsic Potential-Energy Barrier For Twisting In The Trans-Stilbene S1 State In Hydrocarbon Solvents. *J. Chem. Phys.* **1989**, *93*, 6246–6250.

[50] Sun, Y.; Saltiel, J. Application Of The Kramers Equation To Stilbene Photoisomerization In Normal-Alkanes Using Translational Diffusion-Coefficients To Define Microviscosity. *J. Chem. Phys.* **1989**, *93*, 8310–8316.

[51] Waldeck, D. Photoisomerization dynamics of stilbenes. *Chem. Rev.* **1991**, *91*, 415–436.

[52] Quenneville, J.; Martínez, T. J. Ab initio study of *cis-trans* photoisomerization in stilbene and ethylene. *J. Phys. Chem. A* **2003**, *107*, 829–837.

[53] Levine, B. G.; Martinez, T. J. Isomerization through conical intersections. *Annu. Rev. Phys. Chem.* **2007**, *58*, 613–634.

[54] Quick, M.; Berndt, F.; Dobryakov, A. L.; Ioffe, I. N.; Granovsky, A. A.; Knie, C.; Mahrwald, R.; Lenoir, D.; Ernsting, N. P.; Kovalenko, S. A. Photoisomerization Dynamics of Stiff-Stilbene in Solution. *J. Phys. Chem. B* **2014**, *118*, 1389–1402.

[55] Kumpulainen, T.; Lang, B.; Rosspeintner, A.; Vauthey, E. Ultrafast Elementary Photochemical Processes of Organic Molecules in Liquid Solution. *Chem. Rev.* **2017**, *117*, 10826–10939.

[56] Tzeli, D.; Theodorakopoulos, G.; Petsalakis, I. D.; Ajami, D.; Rebek, J., Jr. Conformations and Fluorescence of Encapsulated Stilbene. *J. Am. Chem. Soc.* **2012**, *134*, 4346–4354.

[57] Bhandari, S.; Zheng, Z.; Maiti, B.; Chuang, C.-H.; Porel, M.; You, Z.-Q.; Rarnamurthy, V.; Burda, C.; Herbert, J. M.; Dunietz, B. D. What Is the Optoelectronic Effect of the Capsule on the Guest Molecule in Aqueous Host/Guest Complexes? A Combined Computational and Spectroscopic Perspective. *J. Phys. Chem. C* **2017**, *121*, 15481–15488.

[58] Garcia-Iriepa, C.; Sampedro, D.; Mendicuti, F.; Leonard, J.; Manuel Frutos, L. Photoreactivity Control Mediated by Molecular Force Probes in Stilbene. *J. Phys. Chem. Lett.* **2019**, *10*, 1063–1067.

[59] Wei-Guang Diau, E. A New *trans*-to-*cis* Photoisomerization Mechanism of Azobenzene on the $S_1(n,\pi^*)$ Surface. *The Journal of Physical Chemistry A* **2004**, *108*, 950–956.

[60] Lednev, I. K.; Ye, T.-Q.; Hester, R. E.; Moore, J. N. Femtosecond Time-Resolved UV-Visible Absorption Spectroscopy of *trans*-Azobenzene in Solution. *The Journal of Physical Chemistry* **1996**, *100*, 13338–13341.

[61] Stuart, C. M.; Frontiera, R. R.; Mathies, R. A. Excited-State Structure and Dynamics of *cis*- and *trans*-Azobenzene from Resonance Raman Intensity Analysis. *The Journal of Physical Chemistry A* **2007**, *111*, 12072–12080.

[62] Fujino, T.; Tahara, T. Picosecond Time-Resolved Raman Study of *trans*-Azobenzene. *The Journal of Physical Chemistry A* **2000**, *104*, 4203–4210.

[63] Satzger, H.; Root, C.; Braun, M. Excited-State Dynamics of *trans*- and *cis*-Azobenzene after UV Excitation in the $\pi\pi^*$ Band. *The Journal of Physical Chemistry A* **2004**, *108*, 6265–6271.

[64] Fujino, T.; Arzhantsev, S. Y.; Tahara, T. Femtosecond Time-Resolved Fluorescence Study of

Photoisomerization of trans-Azobenzene. *The Journal of Physical Chemistry A* **2001**, *105*, 8123–8129.

[65] Chang, C.-W.; Lu, Y.-C.; Wang, T.-T.; Diau, E. W.-G. Photoisomerization Dynamics of Azobenzene in Solution with S1 Excitation: A Femtosecond Fluorescence Anisotropy Study. *Journal of the American Chemical Society* **2004**, *126*, 10109–10118, PMID: 15303887.

[66] Abel, E. W.; Bennett, M. A.; Wilkinson, G. Substituted carbonyl compounds of chromium, molybdenum, tungsten, and manganese. *Journal of the Chemical Society (Resumed)* **1959**, 2323–2327.

[67] Hawecker, J.; Lehn, J.-M.; Ziessel, R. Electrocatalytic reduction of carbon dioxide mediated by Re(bipy)(CO)3Cl (bipy = 2,2[prime or minute]-bipyridine). *Journal of the Chemical Society, Chemical Communications* **1984**, 328–330.

[68] Sullivan, B. P.; Bolinger, C. M.; Conrad, D.; Vining, W. J.; Meyer, T. J. One- and two-electron pathways in the electrocatalytic reduction of CO2 by fac-Re(bpy)(CO)3Cl (bpy = 2,2'-bipyridine). *Journal of the Chemical Society, Chemical Communications* **1985**, 1414–1416.

[69] Vollmer, M. V.; Machan, C. W.; Clark, M. L.; Antholine, W. E.; Agarwal, J.; Schaefer, H. F.; Kubiak, C. P.; Walensky, J. R. Synthesis, Spectroscopy, and Electrochemistry of (α-Diimine)M(CO)3Br, M = Mn, Re, Complexes: Ligands Isoelectronic to Bipyridyl Show Differences in CO2 Reduction. *Organometallics* **2015**, *34*, 3–12.

[70] Blakemore, J. D.; Gupta, A.; Warren, J. J.; Brunschwig, B. S.; Gray, H. B. Noncovalent Immobilization of Electrocatalysts on Carbon Electrodes for Fuel Production. *Journal of the American Chemical Society* **2013**, *135*, 18288–18291.

[71] Takeda, H.; Kamiyama, H.; Okamoto, K.; Irimajiri, M.; Mizutani, T.; Koike, K.; Sekine, A.; Ishitani, O. Highly Efficient and Robust Photocatalytic Systems for CO2 Reduction Consist-

ing of a Cu(I) Photosensitizer and Mn(I) Catalysts. *J. Am. Chem. Soc.* **2018**, *140*, 17241–17254.

[72] Agarwal, J.; Stanton Iii, C. J.; Shaw, T. W.; Vandezande, J. E.; Majetich, G. F.; Bocarsly, A. B.; Schaefer Iii, H. F. Exploring the effect of axial ligand substitution (X = Br, NCS, CN) on the photodecomposition and electrochemical activity of [MnX(N-C)(CO)3] complexes. *Dalton Transactions* **2015**, *44*, 2122–2131.

[73] Hughey, J. L.; Anderson, C. P.; Meyer, T. J. Photochemistry of Mn2(CO)10. *Journal of Organometallic Chemistry* **1977**, *125*, C49–C52.

[74] Motterlini, R.; Clark, J. E.; Foresti, R.; Sarathchandra, P.; Mann, B. E.; Green, C. J. Carbon Monoxide-Releasing Molecules: Characterization of Biochemical and Vascular Activities. *Circulation Research: Journal of the American Heart Association* **2002**, *90*, e17–e24.

[75] Glyn, P.; George, M. W.; Hodges, P. M.; Turner, J. J. Fast time-resolved IR studies of the excited states of co-ordination compound: direct observation of intramolecular charge transfer. *Journal of the Chemical Society, Chemical Communications* **1989**, 1655–1657.

[76] Sato, S.; Matubara, Y.; Koike, K.; Falkenström, M.; Katayama, T.; Ishibashi, Y.; Miyasaka, H.; Taniguchi, S.; Chosrowjan, H.; Mataga, N.; Fukazawa, N.; Koshihara, S.; Onda, K.; Ishitani, O. Photochemistry of fac-[Re(bpy)(CO)3Cl]. *Chemistry - A European Journal* **2012**, *18*, 15722–15734.

[77] Stockman, M. I. Nanoplasmonics: The physics behind the applications. *Physics Today* **2011**, *64*, 39–44.

[78] Guidez, E. B.; Aikens, C. M. Quantum mechanical origin of the plasmon: from molecular systems to nanoparticles. *Nanoscale* **2014**, *6*, 11512–11527.

[79] Kelly, K. L.; Coronado, E.; Zhao, L. L.; Schatz, G. C. The Optical Properties of Metal

Nanoparticles: The Influence of Size, Shape, and Dielectric Environment. *The Journal of Physical Chemistry B* **2003**, *107*, 668–677.

[80] Hao, E.; Schatz, G. C. Electromagnetic fields around silver nanoparticles and dimers. *The Journal of Chemical Physics* **2003**, *120*, 357–366.

[81] Keller, E. L.; Brandt, N. C.; Cassabaum, A. A.; Frontiera, R. R. Ultrafast surface-enhanced Raman spectroscopy. *Analyst* **2015**, *140*, 4922–4931.

[82] Fateixa, S.; Nogueira, H. I. S.; Trindade, T. Hybrid nanostructures for SERS: materials development and chemical detection. *Phys. Chem. Chem. Phys.* **2015**, *17*, 21046–21071.

[83] Cushing, S. K.; Wu, N. Progress and perspectives of plasmon-enhanced solar energy conversion. *J. Phys. Chem. Lett.* **2016**, *7*, 666–675.

[84] Linic, S.; Christopher, P.; Ingram, D. B. Plasmonic-metal nanostructures for efficient conversion of solar to chemical energy. *Nature Materials* **2011**, *10*, 911–921.

[85] Atwater, H. A.; Polman, A. Plasmonics for improved photovoltaic devices. *Nature Materials* **2010**, *9*, 205–213.

[86] Tsuboi, Y.; Shimizu, R.; Shoji, T.; Kitamura, N. Near-Infrared Continuous-Wave Light Driving a Two-Photon Photochromic Reaction with the Assistance of Localized Surface Plasmon. *Journal of the American Chemical Society* **2009**, *131*, 12623–12627.

[87] Tsuboi, Y.; Shimizu, R.; Shoji, T.; Kitamura, N.; Takase, M.; Murakoshi, K. Acceleration of a photochromic ring-opening reaction of diarylethene derivatives by excitation of localized surface plasmon. *Journal of Photochemistry and Photobiology A: Chemistry* **2011**, *221*, 250–255.

[88] Wu, B.; Ueno, K.; Yokota, Y.; Sun, K.; Zeng, H.; Misawa, H. Enhancement of a Two-Photon-Induced Reaction in Solution Using Light-Harvesting Gold Nanodimer Structures. *The Journal of Physical Chemistry Letters* **2012**, *3*, 1443–1447.

[89] Nishi, H.; Asahi, T.; Kobatake, S. Enhanced photocycloreversion reaction of diarylethene polymers attached to gold nanoparticles in the solid state. *Journal of Photochemistry and Photobiology A: Chemistry* **2011**, *221*, 256–260.

[90] Guillaume, B.; Quidant, R. Nanoplasmonics for chemistry. *Chem. Soc. Rev.* **2014**, *43*, 3898–3907.

[91] Baffou, G.; Quidant, R. Thermo-plasmonics: using metallic nanostructures as nano-sources of heat. *Laser & Photonics Reviews* **2013**, *7*, 171–187.

[92] Ryoji, T.; Satoshi, K.; Shintaro, F.; Manabu, K. Photochromic reaction of the diarylethene derivative on Au nanoparticles. *Advances in Natural Sciences: Nanoscience and Nanotechnology* **2015**, *6*, 015006.

[93] Nishi, H.; Asahi, T.; Kobatake, S. Plasmonic Enhancement of a Photocycloreversion Reaction of a Diarylethene Derivative Using Individually Dispersed Silver Nanoparticles. *ChemPhysChem* **2012**, *13*, 3616–3621.

[94] Takao, O.; Katsuhiro, I.; Francesca, P.; Tomoya, T.; Koh-ichi, N.; Kazushi, M. Plasmon-Resonant Optics on an Indium–Tin-Oxide Film for Exciting a Two-Photon Photochromic Reaction. *Applied Physics Express* **2013**, *6*, 102001.

[95] Albrecht, W.; Deng, T.-S.; Goris, B.; van Huis, M. A.; Bals, S.; van Blaaderen, A. Single Particle Deformation and Analysis of Silica-Coated Gold Nanorods before and after Femtosecond Laser Pulse Excitation. *Nano Letters* **2016**, *16*, 1818–1825.

[96] Ueno, K.; Misawa, H. Photochemical reaction fields with strong coupling between a photon and a molecule. *Journal of Photochemistry and Photobiology A: Chemistry* **2011**, *221*, 130–137.

[97] Du, L.; Furube, A.; Hara, K.; Katoh, R.; Tachiya, M. Plasmon induced electron transfer

at gold–TiO2 interface under femtosecond near-IR two-photon excitation. *Thin Solid Films* **2009**, *518*, 861–864.

[98] Nishi, H.; Asahi, T.; Kobatake, S. Plasmonic enhancement of gold nanoparticles on photocycloreversion reaction of diarylethene derivatives depending on particle size, distance from the particle surface, and irradiation wavelength. *Physical Chemistry Chemical Physics* **2012**, *14*, 4898–4905.

[99] El-Sayed, M. A. Plasmonic photochemistry and photon confinement to the nanoscale. *Journal of Photochemistry and Photobiology A: Chemistry* **2011**, *221*, 138–142.

[100] Ringe, E.; Langille, M. R.; Sohn, K.; Zhang, J.; Huang, J.; Mirkin, C. A.; Van Duyne, R. P.; Marks, L. D. Plasmon Length: A Universal Parameter to Describe Size Effects in Gold Nanoparticles. *The Journal of Physical Chemistry Letters* **2012**, *3*, 1479–1483.

[101] Deeb, C.; Zhou, X.; Plain, J.; Wiederrecht, G. P.; Bachelot, R.; Russell, M.; Jain, P. K. Size Dependence of the Plasmonic Near-Field Measured via Single-Nanoparticle Photoimaging. *The Journal of Physical Chemistry C* **2013**, *117*, 10669–10676.

[102] Ward, C. L. Controlling the Cycloreversion Reaction of a Diarylethene Derivative Using Sequential Two-Photon Excitation. **2014**,

[103] March, A. M.; Stickrath, A.; Doumy, G.; Kanter, E. P.; Krässig, B.; Southworth, S. H.; Attenkofer, K.; Kurtz, C. A.; Chen, L. X.; Young, L. Development of high-repetition-rate laser pump/x-ray probe methodologies for synchrotron facilities. *Review of Scientific Instruments* **2011**, *82*, 073110.

[104] Dufresne, E. M.; Adams, B.; Arms, D. A.; Chollet, M.; Landahl, E. C.; Li, Y.; Walko, D. A.; Wang, J. Time-Resolved Research at the Advanced Photon Source Beamline 7-ID. *AIP Conference Proceedings* **2010**, *1234*, 181–184.

[105] Eng, P. J.; Newville, M.; Rivers, M. L.; Sutton, S. R. *Dynamically figured Kirkpatrick Baez x-ray microfocusing optics*; SPIE's International Symposium on Optical Science, Engineering, and Instrumentation; SPIE, 1998; Vol. 3449.

[106] Takei, M.; Yui, H.; Hirose, Y.; Sawada, T. Femtosecond time-resolved spectroscopy of photoisomerization of methyl orange in cyclodextrins. *J. Phys. Chem. A* **2001**, *105*, 11395–11399.

[107] Bahrenburg, J.; Renth, F.; Temps, F.; Plamper, F.; Richtering, W. Femtosecond spectroscopy reveals huge differences in the photoisomerisation dynamics between azobenzenes linked to polymers and azobenzenes in solution. *Phys. Chem. Chem. Phys.* **2014**, *16*, 11549–11554.

[108] Grimmelsmann, L.; Khah, A. M.; Spies, C.; Haettig, C.; Nuernberger, P. Ultrafast dynamics of a triazene: Excited-state pathways and the impact of binding to the minor groove of DNA and further biomolecular systems. *J. Phys. Chem. Lett.* **2017**, *8*, 1986–1992.

[109] Ramamurthy, V.; Parthasarathy, A. Chemistry in restricted spaces: Select photodimerizations in cages, cavities, and capsules. *Isr. J. Chem.* **2011**, *51*, 817–829.

[110] Parthasarathy, A.; Ramamurthy, V. Water-soluble octa acid capsule as a reaction container: Templated photodimerization of indene in water. *J. Photochem. Photobiol., A* **2016**, *317*, 132–139.

[111] Beharry, A. A.; Woolley, G. A. Azobenzene photoswitches for biomolecules. *Chem. Soc. Rev.* **2011**, *40*, 4422–4437.

[112] Dugave, C.; Demange, L. *cis-trans* isomerization of organic molecules and biomolecules: Implications and applications. *Chem. Rev.* **2003**, *103*, 2475–2532.

[113] Banghart, M.; Mourot, A.; Fortin, D.; Yao, J.; Kramer, R.; Trauner, D. Photochromic blockers of voltage-gated potassium channels. *Angew. Chem., Int. Ed.* **2009**, *48*, 9097–9101.

[114] Kim, Y.; Phillips, J. A.; Liu, H.; Kang, H.; Tan, W. Using photons to manipulate enzyme inhibition by an azobenzene-modified nucleic acid probe. *Proc. Natl. Acad. Sci.* **2009**, *106*, 6489–6494.

[115] Wang, J.; Liu, H.-B.; Ha, C.-S. Zinc-supported azobenzene derivative-based colorimetric fluorescent 'turn-on' sensing of bovine serum albumin. *Tetrahedron* **2009**, *65*, 9686–9689.

[116] Banghart, M.; Borges, K.; Isacoff, E.; Trauner, D.; Kramer, R. H. Light-activated ion channels for remote control of neuronal firing. *Nat. Neurosci.* **2004**, *7*, 1381.

[117] Norikane, Y.; Tamaoki, N. Light-driven molecular hinge: A new molecular machine showing a light-intensity-dependent photoresponse that utilizes the *trans-cis* isomerization of azobenzene. *Org. Lett.* **2004**, *6*, 2595–2598.

[118] Murakami, H.; Kawabuchi, A.; Kotoo, K.; Kunitake, M.; Nakashima, N. A light-driven molecular shuttle based on a rotaxane. *J. Am. Chem. Soc.* **1997**, *119*, 7605–7606.

[119] Wen, Y.; Yi, W.; Meng, L.; Feng, M.; Jiang, G.; Yuan, W.; Zhang, Y.; Gao, H.; Jiang, L.; Song, Y. Photochemical-controlled switching based on azobenzene monolayer modified silicon (111) surface. *J. Phys. Chem. B* **2005**, *109*, 14465–14468.

[120] Kakiage, K.; Yamamura, M.; Ido, E.; Kyomen, T.; Unno, M.; Hanaya, M. Reactivity of alkoxysilyl compounds: Chemical surface modification of nano-porous alumina membrane using alkoxysilylazobenzenes. *Appl. Organomet. Chem.* **2011**, *25*, 98–104.

[121] Masahide, I.; Kenji, H.; Shun-ichi, K.; Toyohiko, Y. Holographic recording on azo-benzene functionalized polymer film. *Jpn. J. Appl. Phys.* **2004**, *43*, 4968.

[122] Jiang, X. L.; Li, L.; Kumar, J.; Kim, D. Y.; Tripathy, S. K. Unusual polarization dependent optical erasure of surface relief gratings on azobenzene polymer films. *Appl. Phys. Lett.* **1998**, *72*, 2502–2504.

[123] Waldeck, D. Photoisomerization dynamics of stilbenes. *Chem. Rev.* **1991**, *91*, 415–436.

[124] Bandara, H. M. D.; Burdette, S. C. Photoisomerization in different classes of azobenzene. *Chem. Soc. Rev.* **2012**, *41*, 1809–1825.

[125] Parthasarathy, A.; Kaanumalle, L. S.; Ramamurthy, V. Controlling photochemical geometric isomerization of a stilbene and dimerization of a styrene using a confined reaction cavity in water. *Org. Lett.* **2007**, *9*, 5059–5062.

[126] Samanta, S. R.; Parthasarathy, A.; Ramamurthy, V. Supramolecular control during triplet sensitized geometric isomerization of stilbenes encapsulated in a water soluble organic capsule. *Photochem. Photobiol. Sci.* **2012**, *11*, 1652–1660.

[127] Mohan Raj, A.; Ramamurthy, V. Volume conserving geometric isomerization of encapsulated azobenzenes in ground and excited states and as radical ion. *Org. Lett.* **2017**, *19*, 6116–6119.

[128] Porel, M.; Jockusch, S.; Parthasarathy, A.; Rao, V. J.; Turro, N. J.; Ramamurthy, V. Photoinduced electron transfer between a donor and an acceptor separated by a capsular wall. *Chem. Comm.* **2012**, *48*, 2710–2712.

[129] Gibb, C. L. D.; Gibb, B. C. Well-defined, organic nanoenvironments in water: The hydrophobic effect drives a capsular assembly. *J. Am. Chem. Soc.* **2004**, *126*, 11408–11409.

[130] Houk, A. L.; Zheldakov, I. L.; Tommey, T. A.; Elles, C. G. Two-photon excitation of *trans*-stilbene: Spectroscopy and dynamics of electronically excited states above S_1. *J. Phys. Chem. B* **2015**, *119*, 9335–9344.

[131] Kovalenko, S. A.; Dobryakov, A. L.; Ioffe, I.; Ernsting, N. P. Evidence for the phantom state in photoinduced *cis-trans* isomerization of stilbene. *Chem. Phys. Lett.* **2010**, *493*, 255–258.

[132] Hochstrasser, R. Picosecond processes in the isomerism of stilbenes. *Pure Appl. Chem.* **1980**, *52*, 2683–2691.

[133] Levine, B. G.; Martinez, T. J. Isomerization through conical intersections. *Annu. Rev. Phys. Chem.* **2007**, *58*, 613–634.

[134] Ioffe, I. N.; Quick, M.; Quick, M. T.; Dobryakov, A. L.; Richter, C.; Granovsky, A. A.; Berndt, F.; Mahrwald, R.; Ernsting, N. P.; Kovalenko, S. A. Tuning stilbene photochemistry by fluorination: State reordering leads to sudden polarization near the Franck–Condon region. *J. Am. Chem. Soc.* **2017**, *139*, 15265–15274, PMID: 28985461.

[135] Hammond, G. S.; Saltiel, J.; Lamola, A. A.; Turro, N. J.; Bradshaw, J. S.; Cowan, D. O.; Counsell, R. C.; Vogt, V.; Dalton, C. Mechanisms of photochemical reactions in solution. XXII. Photochemical *cis-trans* isomerization. *J. Am. Chem. Soc.* **1964**, *86*, 3197–3217.

[136] Nenov, A.; Borrego-Varillas, R.; Oriana, A.; Ganzer, L.; Segatta, F.; Conti, I.; Segarra-Marti, J.; Omachi, J.; Dapor, M.; Taioli, S.; Manzoni, C.; Mukamel, S.; Cerullo, G.; Garavelli, M. UV-light-induced vibrational coherences: The key to understand Kasha rule violation in *trans*-azobenzene. *J. Phys. Chem. Lett.* **2018**, *9*, 1534–1541.

[137] Wei-Guang Diau, E. A new *trans*-to-*cis* photoisomerization mechanism of azobenzene on the $S_1(n,\pi^*)$ surface. *J. Phys. Chem. A* **2004**, *108*, 950–956.

[138] Lednev, I. K.; Ye, T.-Q.; Hester, R. E.; Moore, J. N. Femtosecond time-resolved UV-visible absorption spectroscopy of *trans*-azobenzene in solution. *J. Phys. Chem.* **1996**, *100*, 13338–13341.

[139] Fujino, T.; Arzhantsev, S. Y.; Tahara, T. Femtosecond time-resolved fluorescence study of photoisomerization of *trans*-azobenzene. *J. Phys. Chem. A* **2001**, *105*, 8123–8129.

[140] Stuart, C. M.; Frontiera, R. R.; Mathies, R. A. Excited-state structure and dynamics of *cis*- and *trans*-azobenzene from resonance Raman intensity analysis. *J. Phys. Chem. A* **2007**, *111*, 12072–12080.

[141] Fujino, T.; Tahara, T. Picosecond time-resolved Raman study of *trans*-azobenzene. *J. Phys. Chem. A* **2000**, *104*, 4203–4210.

[142] Satzger, H.; Root, C.; Braun, M. Excited-state dynamics of *trans*- and *cis*-azobenzene after UV excitation in the $\pi\pi^*$ band. *J. Phys. Chem. A* **2004**, *108*, 6265–6271.

[143] Quick, M.; Dobryakov, A. L.; Gerecke, M.; Richter, C.; Berndt, F.; Ioffe, I. N.; Granovsky, A. A.; Mahrwald, R.; Ernsting, N. P.; Kovalenko, S. A. Photoisomerization dynamics and pathways of *trans*- and *cis*-azobenzene in solution from broadband femtosecond spectroscopies and calculations. *J. Phys. Chem. B* **2014**, *118*, 8756–8771.

[144] Lednev, I. K.; Ye, T. Q.; Matousek, P.; Towrie, M.; Foggi, P.; Neuwahl, F. V. R.; Umapathy, S.; Hester, R. E.; Moore, J. N. Femtosecond time-resolved UV-visible absorption spectroscopy of trans-azobenzene: dependence on excitation wavelength. *Chem. Phys. Lett.* **1998**, *290*, 68–74.

[145] Tatsuya, F.; Yu., A. S.; Tahei, T. Femtosecond/picosecond time-resolved spectroscopy of *trans*-azobenzene: Isomerization mechanism following $S_2(\pi\pi*)\leftarrow S_0$ photoexcitation. *Bull. Chem. Soc. Jpn.* **2002**, *75*, 1031–1040.

[146] Kovalenko, S. A.; Schanz, R.; Hennig, H.; Ernsting, N. P. Cooling dynamics of an optically excited molecular probe in solution from femtosecond broadband transient absorption spectroscopy. *J. Chem. Phys.* **2001**, *115*, 3256–3273.

[147] Lednev, I. K.; Ye, T.-Q.; Abbott, L. C.; Hester, R. E.; Moore, J. N. Photoisomerization of a capped azobenzene in solution probed by ultrafast time-resolved electronic absorption spectroscopy. *J. Phys. Chem. A* **1998**, *102*, 9161–9166.

[148] Rosspeintner, A.; Lang, B.; Vauthey, E. Ultrafast Photochemistry in Liquids. *Annu. Rev. Phys. Chem.* **2013**, *64*, 247–271.

[149] Orr-Ewing, A. J. Taking the plunge: Chemical reaction dynamics in liquids. *Chem. Soc. Rev.* **2017**, *46*, 7597–7614.

[150] Varghese, J. J.; Mushrif, S. H. Origins of complex solvent effects on chemical reactivity and computational tools to investigate them: a review. *React. Chem. Eng.* **2019**, *4*, 165–206.

[151] Kukura, P.; McCamant, D.; Yoon, S.; Wandschneider, D.; Mathies, R. Structural observation of the primary isomerization in vision with femtosecond-stimulated Raman. *Science* **2005**, *310*, 1006–1009.

[152] Kirpich, J. S.; Mix, L. T.; Martin, S. S.; Rockwell, N. C.; Lagarias, J. C.; Larsen, D. S. Protonation Heterogeneity Modulates the Ultrafast Photocycle Initiation Dynamics of Phytochrome Cph1. *J. Phys. Chem. Lett.* **2018**, *9*, 3454–3462.

[153] Dugave, C.; Demange, L. *cis-trans* isomerization of organic molecules and biomolecules: Implications and applications. *Chem. Rev.* **2003**, *103*, 2475–2532.

[154] Van der Horst, M.; Hellingwerf, K. Photoreceptor proteins, "star actors of modern times": A review of the functional dynamics in the structure of representative members of six different photoreceptor families. *Acc. Chem. Rev.* **2004**, *37*, 13–20.

[155] Waldeck, D. Photoisomerization Dynamics Of Stilbenes In Polar-Solvents. *J. Mol. Liq.* **1993**, *57*, 127–148.

[156] Saltiel, J.; Gupta, S. Photochemistry of the Stilbenes in Methanol. Trapping the Common Phantom Singlet State. *J. Phys. Chem. A* **2018**, *122*, 6089–6099.

[157] Kovalenko, S. A.; Dobryakov, A. L.; Ioffe, I.; Ernsting, N. P. Evidence for the phantom state in photoinduced *cis-trans* isomerization of stilbene. *Chem. Phys. Lett.* **2010**, *493*, 255–258.

[158] Ioffe, I. N.; Granovsky, A. A. Photoisomerization of Stilbene: The Detailed XMCQDPT2 Treatment. *J. Chem. Theo. Comp.* **2013**, *9*, 4973–4990.

[159] Fuss, W. Predistortion amplified in the excited state. *J. Photochem. Photobiol. A* **2015**, *297*, 45–57.

[160] Kulasekharan, R.; Ramamurthy, V. New Water-Soluble Organic Capsules Are Effective in Controlling Excited-State Processes of Guest Molecules. *Org. Lett.* **2011**, *13*, 5092–5095.

[161] Gibb, C. L. D.; Gibb, B. C. Well-Defined, Organic Nanoenvironments in Water: The Hydrophobic Effect Drives a Capsular Assembly. *J. Am. Chem. Soc.* **2004**, *126*, 11408–11409.

[162] Mohan Raj, A.; Ramamurthy, V. Volume conserving geometric isomerization of encapsulated azobenzenes in ground and excited states and as radical ion. *Org. Lett.* **2017**, *19*, 6116–6119.

[163] Choudhury, R.; Barman, A.; Prabhakar, R.; Ramamurthy, V. Hydrocarbons depending on the chain length and head group adopt different conformations within a water-soluble nanocapsule: ^{1}H NMR and molecular dynamics studies. *J. Phys. Chem. B* **2012**, *117*, 398–407.

[164] Becke, A. Density-Functional Thermochemistry. 3. The Role Of Exact Exchange. *J. Phys. Chem.* **1993**, *98*, 5648–5652.

[165] Francl, M.; Pietro, W.; Hehre, W.; Binkley, J.; Gordon, M.; Defrees, D.; Pople, J. Self-Consistent Molecular-Orbital Methods. 23. A Polarization-Type Basis Set for 2nd-Row Elements. *J. Phys. Chem.* **1982**, *77*, 3654–3665.

[166] Frisch, M. J. et al. Gaussian 09. 2009; Gaussian Inc., Wallingford, CT.

[167] Wang, J.; Wang, W.; Kollman, P. A.; Case, D. A. Antechamber: an accessory software package for molecular mechanical calculations. *J. Am. Chem. Soc.* **2001**, *222*, U403.

[168] Trott, O.; Olson, A. J. AutoDock Vina: improving the speed and accuracy of docking with a new scoring function, efficient optimization, and multithreading. *J. Comp. Chem.* **2010**, *31*, 455–461.

[169] Hess, B.; Kutzner, C.; Van Der Spoel, D.; Lindahl, E. GROMACS 4: algorithms for highly efficient, load-balanced, and scalable molecular simulation. *J. Chem. Theo. Comp.* **2008**, *4*, 435–447.

[170] Case, D. A.; Cheatham, T. E.; Darden, T.; Gohlke, H.; Luo, R.; Merz, K. M.; Onufriev, A.; Simmerling, C.; Wang, B.; Woods, R. J. The Amber biomolecular simulation programs. *J. Comp. Chem.* **2005**, *26*, 1668–1688.

[171] Miyamoto, S.; Kollman, P. A. Settle: An analytical version of the SHAKE and RATTLE algorithm for rigid water models. *J. Comp. Chem.* **1992**, *13*, 952–962.

[172] Hess, B.; Bekker, H.; Berendsen, H. J.; Fraaije, J. G. LINCS: a linear constraint solver for molecular simulations. *J. Comp. Chem.* **1997**, *18*, 1463–1472.

[173] Darden, T.; York, D.; Pedersen, L. Particle Mesh Ewald - An N.Log(N) Method for Ewald Sums in Large Systems. *J. Phys. Chem.* **1993**, *98*, 10089–10092.

[174] Price, D. J.; Brooks III, C. L. A modified TIP3P water potential for simulation with Ewald summation. *J. Phys. Chem.* **2004**, *121*, 10096–10103.

[175] Krieger, E.; Vriend, G. YASARA View—molecular graphics for all devices—from smartphones to workstations. *Bioinformatics* **2014**, *30*, 2981–2982.

[176] Pettersen, E. F.; Goddard, T. D.; Huang, C. C.; Couch, G. S.; Greenblatt, D. M.; Meng, E. C.; Ferrin, T. E. UCSF Chimera—a visualization system for exploratory research and analysis. *J. Comp. Chem.* **2004**, *25*, 1605–1612.

[177] Humphrey, W.; Dalke, A.; Schulten, K. VMD: visual molecular dynamics. *J. Mol. Graph.* **1996**, *14*, 33–38.

[178] Kumari, R.; Kumar, R.; Lynn, A. G-MMPBSA- A GROMACS Tool for High-Throughput MM-PBSA Calculations. *J. Chem. Info. Model.* **2014**, *54*, 1951–1962.

[179] Warshel, A. Calculation of Vibronic Structure of the π-π Transition of trans-Stilbene and cis-Stilbene. *J. Phys. Chem.* **1975**, *62*, 214–221.

[180] Choi, C.; Kertesz, M. Conformational information from vibrational spectra of styrene, trans-stilbene, and cis-stilbene. *J. Phys. Chem. A* **1997**, *101*, 3823–3831.

[181] Molina, V.; Merchan, M.; Roos, B. Theoretical study of the electronic spectrum of trans-stilbene. *J. Phys. Chem. A* **1997**, *101*, 3478–3487.

[182] Massuyeau, F.; Faulques, E.; Latouche, C.; Barone, V. New insights into the vibrational and optical signatures of trans-stilbene via integrated experimental and quantum mechanical approaches. *Phys. Chem. Chem. Phys.* **2016**, *18*, 19378–19385.

[183] Porel, M.; Jayaraj, N.; Kaanumalle, L. S.; Maddipatla, M. V. S. N.; Parthasarathy, A.; Ramamurthy, V. Cavitand Octa Acid Forms a Nonpolar Capsuleplex Dependent on the Molecular Size and Hydrophobicity of the Guest. *Langmuir* **2009**, *25*, 3473–3481.

[184] Houk, A. L.; Zheldakov, I. L.; Tommey, T. A.; Elles, C. G. Two-Photon Excitation of trans-Stilbene: Spectroscopy and Dynamics of Electronically Excited States above S1. *J. Phys. Chem. B* **2015**, *119*, 9335–9344.

[185] Briney, K. A.; Herman, L.; Boucher, D. S.; Dunkelberger, A. D.; Crim, F. F. The Influence of Vibrational Excitation on the Photoisomerization of trans-Stilbene in Solution. *J. Phys. Chem. A* **2010**, *114*, 9788–9794.

[186] Kovalenko, S. A.; Dobryakov, A. L. On the excitation wavelength dependence and Arrhenius behavior of stilbene isomerization rates in solution. *Chem. Phys. Lett.* **2013**, *570*, 56–60.

[187] Kovalenko, S. A.; Schanz, R.; Hennig, H.; Ernsting, N. P. Cooling dynamics of an optically excited molecular probe in solution from femtosecond broadband transient absorption spectroscopy. *J. Phys. Chem.* **2001**, *115*, 3256–3273.

[188] Zheldakov, I. L.; Wasylenko, J. M.; Elles, C. G. Excited-state dynamics and efficient triplet formation in phenylthiophene compounds. *Phys. Chem. Chem. Phys.* **2012**, *14*, 6211–6218.

[189] Ben-Nun, M.; Quenneville, J.; Martinez, T. Ab initio multiple spawning: Photochemistry from first principles quantum molecular dynamics. *J. Phys. Chem. A* **2000**, *104*, 5161–5175.

[190] Orlandi, G.; Garavelli, M.; Zerbetto, F. Analysis of the vibronic structure of the trans-stilbene fluorescence and excitation spectra: the S-0 and S-1 PES along the C-e=C-e and C-e-C-ph torsions. *Phys. Chem. Chem. Phys.* **2017**, *19*, 25095–25104.

[191] Aldaz, C.; Kammeraad, J. A.; Zimmerman, P. M. Discovery of conical intersection mediated photochemistry with growing string methods. *Phys. Chem. Chem. Phys.* **2018**, *20*, 27394–27405.

[192] Fuss, W.; Lochbrunner, S.; Muller, A.; Schikarski, T.; Schmid, W.; Trushin, S. Pathway approach to ultrafast photochemistry: potential surfaces, conical intersections and isomerizations of small polyenes. *Chem. Phys.* **1998**, *232*, 161–174.

[193] Jayaraj, N.; Jockusch, S.; Kaanumalle, L. S.; Turro, N. J.; Ramamurthy, V. Dynamics of capsuleplex formed between octaacid and organic guest molecules - Photophysical techniques reveal the opening and closing of capsuleplex. *Can. J. Chem.* **2011**, *89*, 203–213.

[194] Wen, Y.; Yi, W.; Meng, L.; Feng, M.; Jiang, G.; Yuan, W.; Zhang, Y.; Gao, H.; Jiang, L.; Song, Y. Photochemical-Controlled Switching Based on Azobenzene Monolayer Modified Silicon (111) Surface. *The Journal of Physical Chemistry B* **2005**, *109*, 14465–14468.

[195] Kakiage, K.; Yamamura, M.; Ido, E.; Kyomen, T.; Unno, M.; Hanaya, M. Reactivity of alkoxysilyl compounds: chemical surface modification of nano-porous alumina membrane using alkoxysilylazobenzenes. *Applied Organometallic Chemistry* **2011**, *25*, 98–104.

[196] Masahide, I.; Kenji, H.; Shun-ichi, K.; Toyohiko, Y. Holographic Recording on Azobenzene Functionalized Polymer Film. *Japanese Journal of Applied Physics* **2004**, *43*, 4968.

[197] Jiang, X. L.; Li, L.; Kumar, J.; Kim, D. Y.; Tripathy, S. K. Unusual polarization dependent optical erasure of surface relief gratings on azobenzene polymer films. *Applied Physics Letters* **1998**, *72*, 2502–2504.

[198] Norikane, Y.; Tamaoki, N. Light-Driven Molecular Hinge: A New Molecular Machine Showing a Light-Intensity-Dependent Photoresponse that Utilizes the *trans-cis* Isomerization of Azobenzene. *Organic Letters* **2004**, *6*, 2595–2598.

[199] Murakami, H.; Kawabuchi, A.; Kotoo, K.; Kunitake, M.; Nakashima, N. A Light-Driven Molecular Shuttle Based on a Rotaxane. *Journal of the American Chemical Society* **1997**, *119*, 7605–7606.

[200] Beharry, A. A.; Woolley, G. A. Azobenzene photoswitches for biomolecules. *Chemical Society Reviews* **2011**, *40*, 4422–4437.

[201] Banghart, M.; Mourot, A.; Fortin, D.; Yao, J.; Kramer, R.; Trauner, D. Photochromic Blockers of Voltage-Gated Potassium Channels. *Angewandte Chemie International Edition* **2009**, *48*, 9097–9101.

[202] Kim, Y.; Phillips, J. A.; Liu, H.; Kang, H.; Tan, W. Using photons to manipulate enzyme inhibition by an azobenzene-modified nucleic acid probe. *Proceedings of the National Academy of Sciences* **2009**, *106*, 6489–6494.

[203] Wang, J.; Liu, H.-B.; Ha, C.-S. Zinc-supported azobenzene derivative-based colorimetric fluorescent 'turn-on' sensing of bovine serum albumin. *Tetrahedron* **2009**, *65*, 9686–9689.

[204] Banghart, M.; Borges, K.; Isacoff, E.; Trauner, D.; Kramer, R. H. Light-activated ion channels for remote control of neuronal firing. *Nature Neuroscience* **2004**, *7*, 1381.

[205] Ramamurthy, V.; Parthasarathy, A. Chemistry in Restricted Spaces: Select Photodimerizations in Cages, Cavities, and Capsules. *Israel Journal of Chemistry* **2011**, *51*, 817–829.

[206] Landt, L.; Staiger, M.; Wolter, D.; Klünder, K.; Zimmermann, P.; Willey, T. M.; Buuren, T. v.; Brehmer, D.; Schreiner, P. R.; Tkachenko, B. A.; Fokin, A. A.; Möller, T.; Bostedt, C. The influence of a single thiol group on the electronic and optical properties of the smallest diamondoid adamantane. *The Journal of Chemical Physics* **2010**, *132*, 024710.

[207] Hirose, Y.; Yui, H.; Sawada, T. Effect of Potential Energy Gap between the n-π^* and the π-π^* State on Ultrafast Photoisomerization Dynamics of an Azobenzene Derivative. *The Journal of Physical Chemistry A* **2002**, *106*, 3067–3071.

[208] Mohan Raj, A.; Ramamurthy, V. Volume Conserving Geometric Isomerization of Encapsulated Azobenzenes in Ground and Excited States and as Radical Ion. *Organic Letters* **2017**, *19*, 6116–6119.

[209] Quick, M.; Dobryakov, A. L.; Gerecke, M.; Richter, C.; Berndt, F.; Ioffe, I. N.; Granovsky, A. A.; Mahrwald, R.; Ernsting, N. P.; Kovalenko, S. A. Photoisomerization Dynamics and Pathways of trans- and cis-Azobenzene in Solution from Broadband Femtosecond Spectroscopies and Calculations. *The Journal of Physical Chemistry B* **2014**, *118*, 8756–8771.

[210] Moreno, M.; Gelabert, R.; Lluch, J. M. The Quest for Photoswitches Activated by Near-Infrared Light: A Theoretical Study of the Photochemistry of BF2-Coordinated Azo Derivatives. *ChemPhysChem* **2016**, *17*, 2824–2838.

[211] Weak absorption for $n\pi^*$ excitation requires higher concentrations, which limits the volume of the Az@OA_2 sample. The much stronger absorption for $\pi\pi^*$ excitation allows a lower concentration sample and therefore larger sample volume.

[212] Lednev, I.; Ye, T.-Q.; Matousek, P.; Towrie, M.; Foggi, P.; Neuwahl, F.; Umapathy, S.; Hester, R.; Moore, J. Femtosecond time-resolved UV-visible absorption spectroscopy of trans-azobenzene: dependence on excitation wavelength. *Chemical Physics Letters* **1998**, *290*, 68 – 74.

[213] The relative quantum yields are more accurate than the absolute errors that we report, because all of the samples were measured back-to-back under identical conditions.

[214] Hendler, R. W.; Shrager, R. I. Deconvolutions based on singular value decomposition and the pseudoinverse: a guide for beginners. *Journal of Biochemical and Biophysical Methods* **1994**, *28*, 1–33.

[215] van Stokkum, I. H. M.; Larsen, D. S.; van Grondelle, R. Global and target analysis of time-resolved spectra. *Biochimica et Biophysica Acta (BBA) - Bioenergetics* **2004**, *1657*, 82–104.

[216] Nenov, A.; Borrego-Varillas, R.; Oriana, A.; Ganzer, L.; Segatta, F.; Conti, I.; Segarra-Marti, J.; Omachi, J.; Dapor, M.; Taioli, S.; Manzoni, C.; Mukamel, S.; Cerullo, G.; Garavelli, M. UV-Light-Induced Vibrational Coherences: The Key to Understand Kasha Rule Violation in trans-Azobenzene. *The Journal of Physical Chemistry Letters* **2018**, 1534–1541.

[217] Nagele, T.; Hoche, R.; Zinth, W.; Wachtveitl, J. Femtosecond photoisomerization of cis-azobenzene. *Chemical Physics Letters* **1997**, *272*, 489 – 495.

[218] Azuma, J.; Tamai, N.; Shishido, A.; Ikeda, T. Femtosecond dynamics and stimulated emission from the S2 state of a liquid crystalline trans-azobenzene. *Chemical Physics Letters* **1998**, *288*, 77–82.

[219] Lewis, N. S.; Nocera, D. G. Powering the planet: Chemical challenges in solar energy utilization. *Proceedings of the National Academy of Sciences* **2006**, *103*, 15729.

[220] Lewis, N. S. Research opportunities to advance solar energy utilization. *Science* **2016**, *351*, aad1920.

[221] Morris, A.; Meyer, G.; Fujita, E. Molecular approaches to the photocatalytic reduction of carbon dioxide for solar fuels. *Accounts of Chemical Research* **2009**, *42*, 1983–1994.

[222] Benson, E. E.; Kubiak, C. P.; Sathrum, A. J.; Smieja, J. M. Electrocatalytic and homogeneous approaches to conversion of CO2 to liquid fuels. *Chemical Society Reviews* **2009**, *38*, 89–99.

[223] Appel, A. M. et al. Frontiers, opportunities, and challenges in biochemical and chemical catalysis of CO2 fixation. *Chemical reviews* **2013**, *113*, 6621–6658.

[224] Bourrez, M.; Molton, F.; Chardon-Noblat, S.; Deronzier, A. [Mn(bipyridyl)(CO)3Br]: An Abundant Metal Carbonyl Complex as Efficient Electrocatalyst for CO2 Reduction. *Angewandte Chemie International Edition* **2011**, *50*, 9903–9906.

[225] Smieja, J. M.; Sampson, M. D.; Grice, K. A.; Benson, E. E.; Froehlich, J. D.; Kubiak, C. P. Manganese as a Substitute for Rhenium in CO2 Reduction Catalysts: The Importance of Acids. *Inorganic Chemistry* **2013**, *52*, 2484–2491.

[226] Henke, W. C.; Otolski, C. J.; Moore, W. N. G.; Elles, C. G.; Blakemore, J. D. Modulation of Photochemical CO Release Kinetics from [$Mn(CO)_3$] Complexes Bearing Disubstituted 2,2-Bipyridyl Ligands. in preparation.

[227] Ramallo-Lopez, J. M.; Lede, E. J.; Requejo, F. G.; Rodriguez, J. A.; Kim, J. Y.; Rosas-Salas, R.; Dominguez, J. M. XANES Characterization of Extremely Nanosized Metal-Carbonyl Subspecies (Me = Cr, Mn, Fe, and Co) Confined into the Mesopores of MCM-41 Materials. *The Journal of Physical Chemistry B* **2004**, *108*, 20005–20010.

[228] Cho, H.; Hong, K.; Strader, M. L.; Lee, J. H.; Schoenlein, R. W.; Huse, N.; Kim, T. K. Electronic and Molecular Structure of the Transient Radical Photocatalyst Mn(CO)5 and Its Parent Compound Mn2(CO)10. *Inorganic Chemistry* **2016**, *55*, 5895–5903.

[229] Tanaka, K.; Yu, Q.; Sasaki, K.; Ohnuki, T. *Cobalt(II) Oxidation by Biogenic Mn Oxide Produced by Pseudomonas sp. Strain NGY-1*; 2013; Vol. 30.

[230] Rosa, A.; Ricciardi, G.; Baerends, E. J.; Stufkens, D. J. Metal-to-Ligand Charge Transfer (MLCT) Photochemistry of fac-Mn(Cl)(CO)3(H-DAB): A Density Functional Study. *The Journal of Physical Chemistry* **1996**, *100*, 15346–15357.

[231] Baerends, E. J.; Rosa, A. Metal-CO photodissociation in transition metal complexes: The role of ligand-field and charge-transfer excited states in the photochemical dissociation of metal-ligand bonds. *Coordination Chemistry Reviews* **1998**, *177*, 97–125.

[232] Rosa, A.; Ricciardi, G.; Baerends, E. J.; Stufkens, D. J. Metal-to-Ligand Charge Transfer Photochemistry: Homolysis of the Mn-Cl Bond in the mer-Mn(Cl)(CO)3(α-diimine) Complex and Its Absence in the fac-Isomer. *Inorganic Chemistry* **1998**, *37*, 6244–6254.

[233] Hohenester, U.; Trügler, A. MNPBEM – A Matlab toolbox for the simulation of plasmonic nanoparticles. *Computer Physics Communications* **2012**, *183*, 370–381.

[234] Guidez, E. B.; Aikens, C. M. Plasmon resonance analysis with configuration interaction. *Phys. Chem. Chem. Phys.* **2014**, *16*, 15501–15509.

[235] Irie, M. Diarylethenes for memories and seitches. *Chem. Rev.* **2000**, *100*, 1685–1716.

[236] Shibata, K.; Muto, K.; Kobatake, S.; Irie, M. Photocyclization/Cycloreversion Quantum Yields of Diarylethenes in Single Crystals. *The Journal of Physical Chemistry A* **2002**, *106*, 209–214.

[237] Kobatake, S.; Yamada, T.; Uchida, K.; Kato, N.; Irie, M. Photochromism of 1,2-Bis(2,5-dimethyl-3-thienyl)perfluoro- cyclopentene in a Single Crystalline Phase. *Journal of the American Chemical Society* **1999**, *121*, 2380–2386.

[238] Becker, M.; Huang, W. C.-W.; Batelaan, H.; Smythe, E. J.; Capasso, F. Measurement of the ultrafast temporal response of a plasmonic antenna. *Annalen der Physik* **2013**, *525*, L6–L11.

[239] Pariani, G.; Bianco, A.; Castagna, R.; Bertarelli, C. Kinetics of Photochromic Conversion

at the Solid State: Quantum Yield of Dithienylethene-Based Films. *The Journal of Physical Chemistry A* **2011**, *115*, 12184–12193.

[240] John, S.; Soukoulis, C.; Cohen, M. H.; Economou, E. N. Theory of Electron Band Tails and the Urbach Optical-Absorption Edge. *Physical Review Letters* **1986**, *57*, 1777–1780.

[241] Sumi, T.; Takagi, Y.; Yagi, A.; Morimoto, M.; Irie, M. Photoirradiation wavelength dependence of cycloreversion quantum yields of diarylethenes. *Chemical Communications* **2014**, *50*, 3928–3930.

[242] Buchanan, L. E.; Gruenke, N. L.; McAnally, M. O.; Negru, B.; Mayhew, H. E.; Apkarian, V. A.; Schatz, G. C.; Van Duyne, R. P. Surface-Enhanced Femtosecond Stimulated Raman Spectroscopy at 1 MHz Repetition Rates. *The Journal of Physical Chemistry Letters* **2016**, *7*, 4629–4634.

[243] Nakabayashi, T.; Kamo, S.; Sakuragi, H.; Nishi, N. Time-Resolved Raman Studies of Photoionization of Aromatic Compounds in Polar Solvents: Picosecond Relaxation Dynamics of Aromatic Cation Radicals. *The Journal of Physical Chemistry A* **2001**, *105*, 8605–8614.

[244] Lin, Y.; Jonah, C. D. Picosecond dynamics of benzophenone anion solvation. *The Journal of Physical Chemistry* **1993**, *97*, 295–302.

[245] Schmit, J. D.; Kamber, E.; Kondev, J. Lattice Model of Diffusion-Limited Bimolecular Chemical Reactions in Confined Environments. *Physical Review Letters* **2009**, *102*, 218302.

[246] Minton, A. P. How can biochemical reactions within cells differ from those in test tubes? *Journal of Cell Science* **2006**, *119*, 2863–2869.